

Seismic structure off- and onshore Maule, constraints for megathrust  
earthquakes in central Chile

Dissertation zur Erlangung des Doktorgrades der  
Mathematisch-Naturwissenschaftlichen Fakultät der  
Christian-Albrechts-Universität zu Kiel

vorgelegt von  
Eduardo Moscoso

Kiel, November 2011

Gedruckt mit Unterstützung des Deutschen Akademischen Austauschdienstes





Referent:	Prof. Dr. E. R. Flueh
Korreferent:	P.D. Ingo Grevemeyer
Tag der mündlichen Prüfung:	28.10.11
Zum Druck genehmigt:	07.11.11

Der Dekan

---

# Acknowledgements

I would like to thank to IFM-GEOMAR and the SFB574 project for the opportunity to work with the data retrieved during the cruise JC23. And my most sincere thanks to the Chilean Comisión Nacional de Investigación Científica y Tecnológica (CONICYT) and the German Academic Exchange Service (DAAD) for their financial support during my doctoral studies in Germany.

---

# Zusammenfassung

Während der letzten Dekaden wurde der chilenische Kontinentalrand seewärts von Maule ( $34^{\circ}S - 36^{\circ}S$ ) als stark gekoppelt und seismische Ruhezone beschrieben. Die angesammelte Spannung entlud sich am 27. Februar 2010 als ein Megabebeben ( $M_w = 8.8$ ) mit einer Bruchzone von  $\sim 400$  km entlang der Plattengrenze zwischen der Nazca und der südamerikanischen Platte. Bisher war wenig bekannt über die seismische Struktur vor Maule. Im Rahmen der zweiten Phase des SFB 574 "Volatile und Fluide in Subduktionszonen" der Christian-Albrechts Universität zu Kiel wurden seismische Daten analysiert um detaillierte Abbildungen der tiefen Strukturen des Kontinentalrandes und des outer Rises zu erstellen.

In dieser Arbeit werden Strukturen des Fore-arc und der Bruchzone der Subduktionszonen vorgestellt, welche aus seismischen Refraktions- und Weitwinkeldaten gewonnen wurden. Die Ergebnisse zeigen einen  $\sim 40$  km langen keilförmigen Körper mit typischen Sedimentgeschwindigkeiten, der als vorderer Akkretionskeil (VAK) interpretiert wird. Landwärts des VAK zeigt das Geschwindigkeitsmodell einen starken Geschwindigkeitskontrast, der einen lithologischen Wechsel andeutet, welcher als Schichtgrenze zwischen VAK und dem Paläo-Akkretionskeil (Backstop) interpretiert wird. Die Lage des Backstops fällt mit der seewärtigen Grenze der Nachbeben zusammen, welche die aufwärts geneigte Grenze der co-seismischen Bruchkante und der seismogenen Zone definiert. Desweiteren fallen die seewärtige Grenze der Nachbeben mit der Lage des Schelf Absatzes der gesamten Bruchzone ( $33.5^{\circ}S - 38.5^{\circ}S$ ) zusammen, die als die Lage des Backstops entlang der Kontinentalgrenze interpretiert wird. Veröffentlichte seismische Profile an der Nord- und Südgrenze der Bruchzone zeigen ebenfalls einen starken horizontalen Geschwindigkeitsgradienten, welcher den seismischen Backstop in einer Entfernung von  $\sim 30$  km von der Deformationsfront zeigt. Die seismischen Weitwinkelreflexionen des oberen Bereiches der subduzierten ozeanischen Kruste belegen die Lage der Plattengrenze vor der Küste, die einen Abtauchwinkel von  $\sim 10^{\circ}$  aufweist. Die Projektion des Epizentrums des Maule Erdbebens auf die modellierte Plattengrenze ergibt ein Hypozentrum in ca. 20 km Tiefe. Dieses deutet darauf hin, dass dieses Erdbeben den Ursprung im mittleren Bereich der seismogenen Zone hatte und weder an der Ober- noch an der Unterkante lag.

Der zweite Teil der Studie ist auf die Abhängigkeit zwischen Bend Faulting der ozeanischen Platte, der Hydratisierung der Lithosphäre und der seismischen Aktivität des flachen outer Rise fokussiert. Um die Interpretation zu unterstützen, werden seismische  $V_p$  und  $V_s$  Modelle aus seismischen Weitwinkeldaten und die Verteilung der 2D Poissonzahl des outer Rise bestimmt. Die ozeanische Lithosphäre zeigt einen hohen Grad an Hydratisierung aufgrund von Eindringen von Wasser durch die durch Biegen entstandenen Bruchzonen, welche dem Meerwasser ausgesetzt sind. Dieser Prozess wird vermutlich durch die Existenz eines Unterseeberges in diesem Gebiet verstärkt. Als Schlussfolgerung

---

ergibt sich ein Eindringen von Wasser bis tief in die Lithosphäre, welches flache Erdbeben im outer Rise auslöst und vermutlich eine Serpentinisierung von ca. 10% im Mantel verursacht.

# Abstract

During the last decades, the Chilean margin offshore Maule ( $34^{\circ}S - 36^{\circ}S$ ) had been reported as a highly locked and seismically quiet zone. The stress-accumulated state finished on the 27th of February 2010, when a megathrust earthquake (with  $M_w = 8.8$ ) ruptured  $\sim 400$  km of the Nazca-South America plate boundary. Unfortunately, up to now little was known about the seismic structure offshore Maule. In the frame of the third phase of the project SFB 574 “Volatiles and Fluids in Subduction Zones” of the Christian-Albrechts University of Kiel, seismic data was analyzed in order to obtain detailed images of the deep structure of the margin and of the outer rise.

Here are presented constraints on the forearc and the subduction zone structure of the rupture area derived from seismic refraction and wide-angle data. The results show a wedge shaped body  $\sim 40$  km wide with typical sedimentary velocities interpreted as a frontal accretionary prism (FAP). Landward of the imaged FAP, the velocity model shows an abrupt velocity-contrast suggesting a lithological change, which is interpreted as the contact between the FAP and the paleo accretionary prism (backstop). The backstop location is coincident with the seaward limit of the aftershocks, defining the updip limit of the co-seismic rupture and the seismogenic zone. Furthermore, the seaward limit of the aftershocks coincides with the location of the shelf break in the entire earthquake rupture area ( $33.5^{\circ}S - 38.5^{\circ}S$ ), which is interpreted as the location of the backstop along the margin. Published seismic profiles at the northern and southern limit of the rupture area also show the presence of a strong horizontal velocity gradient imaging the seismic backstop at a distance of  $\sim 30$  km from the deformation front. The seismic wide-angle reflections from the top of the subducting oceanic crust constrain the location of the plate boundary offshore, dipping  $\sim 10^{\circ}$ . The projection of the epicenter of the Maule earthquake onto our derived interplate boundary yielded a hypocenter around 20 km depth. This implies that the earthquake nucleated somewhere within the seismogenic zone, neither at its updip nor at its downdip limit.

The second part of this thesis focuses on the dependency between the incoming plate's bend faulting, lithospheric hydration and shallow outer rise seismic activity. To support the interpretation, are presented  $V_p$  and  $V_s$  seismic models obtained from wide angle seismic data and the derived 2D Poisson's ratio distribution at the outer rise. The oceanic lithosphere shows a high degree of hydration, due to the water infiltration through the bending-related faults exposed to seawater. This process is presumably intensified by the existence of a seamount in the area. It is concluded that the water infiltrates deep into the lithosphere, triggering shallow earthquakes in the outer rise and likely serpentinization in the mantle, estimated to be about 10%.

---



# Resumen

Durante las últimas décadas, el margen Chileno frente a la región del Maule ( $34^{\circ}S - 36^{\circ}S$ ) había sido reportado como altamente acoplado y poco activo sísmicamente. El estado de acumulación de esfuerzos terminó el 27 de Febrero del 2010, cuando un Megaterremoto de subducción de magnitud  $M_w=8.8$  rompió a lo largo de aproximadamente 400 Km del contacto entre las placas de Nazca y Sudamericana. Hasta ahora, desafortunadamente, poco se sabía de la estructura sísmica frente al Maule. En el marco de la segunda etapa del proyecto SFB 574 “Volátiles y fluidos en zonas de subducción” de la Universidad Christian-Albrechts de Kiel, fueron analizados datos sísmicos con el objeto de obtener una imagen detallada de la estructura del margen y del outer rise.

En el presente trabajo se expone la estructura sísmica del ante arco y de la zona de subducción derivada de datos sísmicos de alto ángulo. Los resultados muestran un cuerpo con forma de cuña de aproximadamente 40 km de ancho que presenta velocidades típicas de sedimentos, interpretado como el Prisma Accecionario Frontal (PAF). Del PAF hacia el continente, el modelo muestra un abrupto incremento en la velocidad lateral, sugiriendo un cambio litológico, que es interpretado como el contacto entre el PAF y el paleo prisma (backstop). La ubicación del Backstop coincide con el límite mar adentro de las réplicas, definiendo el updip de la ruptura co-sísmica y de la zona sismogénica. Mas aún, el límite mar adentro de las réplicas coincide con la ubicación del shelf break a lo largo del área de ruptura, lo que es interpretado como la ubicación del backstop a lo largo del margen. Perfiles sísmicos publicados inmediatamente sobre los límites norte y sur de la zona de ruptura, también muestran la aparición de un fuerte gradiente horizontal de velocidades, reflejando la existencia del backstop de un ancho aproximado de 30 km. Las reflexiones de alto ángulo, restringen la ubicación del plano de subducción, a un ángulo alrededor de  $10^{\circ}$ . La proyección del epicentro del terremoto del Maule sobre el contacto propuesto entre las placas, indica un hipocentro cercano a los 20 km de profundidad. Esto implica que este terremoto no se nucleó en el updip o en el downdip, sino en algún lugar dentro de la zona sismogénica.

La segunda parte de la tesis aborda la dependencia entre el fallamiento normal debido a la flexura de la placa subductante, la hidratación de la litosfera y la actividad sísmica somera en el outer rise. La interpretación está sustentada por modelos de  $V_p$  y  $V_s$  obtenidos también mediante sísmica de alto ángulo, de los cuales se derivó la distribución bidimensional de la razón de Poisson en el outer rise. Debido a la infiltración de agua a través de las fallas normales expuestas en la zona del outer rise, la litosfera oceánica presenta un alto grado de hidratación. Este proceso es presumiblemente intensificado por la existencia de un monte oceánico en el área. Se concluye que el agua se infiltra hasta grandes profundidades dentro de la litosfera, gatillando sísmos someros en el outer rise y probablemente produciendo serpentización en el manto, estimada alrededor del 10%.

---

# Erklärung

Hiermit erkläre ich, dass die von mir für das Promotionsverfahren vorgelegte Abhandlung “Seismic structure off- and onshore Maule, constraints for megathrust earthquakes in central Chile”, abgesehen von der Beratung der Betreuer nach Inhalt und Form, meine eigene Arbeit ist. Bisher ist die Arbeit noch nicht an anderer Stelle im Rahmen eines Prüfungsverfahrens vorgelegt worden. Die Arbeit ist unter Einhaltung der Regeln guter wissenschaftlicher Praxis der Deutschen Forschungsgemeinschaft entstanden.

Eduardo Moscoso

---

# Contents

<b>1</b>	<b>Introduction</b>	<b>1</b>
1.1	Seismogenic zone . . . . .	3
1.2	Seismotectonic background . . . . .	5
1.2.1	Regional tectonic setting . . . . .	5
1.2.2	Earthquake activity in central Chile . . . . .	7
1.3	Objectives of the study and agenda . . . . .	9
<b>2</b>	<b>Modeling strategy</b>	<b>13</b>
2.1	Forward ray tracing . . . . .	13
2.2	Inverse problem . . . . .	14
2.3	Starting model . . . . .	18
2.4	Multilayer inversion: top to bottom approach and layer stripping . . . . .	18
<b>3</b>	<b>Margin seismic structure</b>	<b>21</b>
3.1	Abstract . . . . .	21
3.2	Introduction . . . . .	22

---

3.3	Tectonic setting . . . . .	23
3.4	Seismic experiment and data . . . . .	26
3.5	Tomographic inversion scheme . . . . .	28
3.6	Resolution of the velocity model . . . . .	30
3.7	Results . . . . .	32
3.8	Discussion and conclusions . . . . .	34
3.8.1	Relationship between the updip and the backstop. . . . .	34
3.8.2	Maule earthquake nucleation zone . . . . .	36
<b>4</b>	<b>Outer rise seismic structure</b>	<b>39</b>
4.1	Introduction . . . . .	39
4.2	Tectonic framework . . . . .	41
4.3	Seismic experiment and data . . . . .	43
4.3.1	Local earthquake data . . . . .	43
4.3.2	Wide-angle seismic data . . . . .	44
4.4	Velocity field modeling procedure . . . . .	45
4.4.1	P wave traveltimes tomography . . . . .	45
4.4.2	S wave traveltimes tomography . . . . .	47
4.5	Velocity model assessment . . . . .	48
4.5.1	Model uncertainty . . . . .	48
4.5.2	Resolution tests . . . . .	50
4.5.3	Velocity-Depth ambiguity . . . . .	50

4.6	Discussion . . . . .	54
4.6.1	Seismic structure of the oceanic crust in the trench outer rise region	54
4.6.2	Crustal thickness . . . . .	57
4.6.3	Hydration of the oceanic lithosphere and upper mantle serpentinization . . . . .	57
4.6.4	Upper mantle anisotropy . . . . .	59
4.6.5	Outer rise seismic activity . . . . .	60
4.7	Conclusions . . . . .	63
<b>5</b>	<b>Final discussion</b>	<b>65</b>
5.1	Seismogenic zone in the Maule region and 2010 earthquake nucleation zone	65
5.2	Seismic structure of the upper oceanic lithosphere and hydration . . . . .	66
5.3	Outer rise seismicity . . . . .	67
<b>A</b>	<b>Seismic sections</b>	<b>81</b>
<b>B</b>	<b>Data picks used for Vp modeling</b>	<b>101</b>
<b>C</b>	<b>Data picks used for Vs modeling</b>	<b>107</b>
<b>D</b>	<b>Earthquake data examples and hypocenter sensitivity test</b>	<b>109</b>
<b>E</b>	<b>Moho geometry test</b>	<b>113</b>
E.1	Flat Moho v/s curved Moho . . . . .	113
E.2	Velocity-Depth ambiguity test . . . . .	115





# List of Figures

1.1	<i>The subduction factory (modified from Tatsumi and Stern, 2006)</i> . . . . .	2
1.2	<i>Perspective view of the seismogenic zone. It is characterized by large areas of asperities that fail in a frictionally unstable or velocity weakening manner (modified from Dixon and Moore, 2007)</i> . . . . .	4
1.3	<i>a) Central Chile tectonic setting, governed by the subduction of the Nazca plate beneath the south American plate; b) Depth of the Chilean trench axis; c) Age of the Nazca and Antarctic plates at the trench axis. (Figures b and c are modified from (Contreras-Reyes and Osses, 2010))</i> . . . . .	6
1.4	<i>Compilation of historical earthquakes along the Chilean margin A) Main bathymetric and topographic features, and rupture areas of the events; (B) Rupture areas extension along strike of the events with <math>M &gt; 7</math> (after Contreras-Reyes and Carrizo, 2011)</i> . . . . .	8
2.1	<i>Example of the top to bottom approach for the Nazca oceanic plate. Successive inversions with stepwise offset increment were computed in order to constrain the shallowest part before inverting the deepest part of the model.</i> . . . . .	19
3.1	<i>(Top) Map of the central Chile region. The red box outlines the rupture area estimated from the aftershocks of <math>M_w &gt; 4.0</math> between 27th of February and 1st of August 2010, reported by NEIC catalogue . (Bottom) Stations location and shooting line of the profile(in black).</i> . . . . .	25

---

3.2	<i>(Top) Record sections of OBS 327 (left) and OBH 004 (right). Time axis is reduced by 6 km/s. (Center) Record sections with superimposed travel times. (Bottom) Situation of the seismic stations on the bathymetry used for the modeling and seismic reflectors modeled. Data example stations are represented by green triangles. . . . .</i>	27
3.3	<i>Record sections of OBH 314, located in the trench outer rise area. . . . .</i>	28
3.4	<i>Results of the checkerboard tests. For each sub-plot: the top Figure shows the synthetic resolution pattern, and the bottom the recovery. The sizes of the anomalies are (horizontal by vertical extent) a) 2.5 X 2.5 km; b) 10 X 5 km; c) 20 X 10 km; d) 40 X 20 km . . . . .</i>	31
3.5	<i>Traveltime tomography of the forearc offshore Maule and its seismic interpretation based on the comparison of our results with the structure of the margin offshore Arauco (Contreras-Reyes et al., 2008a) . . . . .</i>	33
3.6	<i>a) Frequency histogram of the aftershocks projected on the profile; b) Traveltime tomography of the profile masked by the seismic ray paths. The overall residual time of the model is 0.103 ms (<math>\chi^2 = 1.1</math>); c) Derivative weight sum (DWS). . . . .</i>	35
3.7	<i>Geological interpretation of the study area. AP stands for accretionary prism. The red thick line corresponds to the estimated seismogenic zone, and the white segmented line to the aseismic zone. The orange dots on the bathymetric map indicate the deformation front and the yellow ones the projection of the backstop front. . . . .</i>	37
4.1	<i>(Top) High resolution bathymetric map offshore Maule region. The solid lines represent the transects P03 and P04, the green dots show the stations locations for the wide-angle experiment and the white triangles represent the position of the local seismic network. Station 229, represented by a green triangle, was used for both experiments. At the bottom the OBS/OBH locations are plotted on the bathymetry. . . . .</i>	42

4.2	<i>Examples of wide-angle seismic data recorded by the hydrophone (top) with manually picked arrivals and predicted traveltimes using the average 2D final models (center) and the correspondent rays (bottom), for a) Vp model and, b) Vs model.</i>	46
4.3	<i>a) Initial models used for the Monte Carlo inversion procedure for Vs (left) and Vp (right). The gray area shows the range of the initial Moho depth for the reflector's inversion b) Example of the delay between Pg and PPS phases recorded by the radial component of OBS 405.</i>	47
4.4	<i>Nomenclature for converted seismic phases, modified after Au and Clowes (1984).</i>	48
4.5	<i>a) Error for the Vp model and Moho reflector; b) Error for the Vs model; c) DWS for Vp model; d) Poisson's ratio error derived from equation 4.2.</i>	49
4.6	<i>Resolution tests for a) Vp model; b) Vs model.</i>	51
4.7	<i>Final velocity models for Vp (Top). Vs (Center) and Poisson's ratio (Bottom) using a flat moho and a kernel <math>\omega = 0,01</math>, this test shows a velocity-depth trade off for the lower crust. The red dots correspond to the OBS locations, and CP stands for the crossing point with profile P03. The overall error for the models is 95 ms for Vp and 92 ms for Vs.</i>	53
4.8	<i>Final velocity model derived from averaging all Monte Carlo ensembles for a) Vp and b) Vs, c) <math>v</math> masked by the intersection of rays of the P and S wave velocity models. CP in a) stands for the crossing point with P03.</i>	56
4.9	<i>a) Velocity model of P03, the segmented line CP denotes the crossing point with P04. b) Velocity profiles extracted from the locations of A1 and A2 in a) and the red profile was extracted beneath the crossing point (CP) in profile P04 (Figure 4.8a)</i>	58

---

4.10	<i>a) Aftershocks of the Maule earthquake: yellow dots represent the events up to 3 months after the main shock from NEIC catalogue and the white stars stand for outer rise events with Magnitude higher than 5 within one year after the earthquake, with its respective Harvard CMT fault plane solutions. The black solid lines mark the locations of the profiles P03 and P04. The local earthquakes recorded by our outer rise network operative between March and April of 2008, are represented by red dots. Their projection over P03 and P04 are in b) and c), respectively. . . . .</i>	62
5.1	<i>a) Map showing the seismicity prior to the Maule earthquake from NEIC prior (green dots) and after the Maule earthquake (yellow), ORN (red dots) and CMT catalog (Compressional earthquake with <math>M_w = 5.3</math>); b) Slip distribution from Lorito et al. (2011), and its spatial correlation with the outer rise seismicity during the co-seismic period. The focal mechanisms correspond to events in the outer rise with <math>M_w &gt; 5.0</math>. . . . .</i>	67
D.1	<i>Results of the hypocenter sensitivity test. . . . .</i>	110
D.2	<i>Waveforms from two events occurred in the outer rise area and full covered by the ORN. Red bars stand for S-wave arrivals and the blue ones for P-wave arrivals. The number on the left side of each waveform stands for the obs code and the letter for the component: H: Hydrophone, S1: Horizontal component 1, S2: Horizontal component 2 and Z: Vertical component. . . . .</i>	111
D.3	<i>(Figure D.2 Continuation). . . . .</i>	112
E.1	<i>Results of the moho geometry test. A simple velocity model was used to test 2 different geometries: a flat Moho (red) and the curved Moho obtained from the tomographic inversion procedure (green). The ray paths for the Moho reflections, for each station and geometry are plotted over the model. Two stations were used a) OBS 229 and b) OBS 406. The result of this test shows that the arrivals observed (blue bars) are best explained by travel times calculated with the curved Moho (green dots) than with the flat one (red dots). . . . .</i>	114

E.2 *Results of the velocity-depth ambiguity test. Successive inversions were performed using the starting model of a) and varying the depth kernel to: b)  $\omega = 10$ , c)  $\omega = 1$  and d)  $\omega = 0.01$ . The overall final error is 95 ms, 56 ms and 58 ms, respectively. . . . . 115*

F.1 *Since the only ray paths that illuminate the lower part of the continental crust considered during this layer's inversion are reflections, here we present two different tomographic images that fit the data picks ( $\chi^2 = 1$ ) given two different initial lower crust velocities, and how they affect the top of the oceanic crusts (TOC) geometry: a) When the velocity of the lower crust is between 6-6.7 km/s, the TOC has a dipping angle close to 10, which is the same angle modeled below the trench and accretionary prism, which is well constrained by refractions and reflections. b) When velocity of the layer at the bottom is 7.3 Km/s (which can be interpreted as the rising of the continental mantle), the reflector tends to increase the subduction angle. . . . . 118*

F.2 *From the models of Figure F.1, we analyzed the effect of varying the slope in the vicinity of the reflector obtained from the inversion at the zone where we have no refraction rays illuminating the lower part of the crust. In Figure a) Ten different reflector models are presented. The segmented line represents the reflectors with ( $\chi^2 = 1$ ) and the solid blue lines correspond to the reflectors which adjust the data. In Figure b) the same analysis is carried out for the model with higher velocity at the bottom of the crust. Figure c) shows the RMS error of all the reflectors. The brown zone shows the pick uncertainties for PmP phases (120 ms). The TOC reflectors which satisfy the error criteria are plotted together in Figure d). . . . . 119*

---

# List of Tables

4.1	Summary of data picking information and statistics of the fitness between the final average models and picks . . . . .	44
D.1	<i>1D velocity models used for the second part of the sensitivity test, for three different relocations.</i> . . . . .	110

---



# Chapter 1

## Introduction

Subduction is the process that takes place at convergent boundaries by which one tectonic plate moves under another tectonic plate, sinking into the Earth's mantle as the plates converge. A subduction zone is an area on Earth where two tectonic plates move towards one another and subduction occurs. Subduction zones are often noted for their high rates of volcanism, earthquakes and mountain building. This is because subduction processes result in melting of the mantle, producing a volcanic arc as relatively lighter rock is forcibly submerged (*Stern, 2002*).

The sinking of lithosphere in subduction zones and convection in the asthenosphere provide most of the force needed to drive plates, and cause mid oceanic ridges to spread, with the result that plate tectonics and subduction zones are surficial and interior expressions of Earth's dominant tectonic mode. Subduction zones are also Earth's largest recycling system and therefore have been compared with an industrial plant: "The subduction factory" as shown in Figure 1.1. Subduction zones deliver raw materials to the subduction factory, where oceanic lithosphere, sediments, and seawater reequilibrate with ambient mantle, triggering melting and incidentally creating continental crust. What is not recycled in the upper few hundred kilometers of a subduction zone likely sinks to the core-mantle boundary, where this residue may be reheated for around a billion of years until it is restructured as a mantle plume (*Stern, 2002*).

In addition to playing the central role in Earth tectonics, melt generation and crustal evolution, subduction zones profoundly impact society. Large earthquakes, violent erup-

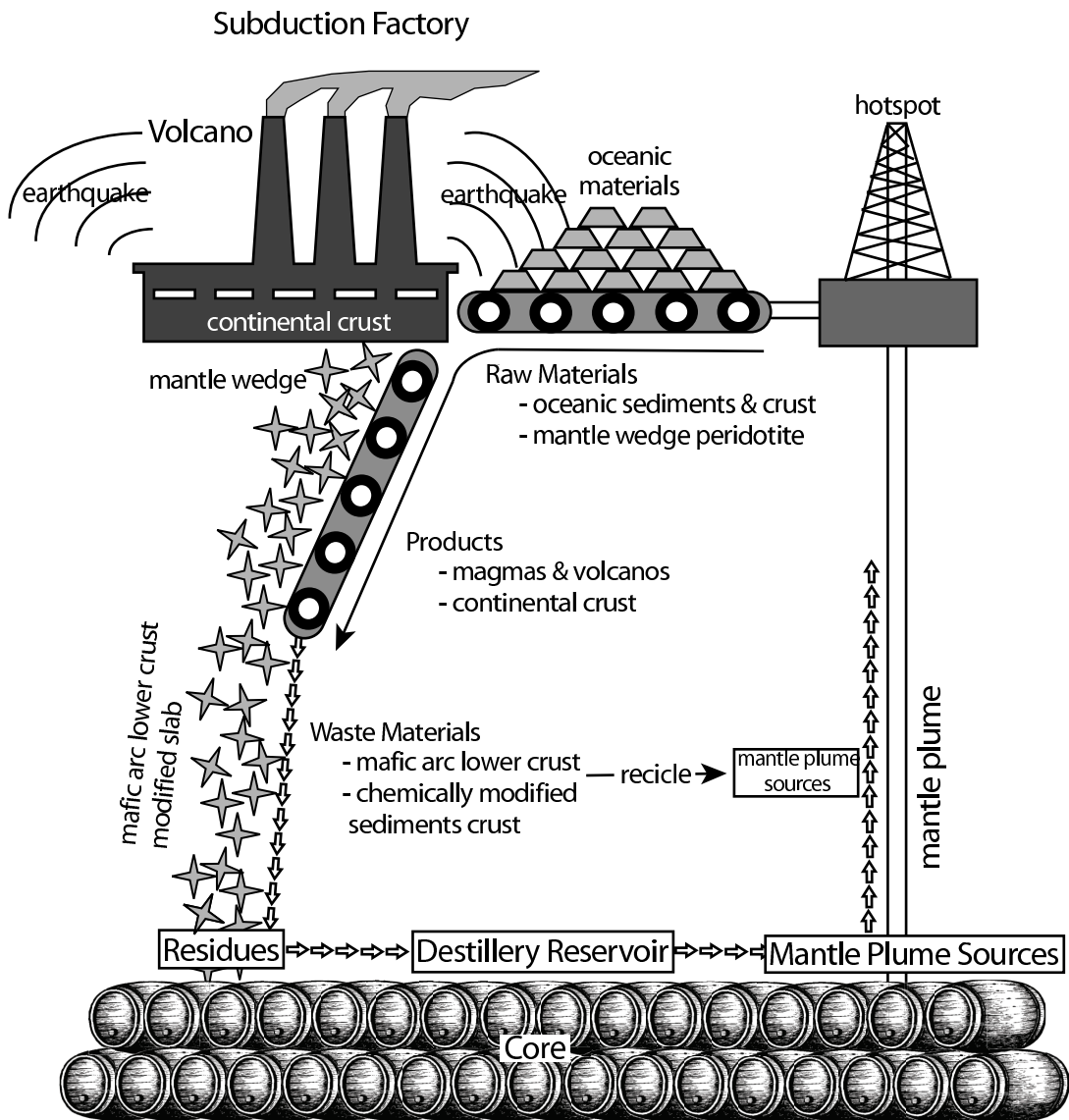


**Figure 1.1:** *The subduction factory (modified from Tatsumi and Stern, 2006)*

tions and destructive tsunamis occur preferentially in subduction zones, threatening most of Earth's population. In the other hand, these zones host by far most of planet's ore resources. Thus understanding the processes related to subduction zones has a direct impact on the life quality of billions of people.

The central Chile subduction zone has been of great interest for scientists because is one of the most seismically active convergent margins in the world. Since 1973, there have been 13 events of magnitude 7.0 or greater. As a matter of fact, it hosted the largest earthquake ever measured in 1960 and recently the sixth largest earthquake registered up to now, of magnitude  $M_w=8.8$  that hit the Maule region the 27/02/2010. Both quakes produced a large tsunami wave that devastated not only the Chilean continental coast, but also the insular part. In the case of the 1960 earthquake, it also affected areas throughout the Pacific Ocean as far away as Japan, producing thousands of casualties and billions of dollars in material losses.

The results exposed on this dissertation are in the framework of the project SFB574 "Volatiles and Fluids in Subduction Zones Climate Feedback and Trigger Mechanisms for Natural Disasters" led by the University of Kiel, with close collaboration of several Chilean partners. It has the purpose of studying the seismic structure of the oceanic plate prior to its subduction and of the continental margin, and determine constraints for the geodynamic processes related to the subduction offshore the Maule region in central Chile.

As a mode of introductory frame to the work presented here, in the following is given a deeper explanation of the relevant concepts related to subduction zones and the tectonic that governs the geodynamics of the area under study.

### **1.1 Seismogenic zone**

The seismogenic zone is the portion of the plate interface, of subduction thrust faults, that produces earthquakes by stick-slip sliding. Its rupture produces most of large earthquakes and tsunamis globally. In a "stick-slip" frictional mechanics model, stress and strain accumulate during the interseismic period ("stick"), and is suddenly released producing considerable "slip".

Since the magnitude of earthquakes increases systematically with the fault rupture

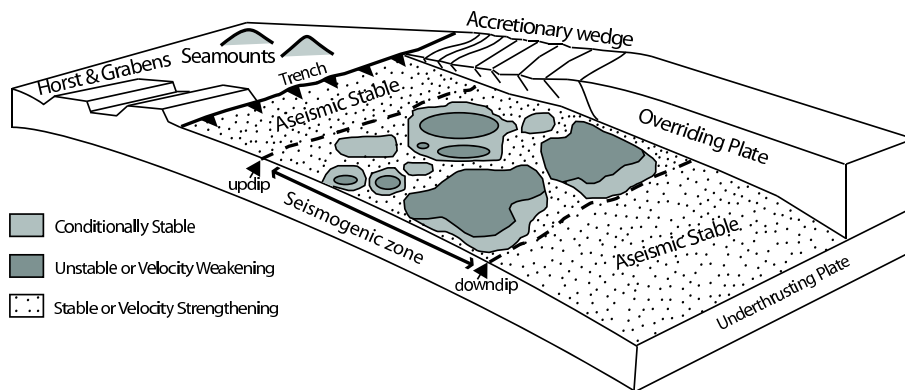


**Figure 1.2:** *Perspective view of the seismogenic zone. It is characterized by large areas of asperities that fail in a frictionally unstable or velocity weakening manner (modified from Dixon and Moore, 2007)*

area, subduction thrusts producing  $M < 7.5$  earthquakes probably have seismic behavior only in small patches, at most a few tens of kilometers across, whereas large subduction earthquakes have seismic rupture that may be over areas of  $\sim 100$  km downdip and  $\sim 1000$  km along strike. An example of this is the 1960 megathrust earthquake in south central Chile ( $M_w=9.5$ ). This patch receives the name of “Seismic asperity”, and is often inferred to be “stronger” than the surrounding region of the thrust, accommodating therefore most of the plate convergence seismically, while adjacent areas have more aseismic slip.

Both small and large thrust events usually do not extend to the trench; there is an updip aseismic zone. *Byrne et al.* (1988) suggested that the part of the thrust in contact with accreted sediments is aseismic. This stable sliding between the plates is probably allowed by the presence of overpressured and unconsolidated sediments in the plate boundary. Seismic behavior should then start landward of the thrust contact with the crystalline crust of the overlying forearc. The transition zone between unconsolidated and crystalline rock is called “Backstop”. Another mechanism suggested to control the updip, is the clay content of the subducted sediments in the fault gouge (*Marone and Scholz, 1988*). Subducted sediments change its rheological properties with temperature, when smectite changes to illite, producing a loose of their lubricating capacity. This process typically occurs approximately in the isotherm between  $100^\circ\text{C}$  to  $150^\circ\text{C}$  (e.g., *Oleskevich et al., 1999*), which usually corresponds to depths on the order of 5-15 km (*Hyndman et al., 1997*).

The downdip limit of the seismogenic zone is defined by the reappearance of weak

rocks, either because they are hot (reaching temperatures greater than  $350^{\circ}\text{C}$ ) or are intrinsically weak, such as serpentinite. Several subduction zones in the world (Kermadec, the Solomons, Japan, South Peru and Kamchatka) present double seismogenic zones (Pacheco *et al.*, 1993), manifesting an upper seismogenic zone along the plate interface with a downdip limit defined by the appearance of serpentinite beneath the forearc Moho and a lower, intraslab seismogenic zone having an updip limit defined by the disappearance of serpentinite and a lower limit defined by the  $350^{\circ}\text{C}$  isotherm in dry peridotite. The depth where the  $350^{\circ}\text{C}$  isotherm is reached strongly depends on the age of the lithosphere subducted: while for young lithosphere it is reached at relatively shallow depths along the subduction interface (e.g., SW Mexico), for old lithosphere, this temperature is not reached until well below the forearc Moho. In most of subduction zones, the seismogenic zone ends at the Moho. This implies that mantle beneath the forearc is unusually weak, most likely because it is pervasively serpentinitized by fluids from the subducted slab. The downdip limit determines the landward extent of the seismic source zone, which is important for great earthquake hazard at inland localities.

## 1.2 Seismotectonic background

### 1.2.1 Regional tectonic setting

In central Chile, the incoming oceanic lithosphere of the subduction zone comprises both the Nazca Plate to the north and the Antarctic Plate to the south of the Chile Rise. The Chilean subduction zone is composed of two major segments defined by the incoming oceanic plate formed at two different spreading centers: north of the Valdivia Fracture Zone (FZ) the oceanic lithosphere was formed at the Pacific-Farallon spreading center more than 20 Ma ago (Müller *et al.*, 1997), whereas south of the Valdivia FZ it was created at the Chile Rise within the last 20 Ma (Herron *et al.*, 1981). North of the Valdivia FZ, the seafloor spreading fabric of the Nazca plate strikes approximately  $45^{\circ}$  to the trench axis, whereas south of the Valdivia FZ it strikes  $\sim 15^{\circ}$  to the trench axis. The Chile trench, Mocha and Valdivia FZs define a triangle called the Mocha block, which is an area of high stress concentration on the plate interface that acts as a boundary between two major segments of the Chilean subduction zone (Barrientos and Ward, 1990). Part of the northern block, offshore Maule, is the object of study of the present thesis.

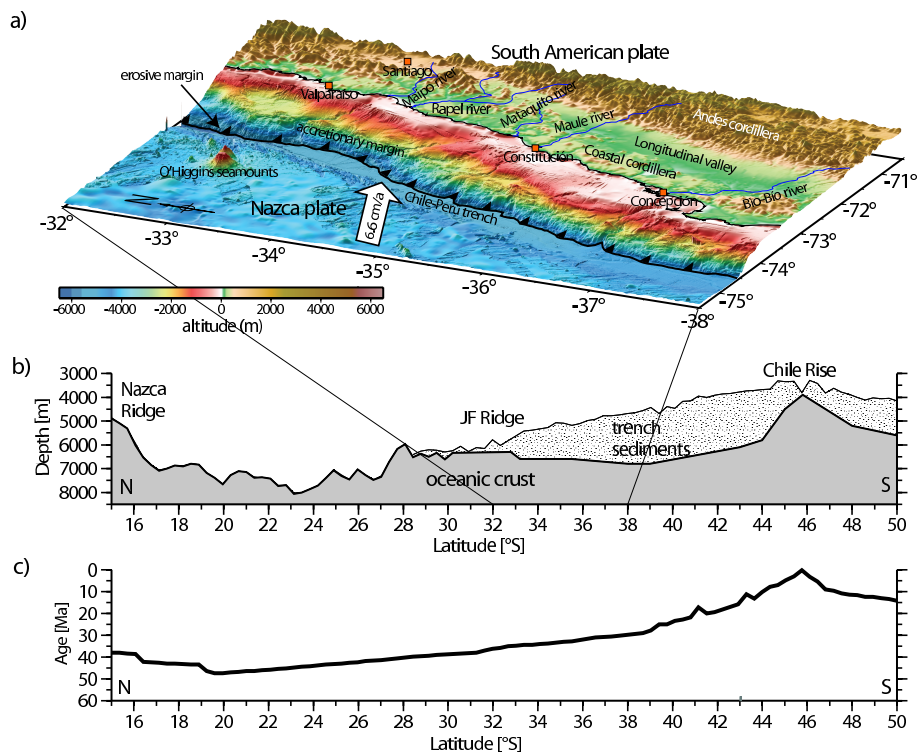


**Figure 1.3:** a) Central Chile tectonic setting, governed by the subduction of the Nazca plate beneath the south American plate; b) Depth of the Chilean trench axis; c) Age of the Nazca and Antarctic plates at the trench axis. (Figures b and c are modified from (Contreras-Reyes and Osses, 2010))

The Chile Rise encounters the overriding continental South American Plate to form the Chile Triple Junction at  $46.5^{\circ}\text{S}$ . The half spreading rate at the Chile Rise is  $31\text{ mm/a}$  since  $5\text{ Ma}$ , but back to  $25\text{ Ma}$  varied between  $38$  and  $61\text{ mm/a}$  (Tebbens *et al.*, 1997). The spreading center is actively subducting south of the Chile Triple Junction. North of the triple junction the Nazca Plate subducts beneath the South American Plate at a rate of  $66\text{ mm/a}$  directed at  $\text{N}78^{\circ}\text{E}$  (DeMets *et al.*, 1994, Angermann *et al.*, 1999). The Chile Margin strikes around  $\text{N}95^{\circ}\text{E}$ . Thus the plate convergence in this region is  $\sim 15^{\circ}$ . Active spreading at the Chile Rise implies that the subducting lithosphere is young. The age of the Nazca Plate directly at the Chile Margin ranges from  $0$  at the triple junction to about  $30\text{-}35\text{ Ma}$  offshore Maule (Figure 1.3c). Several fracture zones divide the Nazca Plate into segments of distinct ages at the trench.

The composition of the overriding part of the South American Plate is divided into

the Coastal Platform (Cenozoic marine and continental sediments), the Coastal Cordillera (crystalline basement of Palaeozoic accretionary complex and magmatic arc), the Central Depression or Longitudinal Valley (Pliocene-Quaternary sediment filled basin), and finally the Andes Cordillera (active volcanic arc) (*Melnick et al.*, 2006), as shown in Figure 1.3a. The primary geologic units exposed on land along the southern Chile coast are the continental basement rocks that are part of a Paleozoic accretionary complex and magmatic arc (*Mordojevich*, 1974, *Hervé et al.*, 1988). The southern central Chile trench is filled with terrigenous sediments sourced from the Andes (*Thornburg and Kulm*, 1987). The deposited material is transported through submarine canyons and redistributed within the trench from south to north as shown in Figure 1.3b (*Thornburg et al.*, 1990, *Völker et al.*, 2006).

### 1.2.2 Earthquake activity in central Chile

Seismologically, south central Chile represents one of the most active regions in the planet, with large to giant megathrust earthquakes occurring every 130 to 300 yr. The historical seismicity of central Chile between 32°S and 39°S has been studied based on local reports, geological information, level changes, seismic data, etc. The whole area has ruptured repeatedly since 1647, the largest earthquakes being that of 1730 and that of 22 May 1960. The Chillán earthquake of 1939, was not a subduction zone shock, but an earthquake that broke the downgoing slab under the Longitudinal Valley of Chile. The area from 35°S to 37°S has suffered at least three large events in 1730, 1751, 1835 and, partly, in 1928. Although there are some doubts about the southern termination of the 1928 event, it is clear that the southern part of the Concepción-Constitución area had had no major subduction earthquakes since 1835 (*Campos et al.*, 2002) as can be seen in the updated compilation of historic events made by *Contreras-Reyes and Carrizo* (2011) presented in Figure 1.4.

The southern part of central Chile was the site of the largest historic earthquake of 22 May 1960 in magnitude larger than 9.5. The rupture area of this mega-thrust earthquake bounds the southern limit of the Concepción-Constitución seismic gap from the north down to 46°S near the Chile Triple Junction, comprising a rupture area of almost 1000 km long (*Cifuentes and Silver*, 1989, *Barrientos and Ward*, 1990). Two important magnitude 8 earthquakes, immediately to the north of the Concepción-Constitución area, are those of 1985 south of Valparaíso and that of Talca on 1 December 1928. The 1928 event produced

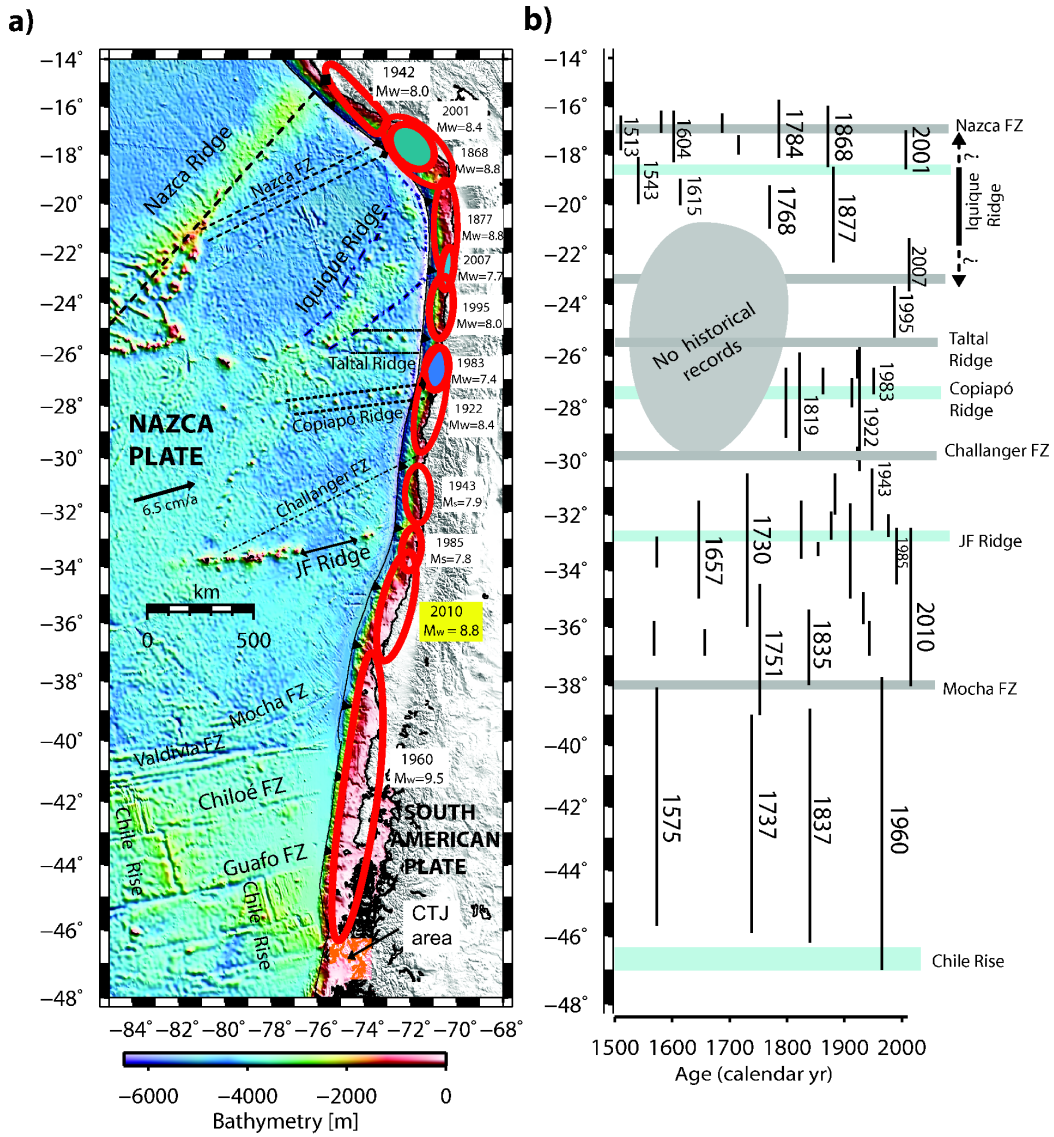


**Figure 1.4:** Compilation of historical earthquakes along the Chilean margin A) Main bathymetric and topographic features, and rupture areas of the events; (B) Rupture areas extension along strike of the events with  $M > 7$  (after Contreras-Reyes and Carrizo, 2011)



extensive damage along the coast from Cauquenes in the south ( $36^{\circ}S$ ) to Pichilemu in the north ( $34.5^{\circ}S$ ) and the cities of Talca, Curicó and San Fernando, in the Longitudinal Valley ( $35^{\circ}S$ ) (Figure 1.4). In their re-evaluation of large Chilean earthquakes, *Beck et al.* (1998) determined the depth and mechanism of the 1928 event. According to these authors, this earthquake was a shallow dipping thrust event with a centroid depth less than 20 km. The 1985 Valparaíso earthquake covered only partially the rupture zone of the great 1906 thrust earthquake, which in turn with the 1928 earthquake define the northern boundary of the Concepción-Constitución seismic gap.

The Concepción-Constitución area had been considered the oldest seismic gap in Chile, with a last large earthquake dating back to 1835 (*Darwin*, 1851). Recent seismic (*Campos et al.*, 2002) and GPS (*Ruegg et al.*, 2009) studies had confirmed the existence of a seismic gap between  $35^{\circ}S$  to  $37^{\circ}S$ , estimating the occurrence of a megathrust earthquake of magnitude  $M_w=8.5$  in the area. Thus, the 2010 Maule earthquake released more than 175 years of seismic energy accumulated. It struck at  $35.909^{\circ}S$ ,  $72.733^{\circ}W$  just offshore the coast of the Maule Region on February 27 at 03:34 local time (06:34 UTC), rating a magnitude of 8.8 on the moment magnitude scale, and lasting up to 3 minutes. The earthquake triggered a tsunami which devastated several coastal towns in central Chile and Juan Fernández Islands, some 700 km offshore.

### 1.3 Objectives of the study and agenda

The main topic of this thesis is the evolution of the seismic properties of the oceanic Nazca plate prior and during subduction offshore Maule, and its relation to the updip of the seismogenic zone and outer rise seismicity. Between March and April of 2008, seismic data was acquired aboard the British vessel RV James Cook in the JC23 cruise. The seismic experiment consisted in a total of 11 wide-angle profiles, including three amphibious, and two local seismic networks: an outer rise network that operated during 5 weeks and an amphibious network that recorded about 9 months of data. Additionally, multibeam high resolution bathymetric data was recorded from  $32^{\circ}S$  to  $38^{\circ}S$ . In this thesis earthquake data from the short term outer rise local network, one amphibious and one trench outer rise wide-angle profiles were modeled and interpreted in order to infer the seismic structure of the oceanic lithosphere and the continental margin, up to a maximum depth of approximately 15 km.

---

Chapter 2 describes the methodology and the mathematical approach used in this work to obtain the seismic velocity distribution and the geometry of the reflectors. For the modeling the joint refraction and reflection traveltime tomographic method (*Korenaga et al.*, 2000) was employed. This method computes simultaneously the velocity distribution and the reflector's geometry for a single layer. In this chapter, the inversion procedure is also explained, as well as the "Layer stripping approach", used for extending the single layer inversion to a multi layered seismic structure. For analyzing the uncertainties of the final models, different approaches were employed, depending on the nature of the zone analyzed. The uncertainties of the model presented in Chapter 3, comprising the area between the trench outer rise up to the continent, were estimated by performing checkerboard tests with synthetic velocity anomalies of different wavelengths. For the error estimation of the model of the trench outer rise area, presented in Chapter 4, a Monte Carlo-like approach that calculates the inversion of a large number of realizations assuming the same probability for each of them, was used.

Chapter 3 and 4 are presented in the format of stand alone scientific articles. Chapter 3 presents the study entitled "**Revealing the deep structure and rupture plane of the 2010 Maule, Chile Earthquake (Mw=8.8) using wide angle seismic data**", published in *Earth and Planetary Sciences Letters* (EPSL)\*. It studies the relationship between the seismic structure of the central Chilean Margin between 35°S and 36°S and the updip of the seismogenic zone.

In Chapter 4 the seismic structure and evidence of hydration of the incoming plate offshore Maule, prior to its subduction is presented. Here the seismic structure of the Nazca plate, the influence of bending related plate faulting and of a neighboring seamount on the seismic properties of the lithosphere, the seismic anisotropy and possible serpentinization of the upper mantle are analyzed in depth. The aspects covered by this chapter are part of the article titled "**Outer rise fracturing of the incoming oceanic plate and its effect on lithospheric hydration and on the seismic activity: A study offshore Maule, Chile**", to be submitted to a special issue of the *International Journal of Earth Sciences* dedicated to the SFB574 Project.

Finally, a discussion of the results presented and general concluding remarks of this

---

\*Moscoso, E., I. Grevemeyer, E. R. Flueh, E. Contreras-Reyes, Y. Dzierma, W. Rabbel and M. Thorwart (2011), Revealing the deep structure and rupture plane of the 2010 Maule, Chile Earthquake (Mw=8.8) using wide angle seismic data, *Earth and Planetary Science Letters*, doi:10.1016/j.epsl.2011.04.025

dissertation are exposed in Chapter 5. Part of Chapter 4 and the final discussion of this thesis are integral part of the article under preparation: **“Outer rise seismicity related to the Maule, Chile 2010 Megathrust earthquake and hydration of the incoming oceanic lithosphere”**.

---

# Chapter 2

## Modeling strategy

The seismic studies presented here are based in the joint refraction/reflection traveltimes inversion method, implemented in the program TOMO2D (for further details, the reader is referred to *Korenaga et al.*, 2000, *Planert*, 2006, and references therein). In order to mimic the decreasing resolution at increasing depth, each model was parameterized as a dense 2-D grid of velocity nodes hanging beneath the sea floor. Nodes were parameterized by a spacing of 500 m horizontally and the vertical spacing increasing with depth from 100 m beneath the sea floor to 300 m at the base of the grid (40 km depth). The reflectors were parameterized as series of depth nodes with a spacing of 500 m and only one degree of freedom in the vertical direction. These reflecting interphases are defined as “floating reflectors”, since it is independent of specific velocity values or grid geometry. The starting geometry assigned to the reflector was determined by forward modeling.

### 2.1 Forward ray tracing

The forward step of the *Korenaga et al.* (2000) inversion method employs a hybrid approach. The first step is a graph theory approach, or shortest path method (e.g., *Dijkstra*, 1959), that searches for the ray path connecting each source-receiver combination that minimizes the travel time (*Moser*, 1991, *van Avendonk et al.*, 1998) as an approximation of Fermat’s principle. Graph methods introduce systematic errors in ray geometry and therefore in

---

calculation of traveltimes, yielding overestimation of velocities (e.g., *Moser, 1991*). This is because the rays are forced to travel through the velocity nodes, making a zig-zag in smooth velocity grids. For searching node connections, *Korenaga et al. (2000)* includes a forward star, which defines the structure of possible node connections. The bigger the search star, the more accurate rays, but also the larger computational times needed.

For computing the global minimum, the solution found by the graph method is used as a good initial guess for the ray path geometry, which is subsequently refined by the ray bending method, instead of using the graphic method with a bigger star, or equivalently, with a finer velocity grid. The ray bending method implemented in TOMO2D, uses the conjugate gradient for the minimization, because of its modest memory space requirements and its superior convergence properties in comparison with Newton's method or descent gradient method (*Moser et al., 1992*). The stopping criteria for the minimization is that residual travel time ( $t_{obs} - t_{calc}$ ) reaches a threshold.

In practical terms, it is possible to get acceptable traveltime calculations only using the graph method, but it has been shown that for simple geometries it takes more than 10 times more computational time than the hybrid method (*Korenaga et al., 2000*). Choosing a good initial ray path, it minimizes the calculation time for the bending method. To overcome the trade off between ray accuracy and computational time, several forward stars were tested for the geometry of the profiles, choosing finally the one that minimized the computing time for the hybrid ray tracing. For the case of both profiles, P03 and P04, the optimum size found for the search star was 5 by 10 nodes (horizontal by vertical, respectively).

## 2.2 Inverse problem

The traveltime residual  $\delta t_j$  is related to an infinitesimal perturbational model  $\delta u(r)$  by equation 2.1:

$$\delta t_j = \int_{P_j} \delta u(r) dr \quad (2.1)$$

For reflection traveltime residuals, they can be linearly related to slowness perturba-

tions and vertical changes in reflector depth by equation 2.2:

$$\delta t_j = \int_{P_j} \delta u(r) dr + \left. \frac{\delta T}{\delta z} \right|_{x=x_j} \delta z(x_j) \quad (2.2)$$

where,  $x_j$  is the reflecting point of the  $j$ th ray.

Equations 2.1 and 2.2 can be written in matricial form as:

$$d = G\delta m \quad (2.3)$$

where  $G$  is the Fréchet matrix containing the partial derivatives with respect to slowness,  $d$  is the data vector and  $\delta m$  the updated model vector.

Equation 2.3 is under-determined, hence smoothness constraints need to be applied as additional equations in order to obtain a unique solution. Gaussian smoothing within one decay length (correlation length) is used for each perturbational model parameter in all smoothing matrices (*Toomey and Foulger, 1989*). The correlation lengths are allowed to vary both in the horizontal and vertical direction. Since lateral variations in Earth's structure are usually much weaker than vertical ones, horizontal smoothing constraints are commonly chosen one order of magnitude bigger than corresponding vertical smoothing constraints, and thus the vertical and horizontal smoothing matrices (labeled  $C_{Vv}$  and  $C_{Hv}$  in the following) are applied separately (e.g., *van Avendonk et al., 1998, Toomey and Foulger, 1989, Korenaga et al., 2000*). To be consistent with the normalization in the Fréchet matrix, each smoothing equation for an individual model perturbation  $\delta m_i$  is normalized by the slowness of the starting model  $o^{u_i}$  (*Toomey and Foulger, 1989*) in equation 2.4.

$$\delta m_i o^{u_i-1} = \frac{\sum_{j=1}^m \beta_j \delta m_j o^{u_i-1}}{\sum_{j=1}^m \beta_j} \quad (2.4)$$

The weights  $\beta_j$  decrease with distance from the  $i$ th model parameter in a Gaussian distribution, given in equation 2.5

---


$$\beta_j = \exp \left[ \frac{(x_j - x_i)^2}{\tau_x^2} - \frac{(z_j - z_i)^2}{\tau_z^2} \right] \quad (2.5)$$

where  $\tau_x$  and  $\tau_z$  act as horizontal and vertical correlation lengths for the weights  $\beta_j$  to assure that only nodal positions lying within one correlation length of the particular model parameter are affected by the spatial smoothing constraints, i.e. are given non-zero weights. However, the horizontal and vertical correlation lengths of velocity variations within the Earth are a priori to a large extent unknown, which makes them a somehow arbitrary, but nonetheless quite effective choice to restrict the possible model space (e.g., *van Avendonk et al.*, 1998, *Toomey and Foulger*, 1989, *Korenaga et al.*, 2000).

Within an iterative approach, the regularization method applied here is "creeping" (*Shaw and Orcutt*, 1985), i.e. all constraints are operative on an individual model perturbation  $\delta m_i$  which is defined with respect to the solution of the previous iteration. So far, the above formulations contain no information about the original starting model, except for the normalization terms.

The corresponding forward problem in block matrix can then be written as:

$$\begin{pmatrix} d \\ 0 \\ 0 \\ 0 \end{pmatrix} = \begin{pmatrix} G_v & \omega G_d \\ \lambda_v C_{Hv} & 0 \\ \lambda_v C_{Vv} & 0 \\ 0 & \omega \lambda_d L_d \end{pmatrix} \begin{pmatrix} \delta m_v \\ \frac{1}{\omega} \delta m_d \end{pmatrix} \quad (2.6)$$

where subscripts  $v$  and  $d$  in equation 2.6 describe the velocity and depth sensitive components, respectively.  $\lambda_v$  and  $\lambda_d$  are the weights for the slowness and reflector depth perturbations which control the relative importance of the smoothing constraints with respect to the data misfit.  $C_{Hv}$  and  $C_{Vv}$  are the corresponding normalized smoothing matrices for velocity perturbations and  $C_d$  is the analogous smoothing matrix for reflector and depth perturbations.

The depth kernel weighting parameter  $\omega$  controls the relative depth sensitivity in the Fréchet matrix. The  $\omega$  parameter directly biases the inversion toward fitting reflector's travel time data with perturbations to either velocities in the lower crust or the depth of the reflector. For example, a value of  $\omega = 1$  equally weights both velocity and depth



node perturbations;  $\omega > 1$  ponders reflector changes over velocity changes;  $\omega < 1$  ponders velocity perturbations over reflector variations,  $\omega = 0$  just considers reflector changes and  $\omega \rightarrow \infty$  just considers velocity mesh changes. Because of the trade-off between media velocity and reflector depth (Korenaga, 2011) seismic travel time data possibly exhibit ambiguities that prevent the resolution of a time anomaly into reflector structure and media velocity. However, the existence of this ambiguity is a feature of the geometry of the subsurface and is not caused by the particular inversion algorithm (Tieman, 1994); Nevertheless, the inversion algorithm can be used to assess its extent in effectively exploring the possible solution space invoking a wide range of values for  $\omega$  as the single controlling parameter (Korenaga et al., 2000).

The solution for  $\delta_m$  in equation 2.6 is computed with the sparse matrix solver LSQR (Paige and Saunders, 1982). If the starting model is far from the initial model, calculated ray paths can be far from the true paths through the Earth. Model updates become quite large, taking the model update vector outside the region of linearity, i.e. traveltimes are predicted badly and the succeeding iterations could eventually become unstable. In order to remain within the region of linearity, equation 2.6 is augmented with additional damping constraints (equation 2.7).

$$\begin{pmatrix} d \\ 0 \\ 0 \\ 0 \\ 0 \\ 0 \end{pmatrix} = \begin{pmatrix} G_v & \omega G_d \\ \lambda_v C_{Hv} & 0 \\ \lambda_v C_{Vv} & 0 \\ 0 & \omega \lambda_d C_d \\ \alpha_v D_v & 0 \\ 0 & \omega \alpha_d D_d \end{pmatrix} \begin{pmatrix} \delta m_v \\ \frac{1}{\omega} \delta m_d \end{pmatrix} \quad (2.7)$$

were  $D_v$  and  $D_d$  are the velocity and depth damping matrices, which can be derived from a penalty function for the magnitude of model perturbation, and  $\alpha_v$  and  $\alpha_d$  are the individual weighting parameters which control their particular strength. Additionally, data outliers, i.e. synthetic traveltimes with misfits exceeding a predefined value, can be excluded from each linear inversion step.

Therefore, each inversion step must be small and is controlled by a total of the weighting parameters (two for damping and two for smoothing). After each inversion step, a solution is obtained that is closer to the minimum, but still lies within the limits of

---

linearity. Subsequently, new ray paths and traveltimes are computed with the new model and the inversion is initialized again. A series of these iterative steps can change an initial model dramatically if such a fit is required by the data.

## **2.3 Starting model**

Initial velocity models for the refraction lines were constructed from forward modeling. Specifically, for the outer rise it was a simple 1D model of the oceanic crust, based on the individual modeling for each station (E. Vera, personal communication). For the margin, a 2D approach was employed, as it involves a more complex seismic structure than the oceanic plate. For the water column a constant velocity of 1500 m/s was used to simplify traveltimes calculations, and the bathymetry was a track extracted from the high resolution bathymetric grid, sampled each 150 m (see Figure 1.3).

## **2.4 Multilayer inversion: top to bottom approach and layer stripping**

The inversion procedure employed is the top to bottom approach process that focusses first on the shallow structure where steep velocity gradients and lateral heterogeneity strongly influence phase arrival times (Figure 2.1). By inverting for deeper crustal structure from the top down, this method accounts for the systematic decrease in ray coverage with depth, thereby reducing the risk of smearing strong shallow anomalies into the lower crust. The offset limit started at 20 km, and was increased in steps of 10 km for the following inversions, until all the data was inverted. Each inversion step consisted in a maximum of 4 iterations, that stopped whether when the maximum iteration number was reached, or the overall residual traveltimes reached a value equal or smaller than the data uncertainty ( $\chi^2 \leq 1.0$ ). The single layer tomographic inversion already described, was generalized for a multilayer media using the "layer-stripping". It consists of inverting the top layer first, and the following layer later, fixing the upper section of the model with a weight of 1000 compared to the deeper section.

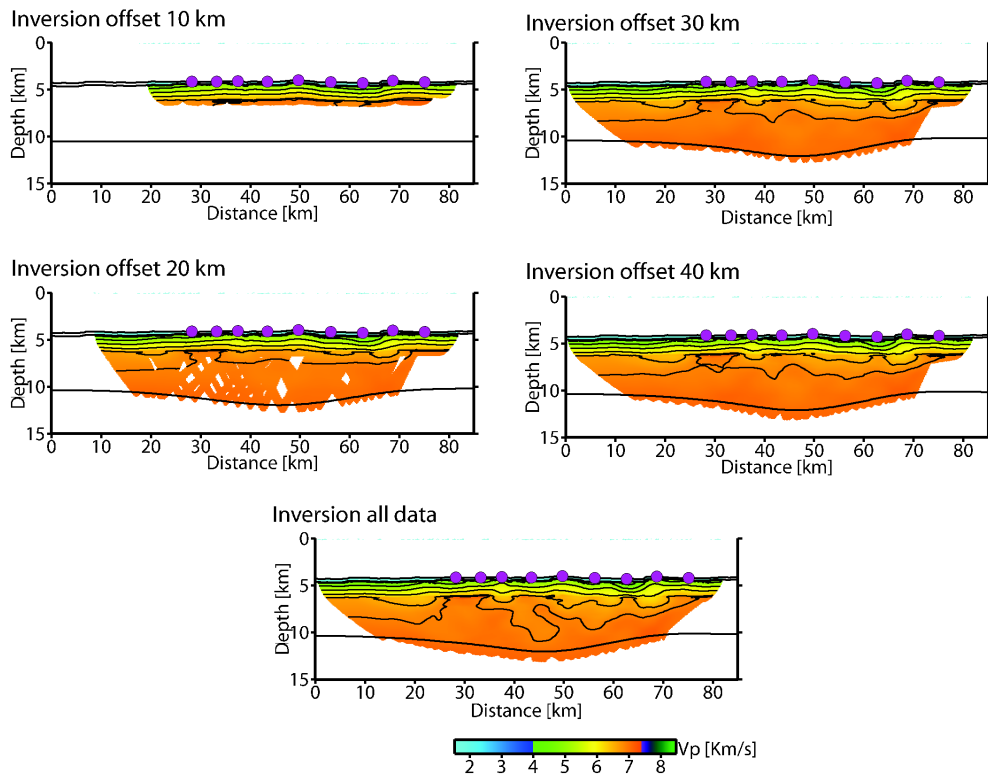


**Figure 2.1:** Example of the top to bottom approach for the Nazca oceanic plate. Successive inversions with stepwise offset increment were computed in order to constrain the shallowest part before inverting the deepest part of the model.

---

# Chapter 3

## Margin seismic structure

### 3.1 Abstract

The 27 February, 2010 Maule earthquake ( $M_w = 8.8$ ) ruptured  $\sim 400$  km of the Nazca-South America plate boundary and caused hundreds of fatalities and billions of dollars in material losses. Here we present constraints on the fore-arc structure and subduction zone of the rupture area derived from seismic refraction and wide-angle data. The results show a wedge shaped body  $\sim 40$  km wide with typical sedimentary velocities interpreted as a frontal accretionary prism (FAP). Landward of the imaged FAP, the velocity model shows an abrupt velocity-contrast, suggesting a lithological change which is interpreted as the contact between the FAP and the paleo accretionary prism (backstop). The backstop location is coincident with the seaward limit of the aftershocks, defining the updip limit of the co-seismic rupture and seismogenic zone. Furthermore, the seaward limit of the aftershocks coincides with the location of the shelf break in the entire earthquake rupture area ( $33^\circ S - 38.5^\circ S$ ), which is interpreted as the location of the backstop along the margin. Published seismic profiles at the northern and southern limit of the rupture area also show the presence of a strong horizontal velocity gradient (seismic backstop) at a distance of  $\sim 30$  km from the deformation front. The seismic wide-angle reflections from the top of the subducting oceanic crust constrain the location of the plate boundary offshore, dipping at  $\sim 10^\circ$ . The projection of the epicenter of the Maule earthquake onto our derived interplate boundary yielded a hypocenter around 20 km depth, this implies that this earthquake

---

nucleated somewhere in the middle of the seismogenic zone, neither at its updip nor at its downdip limit.

## 3.2 Introduction

The Chile subduction zone is among the most active convergent margins on earth, producing a large earthquake ( $M_w > 8.0$ ) every  $\sim 10 - 20$  years. These large earthquakes also cause significant vertical motion that can generate devastating tsunamis (*Bilek, 2009*, and references therein), as occurred during the devastating 27 February 2010 earthquake in Chile. This earthquake hit the south central part of Chile producing a tsunami which affected not only the continental central Chilean coast, but also the Juan Fernández Islands located some 670 km offshore. It caused more than 500 casualties and billions of dollars in material losses. The epicenter of this earthquake was preliminary located by the US Geological Survey (USGS) catalogue at  $35.97^\circ S$  and  $72.87^\circ W$  (<http://earthquake.usgs.gov/regional/world/historical.php>) offshore of the Chilean Maule region. The rupture zone, estimated by the USGS aftershocks (Figure 3.1), covers a distance of approximately 500 km long between the Juan Fernández Ridge (JFR) in the north and the Mocha Fracture Zone in the south (Figure 3.1). The distribution of the aftershocks of the Maule earthquake (<http://neic.usgs.gov>) suggests that the rupture area of this megathrust earthquake is larger than the so-called mature seismic gap between Constitución and Concepción ( $35^\circ S - 37^\circ S$ ) inferred from local seismological (*Campos et al., 2002*) and geodetic data, whose rupture estimated would produce a  $M_w = 8.5$  event (*Ruegg et al., 2009*). This segment ruptured in 1835 and the earthquake's effects were studied and described by Charles Darwin more than 160 years ago (*Darwin, 1851*).

The seismogenic zone along the subduction interface does not normally extend all the way to the trench axis and the shallowest part of the plate interface is considered to be seismically decoupled (*Byrne et al., 1988, Obana et al., 2003, ?*). The aseismic region of the subduction interface, located seaward of the updip limit of the seismogenic zone, is considered to be caused by the presence of high pore fluid pressure within unconsolidated sediments (the accretionary prism) which approach lithostatic pressure, resulting in a substantial decrease in effective normal stress. Low effective normal stress results in low shear strength along the subduction interface, which in turn means that the accretionary prism does not accumulate strain that is released as sudden slip during large earthquakes

(e.g., *Byrne et al.*, 1988). Thus, the updip limit of the seismogenic zone is expected to be coincident with the landward limit of the accretionary prism (*Byrne et al.*, 1988, *Contreras-Reyes and Osses*, 2010).

Seismic refraction and wide-angle data collected in 2008 offshore the Maule region provide a unique opportunity to gain insights into the seismic structure and geometry of the co-seismic rupture area of the Maule megathrust earthquake. Here, we present a high resolution 2D seismic tomographic image derived from an amphibious seismic profile located above the area of maximum co-seismic slip of the 2010 Maule earthquake (*Delouis et al.*, 2010, *Moreno et al.*, 2010, *Tong et al.*, 2010). The derived velocity model and aftershocks distribution is used to study the nature of the updip limit and the structure of the Maule earthquake rupture area. The main aim of this paper is examine the interplay between the aseismic-seismic and the accretionary prism-continental framework transition zones for the case of the Maule megathrust earthquake ( $M_w = 8.8$ ).

### 3.3 Tectonic setting

Along the central Chilean margin the oceanic Nazca plate subducts at a convergence rate of approximately 6.6 cm/yr beneath the South-American plate, with a convergence azimuth of  $\sim 78^\circ E$  (*Angermann et al.*, 1999). The southern central Chile trench ( $33^\circ S - 46.5^\circ S$ ) is filled by terrigenous sediments sourced from the Andes (*Thornburg and Kulm*, 1987), rising to a thickness of 2-3 km at the trench axis (e.g., *Scherwath et al.*, 2009). Trench sediments are redistributed from south to north due to the slight northward dip of the trench floor (e.g., *Thornburg et al.*, 1990).

Our study area is located between the Juan Fernández Hotspot Ridge and the oceanic Mocha Fracture Zone which is approximately coincident with the aftershocks of the Maule megathrust earthquake (figure 3.1). Here, the 30-38 Myr old Nazca plate (*Müller et al.*, 1997) presents a prominent outer rise seaward of a narrow trench basin where the uplifted oceanic basement is covered by a few hundred meters of pelagic sediments (*Contreras-Reyes and Osses*, 2010). Reduced values of  $V_p$  in the oceanic crust and in the upper mantle beneath the trench-outer rise zone have been imaged by seismic data (*Contreras-Reyes et al.*, 2008a), which may reflect normal faulting which creates pathways for hydration of the oceanic plate and upper mantle, producing upper mantle serpentinization (e.g.,

---

*Contreras-Reyes et al., 2008a, Ivandic et al., 2008).*

From the seismologic point of view, the central Chile subduction zone is one of the most active regions worldwide. The largest earthquake ever measured with a magnitude of  $M_w = 9.5$ , ruptured about 1000 km from Arauco peninsula (which is also the southern limit of the 2010 Maule earthquake rupture zone) in the north to the Chile triple junction in the south (*Cifuentes and Silver, 1989, Barrientos and Ward, 1990*). The rupture of the 2010 Maule Earthquake coincides with the seismic gap along the 1835 earthquake rupture zone, where two large earthquakes hit during the last century on 1928 ( $M_s = 8.0$ ) and on 1939 ( $M_s = 7.8$ ). These earthquakes were initially assumed to be interplate, but it has been shown that the 1939 earthquake was not a thrust earthquake, but a large intraplate event (*Campos and Kausel, 1990, Beck et al., 1998*). Therefore, stress accumulated in the interplate boundary between  $35^\circ S$  to  $37^\circ S$  for almost 175 years (*Campos et al., 2002, Ruegg et al., 2009*), and when the stress is finally released, slip occurred not only on the 1835 rupture area, but also along the interplate interface to the north that ruptured the 1928 and 1985 earthquakes, and along most of that zone ruptured during the 1906 earthquake (*Beck et al., 1998*).



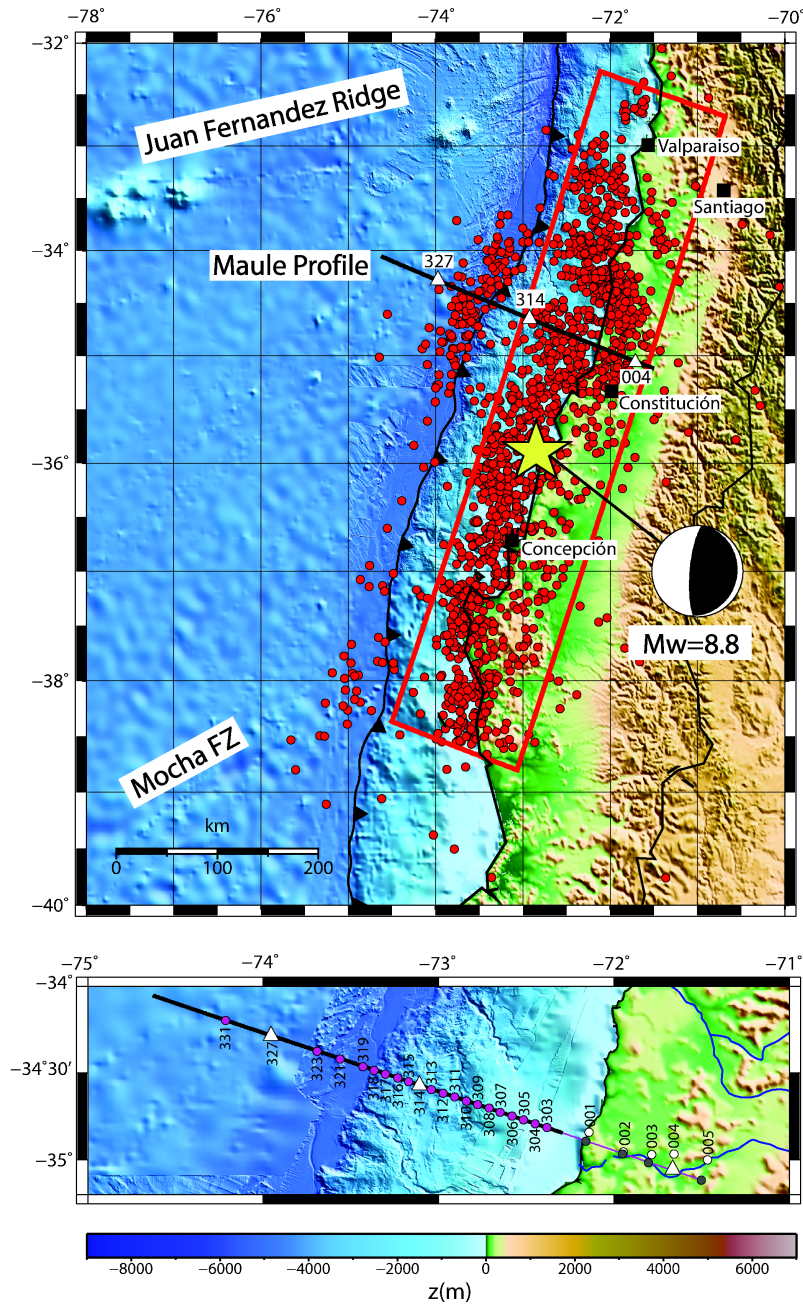


**Figure 3.1:** (Top) Map of the central Chile region. The red box outlines the rupture area estimated from the aftershocks of  $M_w > 4.0$  between 27th of February and 1st of August 2010, reported by NEIC catalogue. (Bottom) Stations location and shooting line of the profile (in black).

---

## 3.4 Seismic experiment and data

A combined onshore-offshore survey was carried out in central Chile at  $\sim 34.5^\circ S$ . The data were recorded in March 2008 during cruise JC23 of the British R/V James Cook. The resulting  $\sim 300$  km long profile is comprised 25 Ocean Bottom Seismometers/Ocean Bottom Hydrophones (OBS/OBH), and 5 short period land stations recorded the airgun shots fired from the vessel up to 80 km onshore. The seismic line covers the trench-outer rise, trench and fore-arc regions and continental crust. As seismic source we employed four tuned arrays of 3 airguns each plus two single airguns, providing a total volume of  $11200 \text{ inch}^3$ . Shots were fired every 60 sec. at a speed of 5 kn, yielding a shot spacing of  $\sim 150$  m. Preprocessing of the OBS/OBH data included calculation of the clock-drift corrections to adjust the clock in each instrument to the GPS base time, and instrument locations to corrected for drift from the deployment position during their descent to the seafloor using the direct water wave arrival. A time-gated deconvolution was applied to remove predictable bubble reverberations. Finally, for all the record sections, a time and offset-variable Butterworth filter, in which the pass-band moves towards lower frequencies as record time and offset increase, was applied to account for frequency changes caused by signal attenuation.

Figure 3.2 shows three representative examples of record sections from seismic stations located on the trench outer-rise, on the accretionary prism and on the continent. We recorded refractions from the sediments (Ps), crustal refractions (Pg), reflections from the top of the oceanic crust (PtocP), wide-angle Mohorovicic discontinuity (Moho) reflections (PmP), and mantle refractions (Pn) with excellent data quality, which enabled us to determine the structure of the continental wedge, oceanic crust, and upper mantle in detail. At some forearc stations, we also detected reflections from the bottom of the unconsolidated sediments (PsP). In the continental crust, we detected a mid-crustal reflector (PrP) on the easternmost land stations, indicating a strong velocity contrast between upper and lower continental crust beneath the coastal mountains.

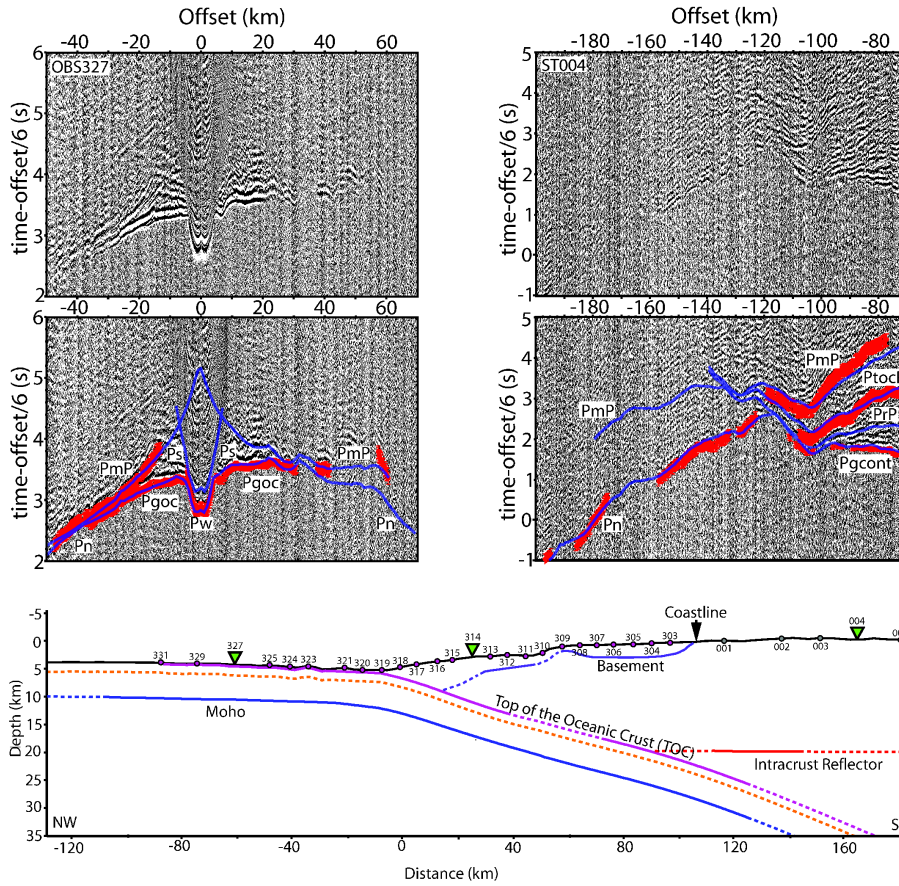


**Figure 3.2:** (Top) Record sections of OBS 327 (left) and OBH 004 (right). Time axis is reduced by 6 km/s. (Center) Record sections with superimposed travel times. (Bottom) Situation of the seismic stations on the bathymetry used for the modeling and seismic reflectors modeled. Data example stations are represented by green triangles.

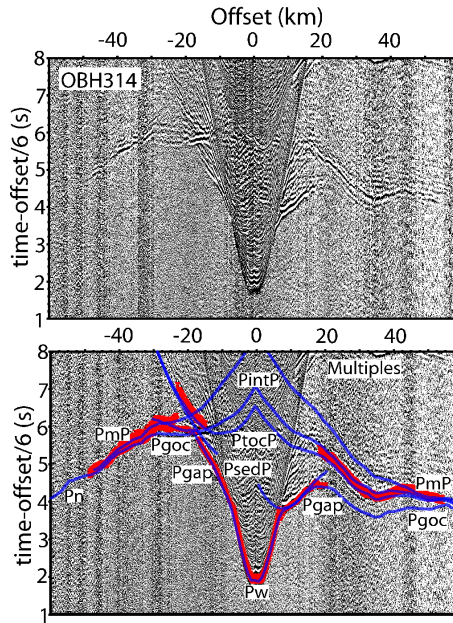


**Figure 3.3:** Record sections of OBH 314, located in the trench outer rise area.

### 3.5 Tomographic inversion scheme

The seismic velocity distribution was modeled by joint refraction/reflection 2D tomographic inversion using the program TOMO2D (Korenaga *et al.*, 2000). Our starting model is a simple layered structure including the following units (1) water, (2) sediments and accretionary wedge, (3) oceanic crust and (4) upper oceanic mantle. The size of the grid employed is 310 km long and 40 km deep, with a horizontal spacing of 500 m. In order to mimic the decreasing resolution at increasing depths, we parameterized the vertical spacing increasing with depth from 100 m just beneath the seafloor to 300 m at 40 km depth. The correlation length parameters were chosen to be 0.5 km x 0.1 km (horizontal x vertical) at the top and linearly increasing with depth to 3 km x 3 km at 40 km depth. Several tests have shown that varying the values of correlation lengths by 50% does not significantly affect the main features of the model (Korenaga *et al.*, 2000). Because of the trade-off between correlation lengths and smoothing weights, we used correlation lengths as short as possible and controlled the stability of the inversion by using large smoothing weights in order to reduce computational memory requirements (Korenaga *et al.*, 2000). The layer interface geometry is represented by a floating reflector which consists of an independent array of linear segments with a horizontal spacing of 500 m and only one

degree of freedom in the vertical direction. Depth and velocity nodes are equally weighted in the refraction and reflection travel time inversions.

The data set used for the travel time inversion is comprised by  $\sim 11000$  first arrivals (Ps+Pg and Pn),  $\sim 2500$  PtocP and  $\sim 5000$  PmP phases which were identified and hand-picked from a total of 30 instruments. The pick uncertainty was assumed to be half of the period of one arrival and were weighted according to the phase quality in order to account for systematic shift in the phase identification. Thus, the error assigned for the picks was 50 ms for Ps, 70 ms for Pg and 120 ms for PtocP, PmP and Pn phases.

In the first iteration only picks with offsets smaller than 15 km were inverted. In the following iterations, we increased this offset threshold in steps of 20 km, 30 km, 50 km, and all the picks, subsequently. This stepwise increment in the maximum offset ensures that the shallow part of the model is inverted before the deeper. This approach is necessary mainly for two reasons: (1) The ray coverage of the deeper parts is less dense and (2) The calculated travel times for deeply penetrating rays are also influenced by the shallower part of the model. We generalized this inversion methodology for the whole model by taking a top-to-bottom approach that consists of inverting the shallowest layer, and then fixing the upper section of the model with a weight of 1000 compared to the deeper sections. Then, we ran the joint inversion for the velocity and reflector geometry for the next depth layer. The stopping criteria of the inversion for each offset step was whether when the the number of iterations reached four or the residual error of the travel times (time observed minus time calculated) reached a value equal to or smaller than the error assigned to the picks, i.e.  $\chi^2 \leq 1$ , where  $\chi^2$  is the normalized sum of the RMS misfits divided by the corresponding picking uncertainties; a value of 1 means that the model error is equal to the data uncertainty. However, PrP was best seen on the two most eastward stations. We included the phase after inverting for the Pg and constrained the depth to the intracrustal reflector by a grid search, assuming a horizontal layering of the boundary. This is a reasonable approximation as the phase was only observed over a lateral distance of  $\sim 40$  km. The velocity contrast across the layer was approximated by using constraints from the Zoeppritz equations, indicating a velocity contrast of 0.5-0.6 km/s. In addition, using the Snell's law with velocities of 6.2 km/s and 6.7 km/s and a reflector at 20 Km depth, we estimate a critical distance of  $\sim 97$  km. The critical distance obtained, roughly coincides with the offset at which we can distinguish clear post critical PrP reflections in the data (see Figure 3.2). Subsequently, we fixed the layered structure obtained and repeated the previous step for the following deeper layer. Finally, we kept the entire crustal



---

structure fixed and inverted for the velocity in the upper mantle through the Pn refractions.

## 3.6 Resolution of the velocity model

To check the accuracy of the final model, we computed synthetic travel times for the first arrivals and reflected phases. To compare the seismic sections and the synthetic travel times, we superimposed the calculated travel times on the data. Figure 3.2 shows that the travel times predicted by our tomographic velocity model are in good agreement with the data recorded: all the first arrivals and the post-critical reflections calculated match the observed arrivals; however, pre-critical reflections are not clearly identified in most of the record sections.

In order to evaluate the capability of our velocity model to resolve spatial and amplitude variations, which are dependent on the given ray geometry and the velocity distribution, and also to evaluate the non linear sensitivity of the inversion, we computed checkerboard tests using a pattern of alternate positive and negative velocity anomalies of small amplitudes, compared to the final model. The final inverted velocity model is perturbed by the checkerboard pattern, yielding a known artificial model with the same source-receiver geometry as the original data. Synthetic travel times were computed through the perturbed model, and subsequently we performed a tomographic inversion based on these travel times, using the unperturbed velocity model as the initial model, in order to recover the initial perturbation pattern. To compute this test, we used Gaussian anomalies of amplitude  $\pm 5\%$  with four different sizes a) 2.5 X 2.5 km; b) 10 X 5 km; c) 20 X 10 km; d) 40 X 20 km (horizontal by vertical extent). The results of the test, presented in Figure 3.4, show that for the smallest perturbations, the full recovery of shape and amplitude of the anomalies is restricted to the sedimentary layer. For the case of the anomaly pattern b) we recovered the structure in the sediments, oceanic crust and accretionary wedge, but poor recovery for depths greater than 15 km and for the onshore part of the model. A similar behavior is observed for larger size anomalies c) and d), but with higher recovery in the lower oceanic crust and upper mantle than for the cases a) and b). Based on the checkerboard tests, we conclude that our model is highly reliable between distances of -100 km and 100 km from the deformation front and depths up to 15 km. On the other hand, it is likely that the velocity values tend to be over- or under- estimated in the order by 2-3% of  $V_p$  in the upper continental crust. We also concluded from this

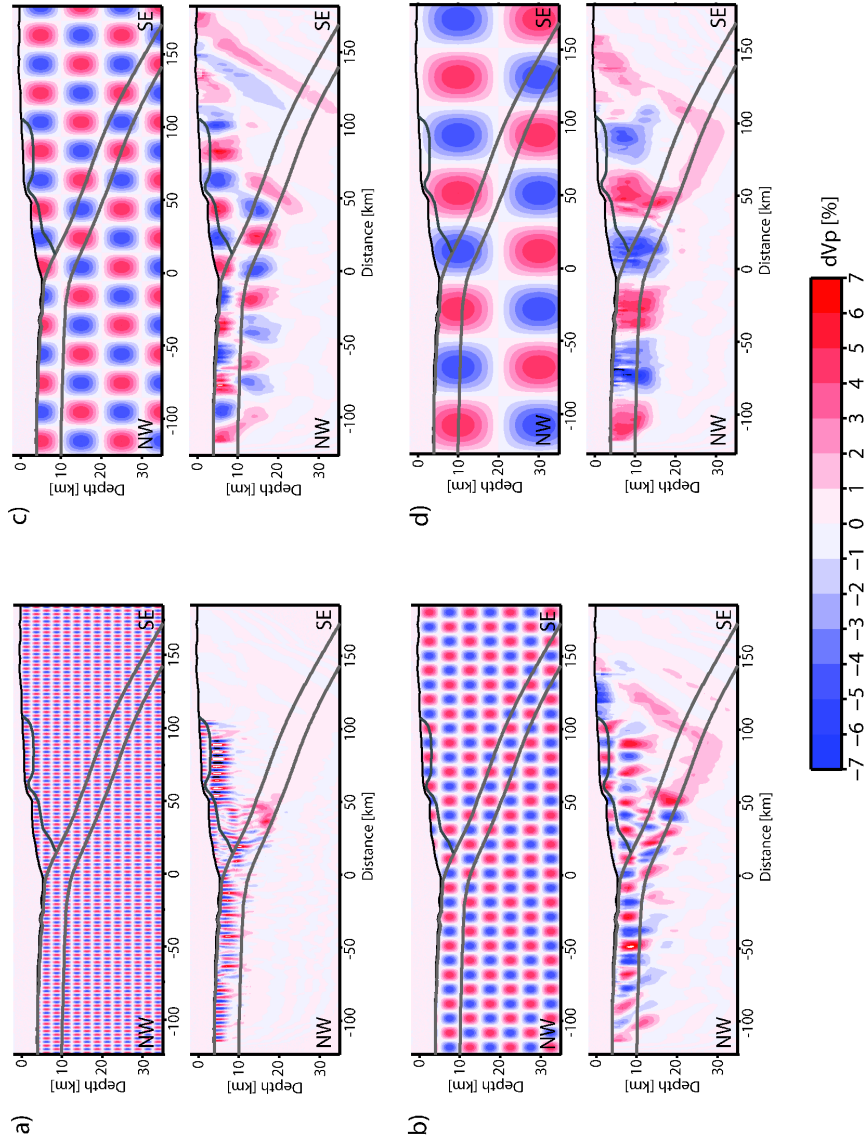


**Figure 3.4:** Results of the checkerboard tests. For each sub-plot: the top Figure shows the synthetic resolution pattern, and the bottom the recovery. The sizes of the anomalies are (horizontal by vertical extent) a) 2.5 X 2.5 km; b) 10 X 5 km; c) 20 X 10 km; d) 40 X 20 km

---

test that the velocities for the lower continental crust and the deep oceanic crust have low resolution for small features. The seismic ray distribution in our model is represented by the Derivative Weight Sum (DWS) shown in Figure 3.6c, which mathematically corresponds to the vector sum of the velocity kernel. This parameter provides crude information on the linear sensitivity of the inversion, describing the relative ray density near a given velocity node (*Toomey and Foulger, 1989*). Hence the resolution breaks down in the areas of low ray density, represented by low DWS values, while the recovery is high in the areas of high DWS values (Figure 3.6c).

### 3.7 Results

The seismic structure along the profile is presented in Figures 3.5 and 3.6b. The incoming oceanic crust seaward of the deformation front (defined as the origin for the horizontal coordinate) is characterized by a uniform thickness of approximately 6 km and velocities ranging between 4.5 km/s to 7.1 km/s for the upper and lowermost crust, respectively. These velocities are typical for a mature Pacific oceanic crust far from the spreading center (*Grevenmeyer et al., 1998*). Approaching the trench, however, the crustal velocities decrease, likely due to normal faulting produced by plate bending (e.g., *Contreras-Reyes et al., 2008a, Ivandic et al., 2008*). Well developed outer-rise faults observed in our high resolution bathymetric data (Figures 3.1 and 3.6) are coincident with the outer-rise seismicity (Figure 3.1). The upper oceanic mantle velocities range from 7.5-7.8 km/s beneath the trench axis to 8.2 km/s beneath the continental slope, perhaps indicating that the upper mantle is serpentinized. In fact, this finding is concordant with previous seismic works carried out in south central Chile (*Contreras-Reyes et al., 2008a, ?, Scherwath et al., 2009*) and suggests that the serpentinization of the oceanic mantle beneath the trench outer rise is a common process along the Chilean margin (*Contreras-Reyes and Osses, 2010*).

In the overriding plate, the tomographic model reveals two prominent velocity transition zones characterized by steep lateral velocity gradients, resulting in a seismic segmentation of the marine forearc. The margin is composed of three clear domains: (1) the toe of the continental slope, a wedge shaped body with typical velocities of sediments ( $\approx 4.0$  km/s) that we interpret as the frontal accretionary prism (FAP). This shaped body extends from the deformation front up to the shelf break, where domain (2) begins and extends to the coast where velocities range between 4.0 km/s and 5.5 km/s, indicating a



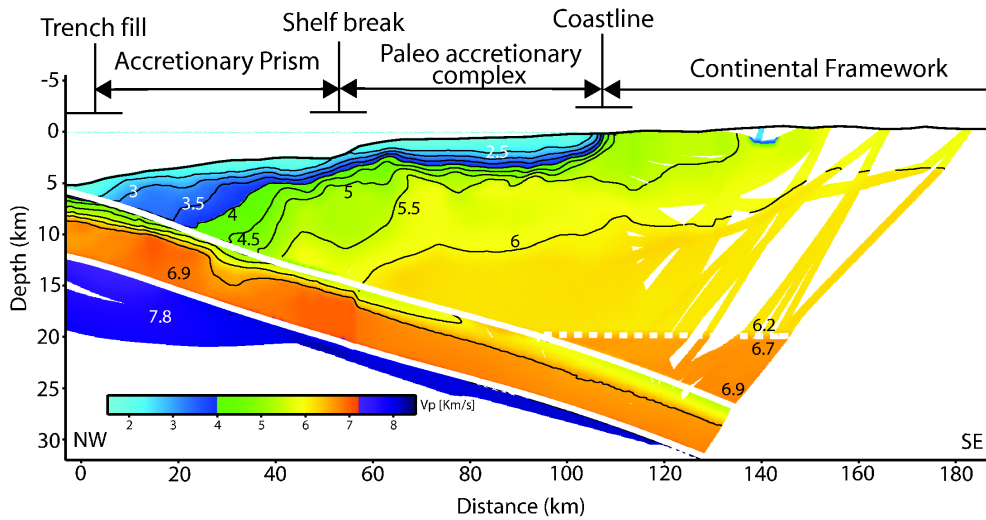


**Figure 3.5:** *Traveltime tomography of the forearc offshore Maule and its seismic interpretation based on the comparison of our results with the structure of the margin offshore Arauco (Contreras-Reyes et al., 2008a)*

lower effect of fracturing and a higher mechanical resistance in comparison with the FAP. The transition between zones (1) and (2) is characterized by a strong horizontal velocity gradient between 40 km and 60 km landward from the deformation front. This domain has been already interpreted as a paleo accretionary prism with an estimated Jurassic age (Contreras-Reyes et al., 2008a). We also identify on the shallow part of this domain typical sediment velocities, layered vertically and increasing from 2.5 on top to 4 km/s at the bottom, corresponding to the Mataquito basin. This forearc basin is filled by more than 3000 m of marine clastic sediments that were deposited during the last  $\sim 100$  My (González, 1989). The transition to domain (3) is signaled by another sharp velocity gradient further landward where  $V_p$  increases from the continental shelf to values of 5.0-5.5 km/s near onshore. This change in velocity marks the transition of the paleo accretionary prism to the late Paleozoic arc granitoids that are associated with low P/T metasediment (“Eastern Series”) exposed in the Coastal Cordillera (Arriagada et al., in press).

The Top of the Oceanic Crust (TOC) dips from  $\sim 6$  km beneath the deformation front with an angle of  $4^\circ - 6^\circ$  and becomes steeper under the shelf, dipping at  $\sim 10^\circ$  and reaching some 22 km under the coast line. The maximum depth to the top of the oceanic crust indicated by our data is about 27 km, and occurs approximately 20 km landward of the coastline.

---

## 3.8 Discussion and conclusions

### 3.8.1 Relationship between the updip and the backstop.

The abrupt horizontal velocity gradient detected between  $\sim 40 - 60$  km landward of the deformation front (Figure 3.5) is interpreted as a transition between accreted sediments to the paleo accretionary complex (backstop). The backstop is defined as a region within the forearc that is significantly stronger than the accreted sediment lying further trenchward (Byrne *et al.*, 1988). In addition, the backstop may control the seismic front, a transition zone between stable and stick-slip frictional sliding along the plate boundary. Thus, the seismic front may be related to the maximum depth of the unconsolidated FAP sediments, which marks the deep end of the aseismic zone and hence the updip of the seismogenic zone (Byrne *et al.*, 1988). Therefore, seismic energy may dissipate as anelastic deformation through the accretionary prism and/or as stable aseismical sliding (Scholz, 2002). This stable sliding between the plates is probably facilitated by the presence of overpressured and unconsolidated sediments at the plate boundary, and therefore it is characterized by the absence of both strong and weak thrust earthquakes (Byrne *et al.*, 1988).

Figure 3.1 shows the USGS aftershock distribution along the rupture area of the mega-thrust Maule earthquake (<http://neic.usgs.gov>) where most of the interplate events concentrate. It is interesting to note that the aftershock distribution of the Maule earthquake displays a clearly defined aftershock front at a roughly constant distance from the deformation front of 30-50 km. Furthermore, the seaward limit of the aftershocks is coincident with the location of the imaged seismic backstop (Figure 3.5). On Figure 3.6a we show a frequency histogram based on the projection of more than 1000 aftershocks on our profile. It presents three clear areas: (1) the trench outer-rise region where seismic activity concentrates less than 10% of the observed seismicity, (2) a seismically inactive region, beneath the FAP, and (3) the seismogenic zone, which begins at the backstop. This finding suggests that the frontal accretionary prism indeed behaves as an aseismic region and the backstop defines the updip limit of the seismogenic zone. Published 2D seismic velocity models in the northern and southern limit of the Maule rupture area show a FAP with a similar size  $\sim 30$  km wide (Zelt *et al.*, 2003, Contreras-Reyes *et al.*, 2008a, respectively). The distance of the backstop offshore Maule at 40-60 km

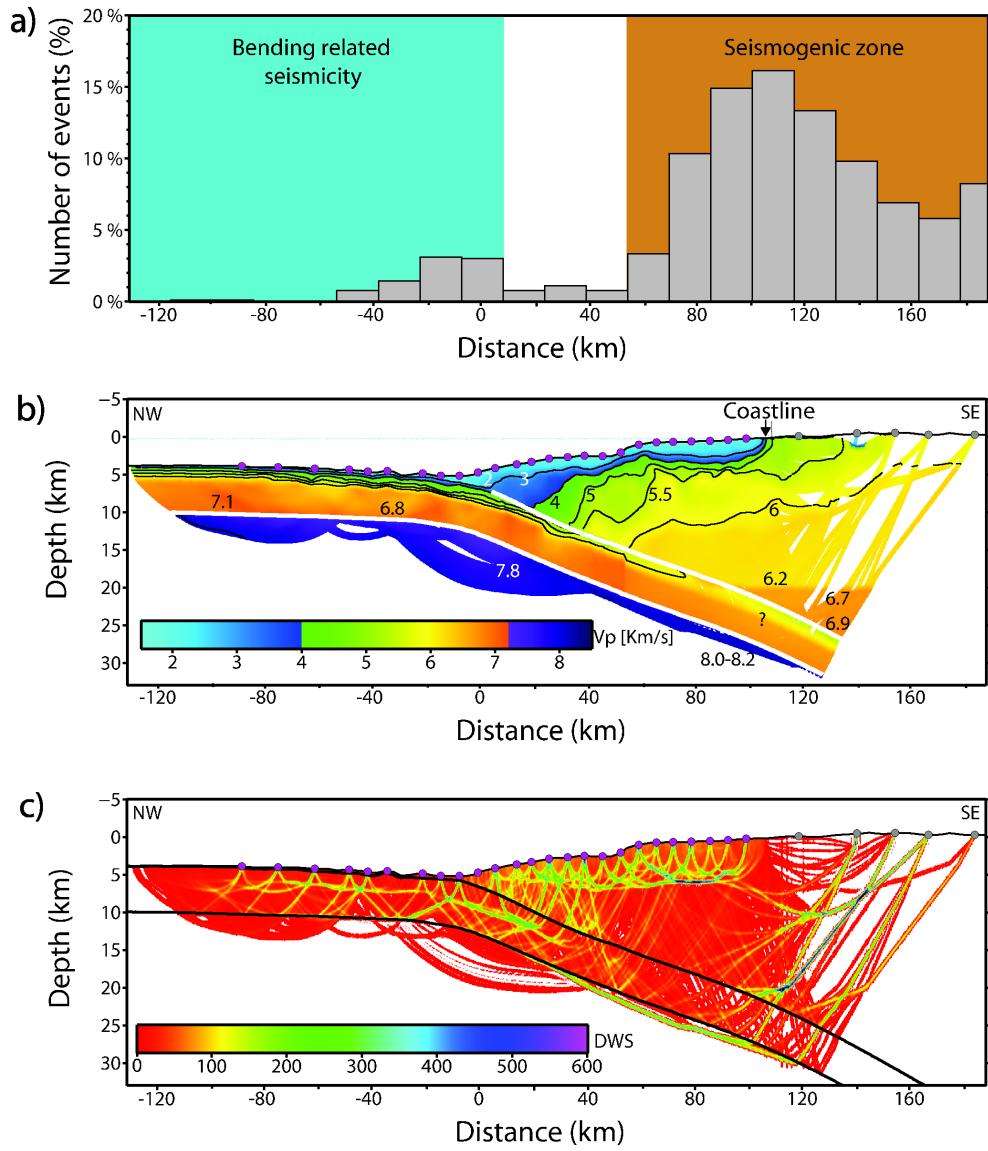


**Figure 3.6:** a) Frequency histogram of the aftershocks projected on the profile; b) Travel-time tomography of the profile masked by the seismic ray paths. The overall residual time of the model is 0.103 ms ( $\chi^2 = 1.1$ ); c) Derivative weight sum (DWS).

---

from the deformation front, is also concordant with the location of the backstop imaged by *Diaz-Naveas* (1999) and *Grevenmeyer et al.* (2003), analyzing multi-channel seismic reflection data between  $35^{\circ}S - 40^{\circ}S$ . Therefore, the structure of the marine fore-arc may control the seaward limit of co-seismic rupture in south-central Chile (*Contreras-Reyes et al.*, 2010). However, the backstop roughly coincides with the location of the thermally defined up-dip limit proposed by heat flow surveys (*Grevenmeyer et al.*, 2003). Therefore, both the occurrence of a water-rich and highly unconsolidated accretionary prism and a temperature of  $100^{\circ}C$  to  $150^{\circ}C$  in the subduction thrust may establish the seaward limit of the seismogenic coupling zone.

The strong spatial correlation between coseismic activity, backstop, location of the continental shelf and position of the  $100 - 150^{\circ}C$  isotherm in the interplate contact has also been observed and analyzed in other well studied subduction zones such as south Alaska, Cascadia (*Oleskevich et al.*, 1999) , Japan (*Obana et al.*, 2003, *Nakanishi et al.*, 2004, *Oleskevich et al.*, 1999) and Sumatra (*Klingelhoefer et al.*, 2010). This suggests not only that these features are interrelated, but also that it is common in subduction zones capable of producing large earthquakes.

### **3.8.2 Maule earthquake nucleation zone**

The plate interface is well constrained by refractions and reflections down to a depth of  $\sim 15$  km. At greater depth the geometry of the interface is entirely based on wide-angle reflections from the top (P<sub>top</sub>P) and bottom (P<sub>bot</sub>P) of the subducting plate, recorded at the land stations. If we assume that the epicenter location published by the USGS for the main shock of 27th february 2010 is correct, then the projection of this location on our derived interplate boundary gives a depth of  $\sim 20$  km near the coast (see Figure 3.7).

If we examine the maximum depth of seismic coupling and compare it with the hypocenters of thrust earthquakes, this suggests that large interplate earthquakes ( $M > 6$ ) nucleate preferentially far downdip from the trench axis at a depth of about 50 km for the Chilean margin (*Tichelaar and Ruff*, 1991, 1993). A recent example of this is the 2007 Tocopilla earthquake ( $M_w = 7.7$ ) that ruptured the deeper part of the seismogenic interface, between 30 and 50 km depth (*Bejar-Pizarro et al.*, 2010, *Peyrat et al.*, 2010). Surprisingly, our estimation of the hypocenter shows that the Maule earthquake nucleated offshore and beneath the forearc basin, somewhere in the middle of the seismogenic zone, probably near

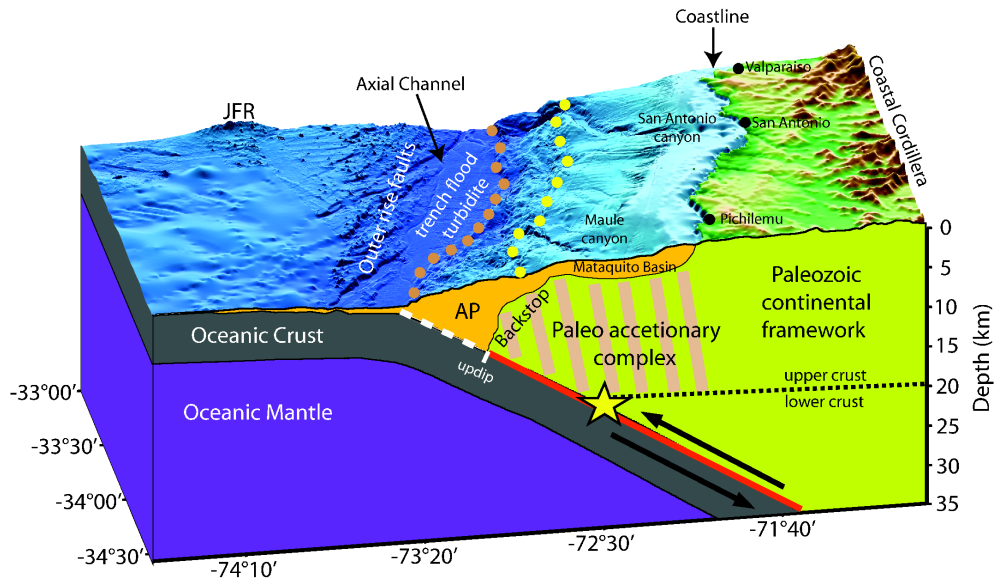


**Figure 3.7:** Geological interpretation of the study area. AP stands for accretionary prism. The red thick line corresponds to the estimated seismogenic zone, and the white segmented line to the aseismic zone. The orange dots on the bathymetric map indicate the deformation front and the yellow ones the projection of the backstop front.

the intersection between the incoming oceanic plate and the boundary between upper and lower continental crust, as is shown in Figure 3.7. The hypocenter is clearly shallower than the expected downdip limit of seismic coupling defined by the intersection of the plate boundary with the continental Moho at  $\sim 35 - 40$  km depth (Heit *et al.*, 2008, Lloyd *et al.*, 2010, Haberland *et al.*, 2009, Tong *et al.*, 2010) and the seismic coupling depth derived from GPS data, occurring at 50 km (Ruegg *et al.*, 2009).

---

# Chapter 4

## Outer rise seismic structure

### 4.1 Introduction

The amount of water stored within the oceanic lithosphere plays a fundamental role in the generation of arc and back-arc magmas, hydration of the mantle wedge, and the global circulation of water (*Hacker, 2008*). The south central Chile subduction zone is characterized by a highly fractured trench outer-rise seafloor, which is generated by the bending of Nazca plate (*Contreras-Reyes and Osses, 2010*, and references therein). These bending-related faulting may reactivate pre-existing cracks in the oceanic crust, previously created at the spreading center, which may also generate faults cutting deep into the lithosphere (e.g., *Grevenmeyer et al., 2005*). This process modifies the porosity and permeability structure of the oceanic crust (*Carlson, 2010*) and allows the water to infiltrate deep into the lithosphere, producing hydration of the crust and eventually serpentinization of the upper mantle (e.g., *Contreras-Reyes et al., 2008a,b, Ranero et al., 2005*). Another proposed pathway for fluids through the crust are seamounts and outcrops penetrating through the sediments (e.g., *Fisher et al., 2003, Contreras-Reyes et al., 2007*).

The creation of normal faults in the outer rise, due to plate bending, is responsible for the shallow intraplate seismic activity (e.g., *Ranero et al., 2005*) that might produce considerable seismicity seaward the updip of the seismogenic zone (*Moscoso et al., 2011*) and may also in rare cases produce devastating tsunamis (*Satake and Tanioka, 1999*).

---

Although the magnitude of the offshore intraplate events is in general smaller than the subduction-related earthquakes, they can present considerable magnitudes. As a matter of fact, the largest normal-faulting event ever reported is the Sanriku, Japan earthquake of 1933, with a magnitude  $M_w=8.5$ , that probably ruptured along the entire oceanic lithosphere (Kanamori, 1971).

Previous seismic studies made offshore south-central Chile show evidence of hydration of the oceanic crust and serpentinization of the upper mantle at the Juan Fernández ridge (Kopp *et al.*, 2004), in the trench-outer rise area offshore Arauco (Contreras-Reyes *et al.*, 2008a) and offshore the zone comprised between Chiloé and the Chile Triple Junction (Contreras-Reyes *et al.*, 2008b); lithospheric hydration has also been observed by seismic studies performed in erosive margins offshore Northern Chile (Sallarès and Ranero, 2005) and Nicaragua (Ivandić *et al.*, 2008). Seismological studies suggest that hydration of the oceanic plate and outer rise seismicity are not independent phenomena (Ranero *et al.*, 2005, Tilmann *et al.*, 2008) and they are probably common processes along subduction zones (Contreras-Reyes and Osses, 2010, Grevenmeyer *et al.*, 2007).

A parameter commonly used to evaluate the hydration is the elastic parameter Poisson's ratio ( $\nu$ ). It is defined as the ratio, when a sample object is stretched, of the contraction or transverse strain (perpendicular to the applied load), to the extension or axial strain (in the direction of the applied load). Its analytical formula expressed in terms of body waves is given by the expression 4.1:

$$\nu = \frac{(V_p/V_s)^2 - 2}{2(V_p/V_s)^2 - 2} \quad (4.1)$$

and its standard deviation  $\Delta\nu$  is calculated by 4.2:

$$\Delta\nu = \frac{(V_p/V_s)^2}{2(V_p/V_s)^2 - 2} \sqrt{\left[\frac{\Delta V_p}{V_p}\right]^2 + \left[\frac{\Delta V_s}{V_s}\right]^2} \quad (4.2)$$

Where  $\Delta V_p$  and  $\Delta V_s$  are the standard deviations of P- and S-wave velocity fields, respectively. Poisson's ratio is very sensitive to the existence of water. In a material with high content of water,  $V_s$  tends to decrease faster than  $V_p$ , producing an increment of  $\nu$ .

To study the hydration-seismicity relationship offshore Maule, we analyzed jointly



(1) seismological data from a temporal outer rise seismic network (ORN) deployed for about 1 month, (2) swath bathymetric data, and (3) the seismic velocity structure of the Nazca plate prior to its subduction between  $\sim 34^\circ S$  and  $\sim 35^\circ S$ . Wide-angle seismic data from a trench parallel seismic profile 85 km long, was used to derive seismic models of the compressional ( $V_p$ ) and shear wave ( $V_s$ ) velocity distribution. We employ traveltime tomography of the velocity structure and crustal thickness to obtain accurate 2-D velocity models and hence Poisson's ratio distribution. P- and S- wave model uncertainties are estimated by applying a non linear Monte Carlo-like method (*Korenaga et al.*, 2000). We examine the crustal models to derive an estimation of the hydro-alteration degree of the upper lithosphere and subsequently we discuss the implications of variations of the oceanic upper mantle velocity, comparing our results with published data from a seismic profile which runs perpendicular to the current profile (*Moscoso et al.*, 2011).

## 4.2 Tectonic framework

The oceanic Nazca plate converges beneath the South American plate at relative velocity of  $6.6\text{cm/yr}$  with an azimuth of  $78^\circ E$  (*Angermann et al.*, 1999). The Nazca plate oceanic crust offshore central Chile between  $32^\circ S$  and  $38^\circ S$ , has been generated at the Chile-rise  $\sim 30$  to  $\sim 35$  MY ago (*Müller et al.*, 1997), which spreading center segments and bending related normal faults can be observed in the high resolution bathymetric map of Figure 4.1. The seabed is covered by a sedimentary layer of  $\sim 200$  meters on the location of our profile with increasing depth trenchward to a maximum of  $\sim 2$  at the trench axis (*Moscoso et al.*, 2011). The incoming plate in the trench-outer rise area is highly faulted and hydrated by intrusions of cold seawater (*Grevemeyer et al.*, 2005). These faults are able not only to hydrate the crust and but even the upper mantle (e.g., *Contreras-Reyes et al.*, 2008b). The Juan Fernandez Ridge (JFR) at  $\sim 32^\circ S$  acts as a barrier for the migration of sediments sourced from the Andes (*Blumberg et al.*, 2008) and carried in the trench from south to north, which changes the regimen of the margin from north erosive to south accretionary (*von Huene et al.*, 1997).

From the seismological point of view, the central Chilean margin has hosted some of the largest earthquakes of the Earth. A few times in every century, large thrust earthquakes break several hundreds of kilometers in a single shock (e.g., *Barrientos*, 2005), producing in most of the cases devastating tsunamis (*Cisternas et al.*, 2005). Previously, the thrust

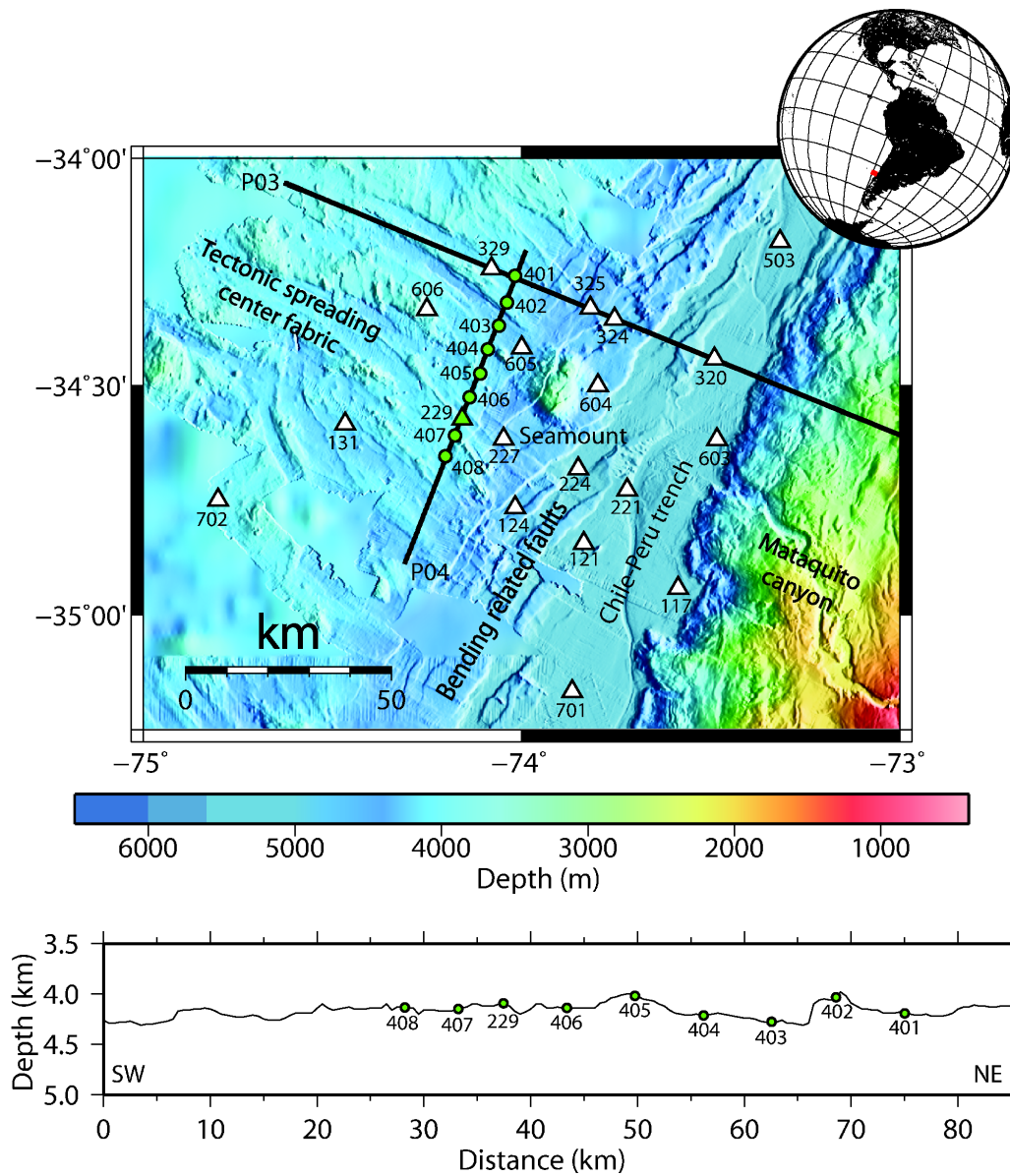


**Figure 4.1:** (Top) High resolution bathymetric map offshore Maule region. The solid lines represent the transects P03 and P04, the green dots show the stations locations for the wide-angle experiment and the white triangles represent the position of the local seismic network. Station 229, represented by a green triangle, was used for both experiments. At the bottom the OBS/OBH locations are plotted on the bathymetry.

offshore Maule has been reported as fully locked (*Ruegg et al.*, 2009, *Campos et al.*, 2002). In fact, the last 2010 megathrust Maule earthquake ( $M_w=8.8$ ) ruptured about 400 km along the margin, producing a devastating Tsunami (*Madariaga et al.*, 2010). The second largest slip of the 2010 Maule earthquake was reported between  $34^\circ$  and  $35^\circ$  (*Delouis et al.*, 2010, *Moreno et al.*, 2010). This zone coincides with an anomalous high outer-rise seismic activity after the earthquake in comparison to the rest of the Maule seismic segment (*Moscoso et al.*, 2011).

## 4.3 Seismic experiment and data

The data analyzed in this study, consists of high resolution multibeam bathymetry, wide-angle seismics and local earthquake measurements made offshore the Maule region ( $34^\circ S - 35^\circ 30' S$ ), during March and April 2008 during the cruise JC23 of the British RV James Cook (*Flueh and Bialas*, 2008).

### 4.3.1 Local earthquake data

The outer rise network (ORN), deployed between the 1<sup>st</sup> of March and the 8<sup>th</sup> of April 2008, consists of 19 Ocean Bottom Seismometers (OBS) (*Bialas and Flueh*, 1999) each of them also equipped with an Ocean Bottom Hydrophone (OBH) (*Flueh and Bialas*, 1996). The instruments were deployed with a spacing between 20 and 40 km, covering an area of approximately 100 by 100  $km^2$ . The network extended over the outer rise from  $\sim 200$  km offshore the deformation front, surrounding the Maule seamount as shown in Figure 4.1.

Preprocessing of the OBH/OBS data included calculation of the clock-drift corrections to adjust the clock in each instrument to the GPS base time. Instrument locations were corrected for drift from the deployment position during their descent to the seafloor using the direct water wave arrival, recorded from the active seismics. A short-term average versus long-term average (STA/LTA) trigger algorithm was applied to detect signal variations that could indicate an event. Earthquake identification from the triggered data was done manually, giving a total of 29 events, 7 of them were inside the network. The data reading and picking of the P and S arrivals was done using the software SEISAN (*Havskov and Ottemöller*, 1999). We picked the phases manually applying a quality factor,

Phase	Total Picks	Pick error min. (ms) *	Pick error max. (ms) †	Average final $T_{rms}$ (ms)	Average final $\chi^2$
Pg	2701	50	65	59.8	1.18
PmP	1850	50	65	60.5	0.95
Pn	543	50	65	67.7	1.09
Total	5094			60.9	1.11
Sg	984	75	85	74.3	0.87
SmS	235	75	85	97.1	1.61
Total	1219			78.0	0.98

**Table 4.1:** Summary of data picking information and statistics of the fitness between the final average models and picks

which accounts for the picking uncertainties.

### 4.3.2 Wide-angle seismic data

The wide-angle seismic profile P04 is a  $\sim 84$  km long transect that runs parallel to the trench in the outer rise area, 130 km offshore Constitución (See Figure 4.1). As seismic source we used four tuned arrays of three airguns each plus two single airguns, providing a total volume of  $11200 \text{ inch}^3$ . The airguns were fired at intervals of 60 s, resulting at ship's speed of 5 kn into an average of 150 m. The airgun shots were recorded by 8 OBS and 1 OBH, which makes a total of 9 stations deployed along the transect. A time-gated deconvolution filter was applied to remove predictable bubble reverberations.

P wave arrivals were recorded with excellent quality and clear S wave arrivals were recorded in 8 of the 9 seismic stations (only station 404 did not present distinguishable S waves arrivals). Data examples from two stations are shown in Figure 4.2, with their respective seismic phases identified. Picking of the seismic phases was done manually, and picking errors were assigned on the basis of the dominant period of the phase. Typically, errors were assumed to be half a period of one arrival and weighed according to the phase quality. Based on the quality of the data, for S wave arrivals we assigned a higher error than for the P phases and due to the larger uncertainties for larger offsets, we assigned differentiated picking uncertainties for long offset arrivals. Detailed information regarding

\*Picking error for arrivals with offset smaller than 20 km for P waves arrivals and 30 km for S waves arrivals

†Picking error for arrivals with offset larger than 20 km for P waves arrivals and 30 km for S waves arrivals

picks uncertainties and statistics of their fitness to the final model are summarized in Table 4.1.

## 4.4 Velocity field modeling procedure

### 4.4.1 P wave traveltimes tomography

The absence of refracted arrivals from the sedimentary layer and of reflections from the basement, was overcome assuming typical  $V_p=1.8$  km/s and  $V_s=0.25$  km/s for sediments and calculating the sediment thickness beneath each station through the time difference between the Pg and PPS phases, which ranges between 0.6 s and 1.1 s (see Figure 4.3b), yielding a 180-300 m sediment thickness.

The 2D  $V_p$ -depth distribution below the sedimentary layer was obtained using the joint refraction and reflection traveltimes inversion code TOMO2D, that simultaneously solves for the seismic velocity field and the depth of a floating reflecting interface (*Korenaga et al.*, 2000). Traveltimes and ray paths are calculated employing a hybrid ray tracing scheme, based on the graph method (e.g. *Dijkstra*, 1959) and in the local ray bending refinement (e.g. *van Avendonk et al.*, 1998). The grid used to represent the velocity field is parametrized as a sheared mesh hanging beneath the seafloor, where the node spacing was fixed constant in 0.5 km for the horizontal dimension and varying from 0.05 km at the top of the model to 0.5 km at the bottom for the vertical. The smaller spacing on top accounts the higher resolution in shallower parts of the model than at the bottom. The Moho is represented by a floating reflector, which consists of an array of linear segments with a horizontal equidistant spacing of 0.5 km between its nodes, and only one degree of freedom in the vertical direction.

The data set considered for the P wave tomography consists of 2701 Pg, 1067 PmP and 543 Pn phases that were handpicked on 9 seismic sections. The size of the model is 84 km long and 14 km depth. We performed the inversion using the "layer stripping" method: first the oceanic crust reflections (Pg) and wide angle moho reflections (PmP) were inverted and then the upper mantle refractions (Pn), keeping the model over the moho fixed. Tomographic inversion was undertaken using the technique of Hole (*Hole*, 1992) inverting in the first iterations only the picks with offsets smaller than 20 km. This threshold was

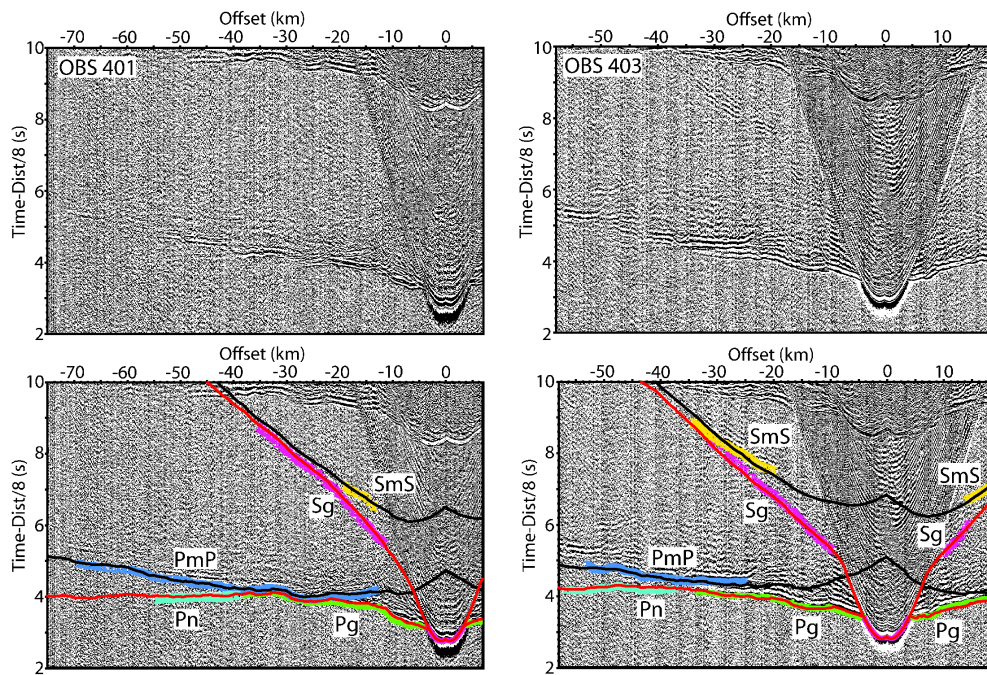


**Figure 4.2:** Examples of wide-angle seismic data recorded by the hydrophone (top) with manually picked arrivals and predicted traveltimes using the average 2D final models (center) and the correspondent rays (bottom), for a)  $V_p$  model and, b)  $V_s$  model.



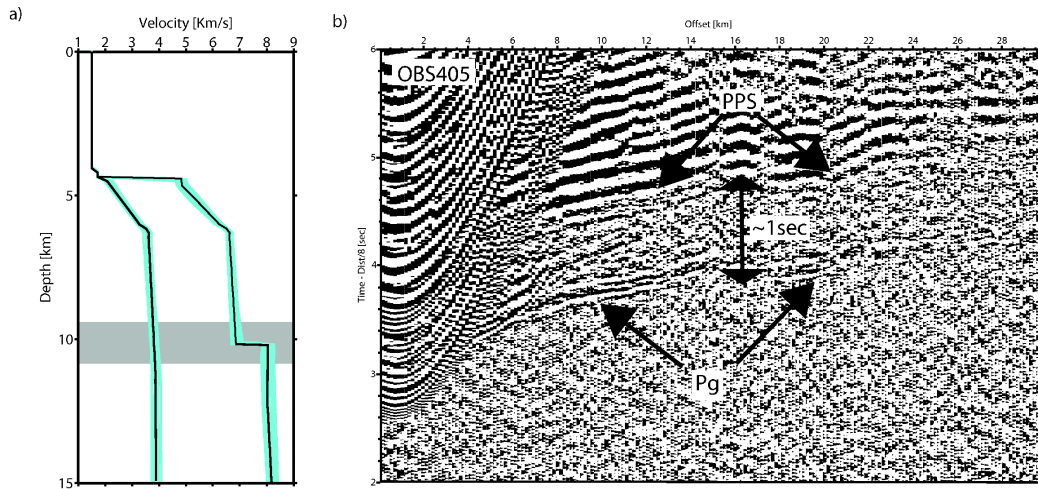


**Figure 4.3:** *a) Initial models used for the Monte Carlo inversion procedure for  $V_s$  (left) and  $V_p$  (right). The gray area shows the range of the initial Moho depth for the reflector's inversion b) Example of the delay between  $P_g$  and  $P_p$  phases recorded by the radial component of OBS 405.*

increased stepwise in steps of 10 km up to 90 km, ensuring that the shallow portion of the model is inverted before the deep portion. The described procedure is necessary because the ray coverage for the deeper parts is less dense and because the calculated travel times for deeply penetrating rays are also influenced by the upper portions of the model. The inversion is stabilized by using smoothness correlation lengths in the horizontal and vertical directions of the velocity mesh and for the depth nodes. The values used for the correlation lengths vary from 2 km to 10 km for the horizontal and from 0.1 km to 2 km for the vertical, at the top and bottom of the model respectively. Initially, the depth sensitivity parameter kernel  $\omega$  was set to 1, which means that velocity field and reflector nodes are equally weighted during the inversion. For each data set we run 4 iterations which were enough to obtain a good fit between observed and calculated arrivals (see Table 4.1). Picked and calculated travel times, and ray tracings for two ocean bottom instruments are shown in Figure 4.2.

#### 4.4.2 S wave traveltime tomography

Since airguns generate a purely compressional wavefield, the shear waves observed in the data are generated through mode conversion. The most plausible interface for generation of

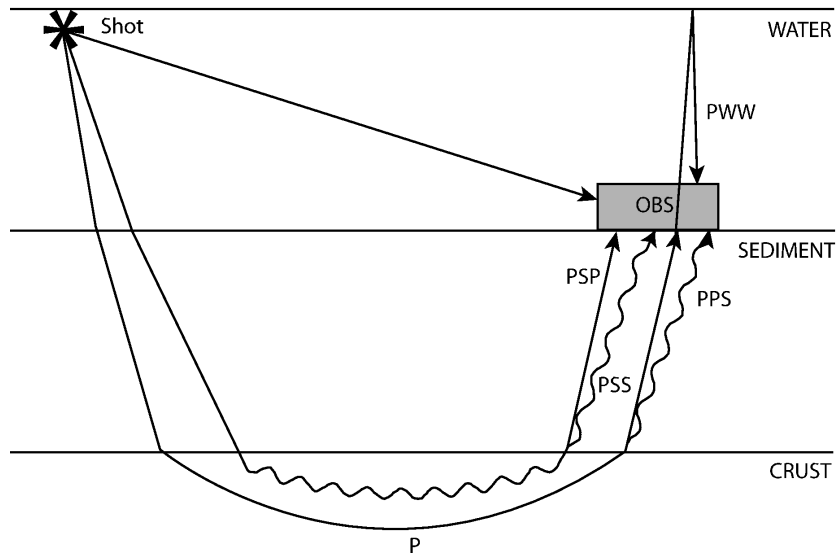


**Figure 4.4:** *Nomenclature for converted seismic phases, modified after Au and Clowes (1984).*

converted shear arrivals is the interface between the sedimentary layer and the crystalline basement (*Spudich and Orcutt, 1980*) whether when they are diving down (PSS), up (PPS) or both (PSP) (Figure 4.4). Under this assumption, recorded the PSP waves were inverted keeping the sediment/basement interface geometry, the Moho reflector and the velocity in the sediment fixed for the inversion of the S<sub>g</sub>, S<sub>n</sub> and S<sub>mS</sub> phases. In other words, the geometry is assumed from the V<sub>p</sub> tomography and only V<sub>s</sub> values are updated during the inversion. For this purpose the kernel weighting factor is set to  $\omega = 0.001$

## 4.5 Velocity model assessment

### 4.5.1 Model uncertainty

In order to estimate the sensitivity of our final model to different starting models and data, we applied a Monte Carlo-like approach by averaging the solutions of 100 realizations (*Korenaga et al., 2000*). The degree of dependence of the final solution on the starting model can be assessed by conducting a number of inversions with a variety of randomly generated initial models and initial data sets (*Tarantola, 1987*). To estimate the model



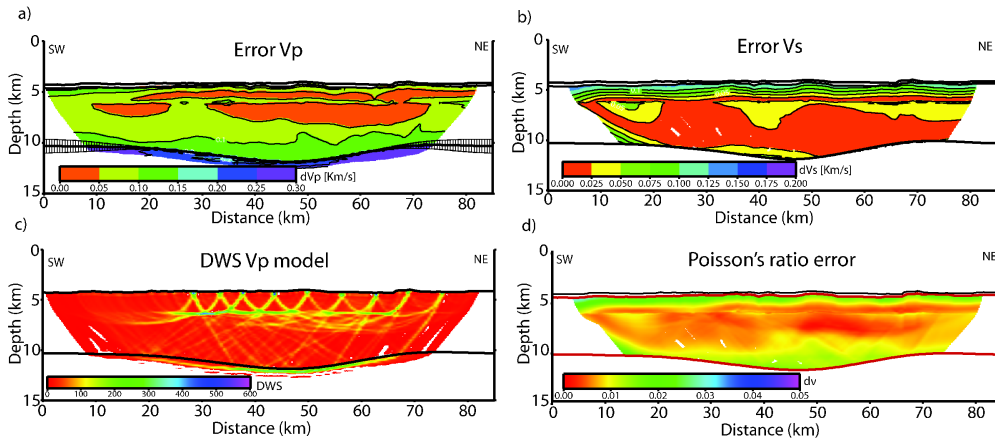


**Figure 4.5:** a) Error for the  $V_p$  model and Moho reflector; b) Error for the  $V_s$  model; c) DWS for  $V_p$  model; d) Poisson's ratio error derived from equation 4.2.

uncertainty, 10 initial models were derived from the 1D starting reference model by varying the velocity and the initial reflector  $\pm 10\%$  (Figure 4.3a). These models are in the vicinity of the possible solutions and also cover a wide range of seismic velocities found in Nazca platet, offshore central Chile (e.g. *Scherwath et al.*, 2009, *Contreras-Reyes et al.*, 2010). Consequently, each model was inverted with 10 noisy data sets in order to include the subjectivity of picking in our analysis. Regarding the Moho reflector, it reaches minimum error at the center of the profile and larger uncertainty at the extremes of the model. The results of this test for  $V_p$  and  $V_s$  are in Figures 4.5a and 4.5b, respectively and final  $Trms$  and  $\chi^2$  of the average final models are summarized in Table 4.1.

The seismic ray distribution in our model is represented by the derivative weight sum (DWS), which mathematically corresponds to the column vector sum of the velocity kernel. This parameter provides crude information on the linear sensitivity of the inversion describing the relative ray density near a given velocity node (*Toomey and Foulger*, 1989). The DWS value of Figures 4.5c shows excellent ray coverage in the upper crust and good ray coverage in the lower crust and upper mantle. Hence, zones of high and low resolution can be explained by high and low ray coverage respectively (see Figures 4.5a and 4.5c).

---

## 4.5.2 Resolution tests

In order to check the resolvability of the obtained velocity models and explore whether our data set can resolve anomalous crustal velocity zones, we have created synthetic models by using the final average velocity models for  $V_p$  and  $V_s$  and superimposing onto the oceanic crust five Gaussian velocity anomalies (Figure 4.6). The maximum amplitude of each anomaly is  $\pm 5\%$  of the velocity. In order to estimate how good is the recovery of the perturbations, synthetic traveltimes data with the same source-receiver geometry as in the real data set were inverted, using the final average velocity model as initial model. To qualify the robustness of the test, this procedure was repeated for a second set of perturbations with the same geometry and amplitudes of the initial set, but with opposite sign. The result shows that, for the given anomalies, the recovery of shape and amplitude is maximum between the 20 km and 60 km of distance, while at the extremes the models are still capable to discriminate between positive and negative anomalies and to estimate their amplitude and position. However the shape of the anomalies is not fully recovered. This is observed in both,  $V_p$  and  $V_s$  models. Thus, the resolving power of our data set is good enough to resolve features similar to the one found in the lower crust of the  $V_p$  model between 40 km and 60 km.

## 4.5.3 Velocity-Depth ambiguity

The  $V_p$  values for the lower crust and the Moho reflector, would not be univocally revealed due to the low amount of crossing ray paths on this zone (Figure 4.2). This effect is due to the geometry of the experiment, and can not be attributed to the inversion procedure (Tieman, 1994) and it produces a trade off between Moho depth and  $V_p$ , called velocity-depth ambiguity. This implies that our initial choice of  $\omega = 1$ , might drive to the calculation of an unconstrained model (Korenaga, 2011).

In order to evaluate the influence of the kernel weighting factor  $w$  into the final model calculation, we recomputed the velocity models in a similar way as described in the previous section, but using a  $\omega = 0.001$  for the  $V_p$  inversion with a starting flat Moho reflector at 10,5 km depth. For the  $V_s$  modelling, we used the same inversion procedure previously described.

The results obtained by applying this procedure are presented Figure 4.7, showing

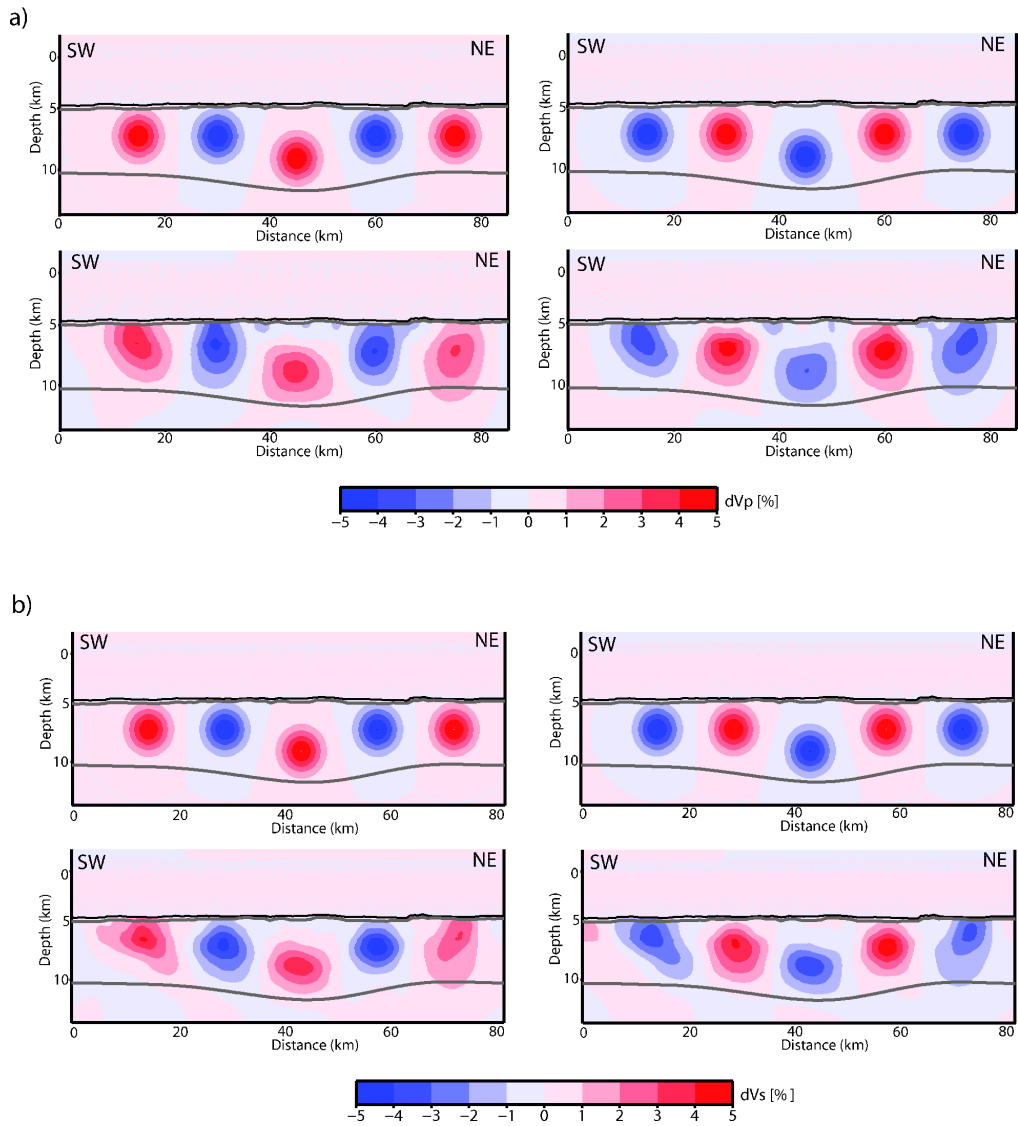


**Figure 4.6:** Resolution tests for a)  $V_p$  model; b)  $V_s$  model.

---

a systematic decrement of  $V_p$  and  $V_s$  in the lower crust between 25 km and 60 km, in comparison to average Monte Carlo models, yielding a lower  $v$  of 0.2 in the same area. We attribute this velocity reduction of  $V_p$  and  $V_s$  to a compensation of the traveltimes due to the imposed restriction of pondering during the inversion 1000 times more the velocity variations than the Moho reflector geometry changes. From the geologic point of view, reduced velocities in the outer rise can be attributed to fracturing and hydration (e.g. *Grevenmeyer et al.*, 2007). Thus, according to the bathymetric map of Figure 4.1, one would expect such low velocity zone in the trench perpendicular direction towards the trench, were bending related faults are observed. For this reason we consider the models of Figure 4.8 more likely, due to its moderate horizontal variation. The results of some tests confirming this election are attached in the Appendix E

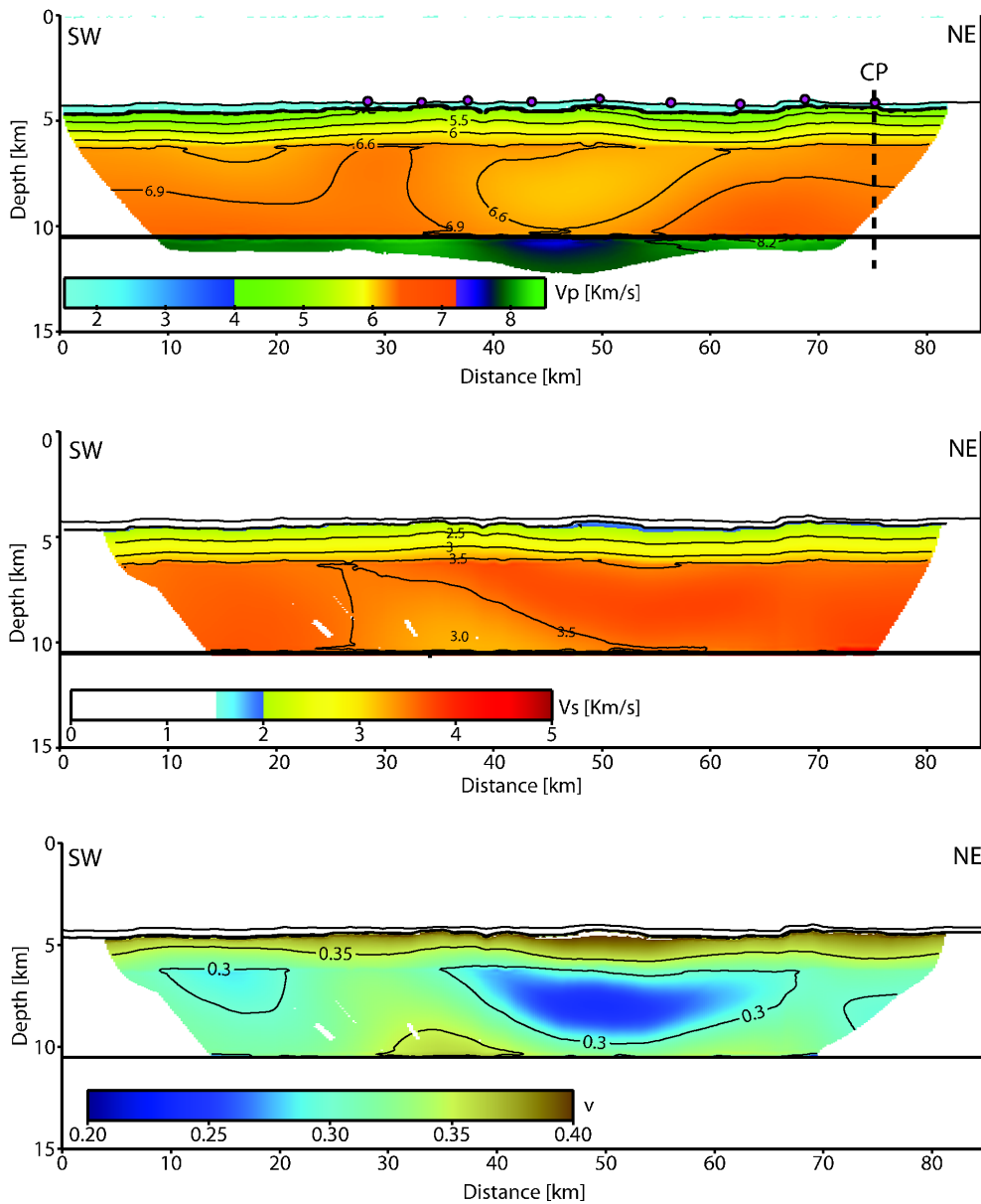


**Figure 4.7:** Final velocity models for  $V_p$  (Top),  $V_s$  (Center) and Poisson's ratio (Bottom) using a flat moho and a kernel  $\omega = 0,01$ , this test shows a velocity-depth trade off for the lower crust. The red dots correspond to the OBS locations, and CP stands for the crossing point with profile P03. The overall error for the models is 95 ms for  $V_p$  and 92 ms for  $V_s$ .

---

## 4.6 Discussion

### 4.6.1 Seismic structure of the oceanic crust in the trench outer rise region

#### Sedimentary layer

Across the profile, we have modeled a thin sedimentary layer of fairly uniform 180 – 300 m depth and its basement tends to mimic the seafloor. The assumed velocities of  $V_p=1.8$  km/s and  $V_s=0.25$  km/s correspond to a  $v = 0.49$ . These values are in agreement with in situ measurements of  $v$  for depth shallower than 100 m below the seafloor, which present  $v$  ranging from 0.46 to 0.49 (*Hamilton, 1976*) and is also consistent with the value of  $v = 0.46$ , found for sediment near the Chile triple junction (*Contreras-Reyes et al., 2008b*).

The sedimentary layer gets thicker towards the trench, resulting in a maximum thickness of 2000 m at the trench axis (*Moscoso et al., 2011*). In the trench fill sediments,  $V_p$  increases gradually from 1.8 km/s on top to 3.5 km/s at the bottom, principally due to compaction and the increase of the sediment size from top to bottom, associated to successive sedimentary deposit events (*Contreras-Reyes et al., 2008a*).

#### Upper crust

The oceanic crust has a thickness of about 6 km and uppermost and lowermost velocities of 4.5 km/s and 7.1 km/s, respectively. Within the crust at  $\sim 6$  depth we can identify for both  $V_p$  and  $V_s$  a change from high to low velocity gradient. This transition zone characterizes the change between the upper and lower crust.

The upper crust is product of a sequence of extrusive basalts on top of a sheeted dike complex characterized by a high velocity gradient (e.g. *Vera et al., 1990*). Our results show:  $V_p$  ranging from 4.0-4.5 km/s on top to 6.5-6.6 km/s at the bottom of a  $\sim 2$  km thick layer, producing a high velocity gradient of  $1.3 s^{-1}$ . The  $V_s$  model presents velocities ranging from 2 km/s on top to 3.5 km/s at the bottom yielding a gradient of  $0.75 s^{-1}$  and  $v$  values decreasing from 0.4 to 0.3, from the top to the bottom, respectively, the highest of the whole crust imaged. Based on sonic velocity logs, *Carlson (2010)* concluded that the

upper oceanic crust is highly fractured, creating secondary porosity. Therefore, fracturing and hydro-alteration might explain the high  $v$  in the upper crust.

### Lower crust

The lower crust is characterized by velocity gradients less steep than in the upper crust, presenting  $V_p$  ranging from 6.6-6.7 km/s on the uppermost part to values near to 7.0 km/s at the bottom, and  $V_s$  values close to 3.5 km/s below the upper-lower crust interface to 4 km/s at the Moho interface. In turn,  $v$  presents decreasing values from 0.3 on top to 0.26-0.27 at the bottom that are overall lower than the Poisson's ratio in the upper crust.

The lithology of the lower crust is dominated by gabbro overlying layered gabbro rocks (e.g. *Vera et al.*, 1990). Large scale in situ values for the uppermost part of the lower crust are  $V_p=6.7$  km/s and  $v = 0.28$  while for its lowermost part are  $V_p=6.9$  km/s and  $v = 0.31$  (*Hyndman*, 1979). In some areas that present reduced lower mantle velocity, it has been suggested the presence of hydrous minerals such as chlorite and amphibolites (e.g. *Christensen and Salisbury*, 1975). A factor that might affect the estimation of the seismic parameters is the anisotropy of metamorphic rocks as amphybolites (*Siegesmund et al.*, 1989) that can constitute 5 to 15 % of gabbros (*Carlson and Miller*, 2004). According to laboratory measurements made at 200 MPa, unaltered dry gabbro might change its velocities of  $V_p = 7.138$  km/s and  $V_s = 3.862$  km/s to  $V_p = 6.866$  km/s and  $V_s = 3.909$  km/s when it metamorphoses to amphybolite, while its Poisson's ratio is reduced from 0.293 to 0.260 (*Christensen*, 1996). Highly altered gabbro samples obtained in the ODP Hole 735B, located in the Atlantis Bank, presented  $V_p$  as low as 6.0 Km/s and  $v$  ranging between 0.28 and 0.30 at 200 MPa (*Iturrino et al.*, 1991).

Although the seismic velocities obtained on our preferred models show little lateral change for the lower crust, the Poisson's ratio reveals lateral heterogeneity. In the uppermost part there are two clear zones of high  $v$ , between 20 km to 40 km and for distances larger than 65 km (Figure 4.8c), which might indicate hydration. According to our model, the sedimentary layer has reduced thickness at the same distances of the high anomalies detected. This perhaps facilitates the infiltration of seawater into the crust. The upper crust is presumably constituted by a highly fractured extrusive overlying brecciated dykes, also called cracked zone (*Lister*, 1974, *Vera et al.*, 1990). These fractures likely constitute pathways for irrigating seawater deeper into the crust. An anomalous low  $v$  is observed in

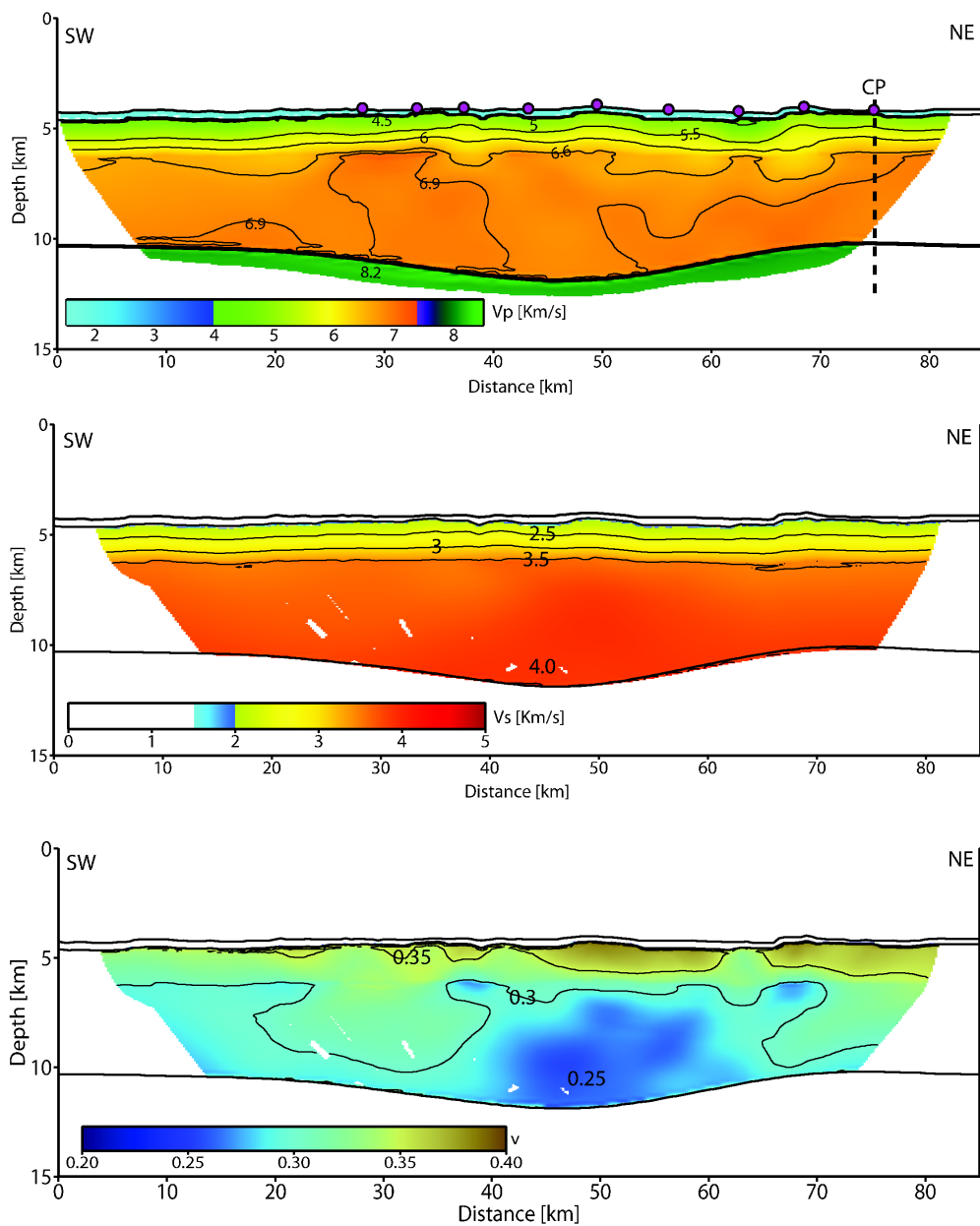


**Figure 4.8:** Final velocity model derived from averaging all Monte Carlo ensembles for a)  $V_p$  and b)  $V_s$ , c)  $v$  masked by the intersection of rays of the P and S wave velocity models. CP in a) stands for the crossing point with P03.



the lowermost part of the crust at a distance between 35 km and 60 km. *Carlson and Miller* (2004) showed that although the compressional velocity does not change, the gabbro might be altered. We observe a similar case near the mocho where  $v$  drops to values close to 0.27 while  $V_p$  is almost unaltered. This fact suggests that the gabbro might be metamorphosed, likely due to the presence of sea water infiltration.

### 4.6.2 Crustal thickness

The Moho geometry is well constrained by PmP reflections, with an error estimated below 500 m at the center of the profile, due to the higher ray coverage on this zone (Figure 4.5c), yielding a minimum crustal thickness of  $\sim 6$  km and a maximum of  $\sim 8$  km.

The presence of a seamount's root product of isostatic compensation is unlikely, due to Maule seamount's modest altitude and the evidence of root's absence beneath the more prominent O'Higgins seamounts, located further north on an area of the Nazca plate of similar age (*Kopp et al.*, 2004). A likely mechanism that might have produced the prominent change of crustal thickness observed in the tomographic image of Figure 4.8a, is at the genesis of the Nazca Plate at this latitude, the Chile Rise. The oceanic crust's thickness is independent of its age and spreading velocity, but strongly dependent on the thermal conditions of the mantle upwelling. Different extents of partial melting of the oceanic upper mantle at its generating ridge can produce small scale variations of the thickness in the axial direction along the ridge (*Canales et al.*, 2003, *Holmes et al.*, 2008, *Mutter and Mutter*, 1993).

### 4.6.3 Hydration of the oceanic lithosphere and upper mantle serpentinization

The  $V_p$  velocity structure along P04, located about 90 km seaward of the trench axis, remains almost constant. However, the most striking feature of the trench perpendicular profile P03 (Figure 4.9a) (*Moscoso et al.*, 2011), is the reduction of crustal and upper mantle velocity approaching the trench axis (Figure 4.9b), indicating changes in the physical properties of the incoming plate. This feature has been reported along strike in the Chilean margin (*Sallarès and Ranero*, 2005, *Contreras-Reyes et al.*, 2008a,b, *Scherwath*

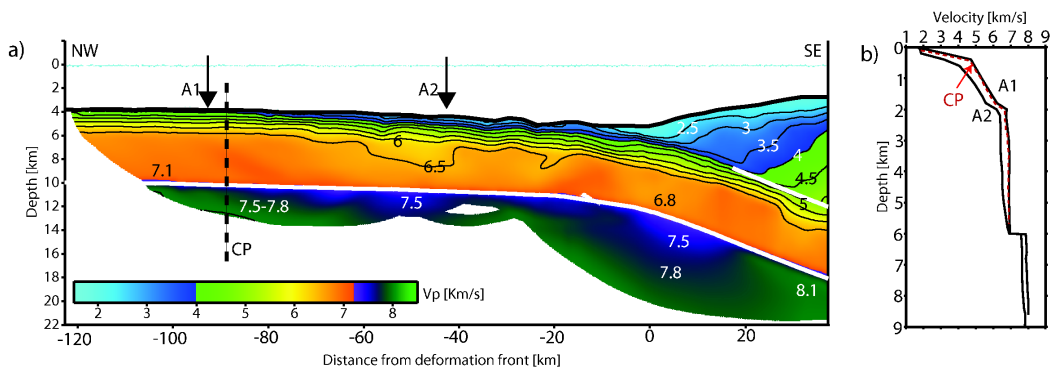


**Figure 4.9:** a) Velocity model of P03, the segmented line CP denotes the crossing point with P04. b) Velocity profiles extracted from the locations of A1 and A2 in a) and the red profile was extracted beneath the crossing point (CP) in profile P04 (Figure 4.8a)

*et al.*, 2009), in the highly hydrated subduction zone offshore Nicaragua (*Grevenmeyer et al.*, 2007, *Ivandic et al.*, 2008), and in the Tonga subduction (*Contreras-Reyes et al.*, in press).

A proposed mechanism for velocity reduction in the trench-outer rise is the creation of bending related faults in the crust in the near-trench region, which possibilities the percolation of sea water into the crust (*Ranero et al.*, 2003, 2005). The reported depth down to which the faults cut into the crust or mantle is around 20 km below the sea floor (*Ranero et al.*, 2003). These large seafloor cutting faults might act as pathways that possibility migration of seawater along the fault to reach and hydrate the uppermost mantle. In south central Chile heat flow decreasing has been observed toward the trench, indicating that the bend faulting facilitates hydrothermal circulation (*Grevenmeyer et al.*, 2005, *Contreras-Reyes et al.*, 2007).

According to the bathymetric data of Figure 4.1 and the seismic models of Figures 4.8a and 4.9a there is a thick blanket of relative impermeable sediments, that block water infiltration into the fault system through the underlying oceanic crust (*Contreras-Reyes et al.*, 2007). However, reflection seismic data on this zone (*Grevenmeyer et al.*, 2005, *Diaz-Naveas*, 1999) show evidence that some of the fissures are capable to reach the seafloor and likely create pathways for sea water circulation into the lithosphere. The decrement of the velocity in the slab is coincident with an increasing roughness in the seafloor which might be an indicator of faults in the basement exposed to the sea water (see Figure 4.9a). Another effective link between the basement and the sea water is through outcrops and seamounts,

as the Maule seamount (Figure 4.1). Seamounts can guide hydrothermal recharge and discharge between sites separated by large distances due to percolation through their flanks in direct contact with seawater (*Fisher et al.*, 2003). Although both mechanisms, fracturing and hydration, produce a decrement of the seismic velocity, they are related to each other making it difficult to discriminate between them based on seismic properties. Offshore Nicaragua, *Ivandic et al.* (2010) show a profound correlation between the occurrence of velocity anomalies and seamounts, suggesting a close link between seamounts and hydration.

Laboratory seismic measurements made on ophiolite dry samples of ultramafic rocks as dunite at 200 MPa, present  $V_p$  of 8.299 km/s (*Christensen*, 1996). For samples of peridotite the values estimated are  $V_p$  of 8.4 (*Hyndman*, 1979). For serpentinite samples at 200 MPa, the seismic velocities reduce drastically to  $V_p$  of 5.308 (*Christensen*, 1996). Along P04 we obtained average mantle velocities of  $V_p$  of 8.17 km/s,  $V_p$  values present a reduced velocity in comparison with the values correspondent to dry and unaltered mantle. This suggests that we are in presence of hydration of the upper mantle and partial serpentinization. According to our results, the degree of serpentinization of the upper mantle is estimated around 10%.

#### 4.6.4 Upper mantle anisotropy

Azimuthal P-wave anisotropy in the upper mantle is well established by seismic refraction experiments (e.g. *Shearer and Orcutt*, 1986, *Bée and Bibee*, 1989, *Contreras-Reyes et al.*, 2008b) and also suggested by surface wave studies (*Park and Levin*, 2002). The velocity anisotropy can be described by a sinusoidal function of azimuth with the fast direction, generally parallel to the original spreading direction, as result of the preferred orientation of olivine crystals (*Hess*, 1964). For dry olivine, the a axis presents the fastest and b the slowest  $V_p$  (*Verma*, 1960). *Hess* (1964) proposed that mantle anisotropy originated from preferred olivine orientation based on evidence of Pn velocities anisotropy in the north-east Pacific. Plots of velocities versus azimuth on this region showed that upper mantle compressional-wave velocities were fast for propagation directions approximately parallel to fracture zones. Hence, the direction of the fastest P-wave velocity is usually assumed to indicate the flow direction in the mantle (e.g. *Zhang and Karato*, 1995, *Park and Levin*, 2002). The described behavior might not be valid for environments highly hydrated and/or

---

under a high stress field (e.g. *Katayama et al.*, 2009). Due to the effect of water in the anisotropic deformation of olivine, the high speed axis is reoriented with the low speed axis nearly parallel to the shear direction (*Jung and Karato*, 2001), implying that the high speed axis becomes perpendicular to plate motion (*Ando et al.*, 1983). Additionally, high pressure conditions produce in the olivine the same crystallographic preferred orientation that by high water activity at lower pressure (*Jung et al.*, 2009).

To estimate the degree of anisotropy of Pn velocities, we extracted from the trench parallel velocity model P04 a track 500 m beneath the Moho. It yielded a media velocity of  $V_p=8.17$  km/s. For the velocity model of P03, perpendicular to P04 and to the trench, we also extracted a similar velocity profile in the vicinity of the crossing point between the profiles, which yielded a media velocity of  $V_p=7.5$  km/s. Therefore the Pn anisotropy is near 8%, with a preferential higher velocity direction parallel to the trench axis, this value is higher than the value found in a younger section of the Nazca plate located at  $\sim 43^\circ S$ , near the Chile triple junction (CTJ)(*Contreras-Reyes et al.*, 2008b).

The direction of maximum  $V_p$  for the upper mantle, observed along P04, coincides with the spreading center fabric as shown in Figure 4.1. This finding suggests that in the vicinity of P04, the upper mantle is not strongly altered by hydration, but this state probably changes as the plate approaches the trench where  $V_p$  presents a reduction of  $V_p$ , likely due to water infiltration (see Figure 4.9). Based on the behavior reported on samples of upper mantle rocks under hydration and high deformation (*Zhang and Karato*, 1995, *Katayama et al.*, 2009), we speculate that near the trench, the orientation of the high velocity axis should tend to align perpendicular to the spreading direction axis.

#### **4.6.5 Outer rise seismic activity**

For the hypocentral determination, we employed 1-D  $V_p$  and  $V_s$  models, derived from the seismic refraction tomography of Figures 4.8a and 4.8b. The location of the 29 events was inferred using the linear location program HYP, included in SEISAN (*Havskov and Ottemöller*, 1999).

The set of events analyzed, shown in Figure 4.10, suggest the existence of a zone of high seismic activity beneath the seamount to a depth of  $\sim 30$ . This intraplate seismicity is consistent with the faults imaged in the bathymetry, shown in Figure 4.1, and seems to

be product of the reactivation of normal faults formed by plate bending near the trench (Ranero *et al.*, 2005). It is thought that the shallow outer rise seismicity ( $< 30$  km) is triggered by the increment of pore pressure within the fault system produced by infiltration of sea water into the lithosphere (Tilmann *et al.*, 2008). However, bending related faulting itself might be an important mechanism of recurrence of earthquakes and may act as a fault valve, causing seismic pumping (Grevemeyer *et al.*, 2007). Therefore, the high seismicity nearby the seamount might be explained by a higher fracturing and hydration of the crust.

The shallow outer rise seismic activity might also be related to large interplate earthquakes in the subduction zone. Kato and Hirasawa (2000) showed through a numerical simulation, that a large tensional outer rise earthquake tends to advance the occurrence time and reduces the magnitude of the next interplate earthquake, while a compressional one tends to delay the occurrence of a large interplate earthquake. In the other hand, large underthrusting events might transfer tensional stresses along the slab and subsequently trigger intraplate earthquakes in the outer rise (Christensen and Ruff, 1983, 1988).

The Maule area presented little background seismic activity in comparison to the rest of the Chilean margin (Campos *et al.*, 2002). This is probably due to the high locking in the interplate between Constitución and Concepción (Ruegg *et al.*, 2009). However, during the months following the mainshock, several events occurred in the outer rise area between  $\sim 34^{\circ}S$  and  $\sim 35^{\circ}30'S$ . There were even 6 events with magnitude over 5.0 during the year following the main shock, as it is shown in Figure 4.10. It is likely that the stress accumulated in the Concepción-Constitución seismic gap over 130 years (Madariaga *et al.*, 2010), once released produced a large slip zone between  $\sim 34^{\circ}S$  and  $\sim 35^{\circ}30'S$  (Delouis *et al.*, 2010, Moreno *et al.*, 2010) (also coincident with a wider shelf, as can be seen in Figure 4.10). This effect led a transport of slab pull stress to the outer rise, reactivating the bending related normal faults of the oceanic plate and perhaps producing new fissures, that might trigger new seismic events in the neighboring area. In addition to plate bending, the fracturing and hydration wakes the oceanic plate when approaching the trench (Contreras-Reyes and Osses, 2010, Chapple and Forsyth, 1979, Kao and Chen, 1996) intensifying the outer rise earthquake genesis process (Lefeldt *et al.*, 2009).

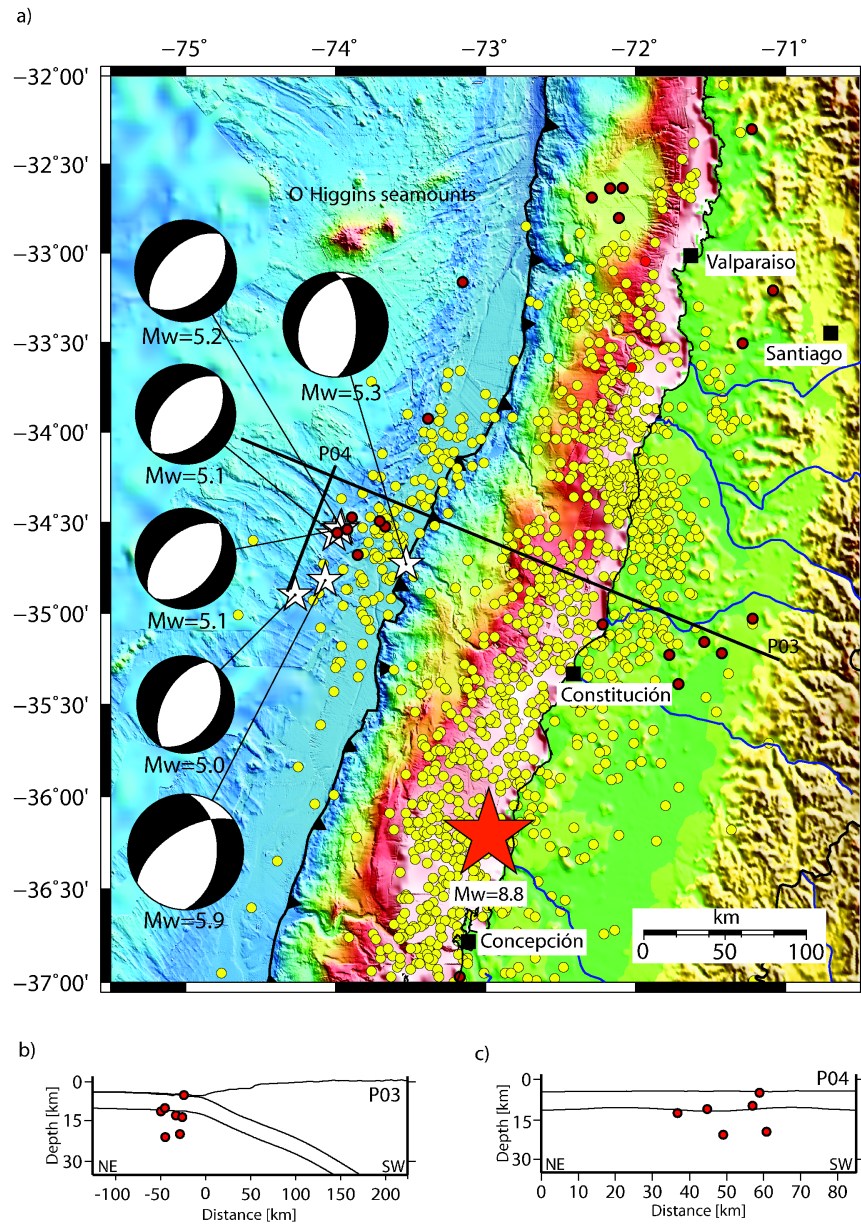


**Figure 4.10:** a) Aftershocks of the Maule earthquake: yellow dots represent the events up to 3 months after the main shock from NEIC catalogue and the white stars stand for outer rise events with Magnitude higher than 5 within one year after the earthquake, with its respective Harvard CMT fault plane solutions. The black solid lines mark the locations of the profiles P03 and P04. The local earthquakes recorded by our outer rise network operative between March and April of 2008, are represented by red dots. Their projection over P03 and P04 are in b) and c), respectively.

## 4.7 Conclusions

We analyzed high resolution bathymetric, seismological and active seismic data to investigate the structure of the incoming plate prior to its subduction, in the trench outer rise area offshore Maule, Chile, between  $34^{\circ}S$  and  $35^{\circ}S$ . In particular, wide angle seismic data was used to obtain the high resolution 2D velocity structure and derive the Poisson's ratio distribution of the Nazca plate on this area. From this study we have concluded the following:

1. As the incoming plate approaches the trench, the  $V_p$  velocity tends to reduce in both, oceanic crust and upper mantle. Those anomalies observed in the compressional velocity is likely produced by a combination of progressive bending related faulting and subsequent hydration by water percolation. The reduction of the upper mantle velocities near the trench, might reflect partial serpentinization of the mantle peridotites, that we estimate is around 10%.
2. The possible differences of the crustal thickness observed along strike in the profile P04 are probably due to mantle upwelling and not by isostatic compensation of the neighboring Maule seamount.
3. The upper mantle presents a  $V_p$  anisotropy estimated in  $\sim 8\%$ , with the faster velocity axis parallel to the trench. This finding confirms a low degree of alteration of the upper mantle in the areas where the oceanic plate presents low fracturing.
4. We found shallow seismic activity in the outer rise area near the seamount, we conclude that this seismicity is produced due to generation and activation of outer rise faults. To the bending-related faulting we have to add the presence of the Maule seamount that probably intensifies the percolation of seawater into the deep structures producing an intense hydrothermal activity, and likely an increment in the pore pressure.
5. The main shock of the 2010 Maule earthquake, triggered an anomalous high seismic activity in the trench outer rise area, likely due to the transmission of stress along the incoming plate, that might have produced a massive crack opening of the bending faults and subsequently water intrusion into the lithosphere.

- 
6. All the previous conclusions indicate presence of sea water in the upper lithosphere near the trench, that produces changes on its seismic properties and likely in the petrology.



# Chapter 5

## Final discussion

In the present work were analyzed high resolution bathymetric, seimological and active seismic data to investigate the structure of the incoming plate prior to its subduction and the relationship between the seismic structure of the margin and the updip extension of the seismogenic zone on- and off- shore Maule, Chile, between  $34^{\circ}S$  and  $35^{\circ}S$ . In the following some aspects of the results previously presented as stand alone articles in Chapters 3 and 4 will be discussed.

### 5.1 Seismogenic zone in the Maule region and 2010 earthquake nucleation zone

In Chapter 3, the relation between the backstop and the updip of the seismogenic zone was discussed. The results presented in Figure 3.6 suggest that the updip is controlled by the transition between consolidated and unconsolidated sediments, evidenced by a high horizontal  $V_p$  gradient. The downdip determination is out of the scope of the present work, however, a first order estimation can be made by a extrapolation of the interplate boundary up to the landward limit of the aftershocks, beneath the Longitudinal Valley (Figure 4.10). Under the assumption that the dip angle, estimated to be  $10^{\circ}$ , does not vary much along the seismogenic zone, the projected depth at the landward limit of the rupture zone yields a depth of 50 km, which is consistent with the location of the continental Moho (*Heit et al.*,

---

2008) and thus with the beginning of the stable sliding zone (see Figure 1.2).

The nucleation of the Maule earthquake at some 20 km depth is consistent with the depth of 22 km reported by the CMT catalog. It roughly coincides with the contact between the proposed location of the upper/lower continental crust reflector, shown in Figure 3.7. The model of asperities and barriers shown in Figure 1.2 suggests that this continental interface is a candidate for an asperity, where the stress accumulated over more than a century in the area comprised between Constitución and Concepción.

## **5.2 Seismic structure of the upper oceanic lithosphere and hydration**

The outer rise area was revealed by two wide-angle seismic profiles parallel (Figure 4.8), and perpendicular to the trench (Figure 4.9), that show that the oceanic plate is covered by a thin and highly hydrated sedimentary layer of  $\sim 200 - 400$  m depth with increasing thickness as the plate approaches the trench, rising to a maximum of  $\sim 2000$  m at the trench axis with a nearly constant  $V_p=1.8$  km/s. The 2 km thick upper crust is characterized by a high seismic velocity gradient and high values of Poisson's ratio. The latter indicates a high degree of hydration. The highest lateral differences of  $v$  along P04 and  $V_p$  in P03 are observed within the lower crust. In the lowermost part of the lower crust, the anomalous low  $v$  might reflect metamorphism of the gabbros, likely produced by hydration.

The reduced  $V_p$  values observed in Figure 4, when the plate approaches the deformation front, suggests a high hydration likely produced by reactivation of normal bending faults in the outer rise and intensified by hydrothermal circulation due to the existence of the neighboring Maule Seamount. The hypothesis that the upper mantle is hydrated is supported by reduced  $V_p$  that also might indicate partial serpentinization of the mantle peridotites, that is estimated in around 10%. The differences of the crustal thickness observed along profile P04 are probably due to mantle upwelling and not by isostatic compensation produced by the neighboring Maule seamount.

### 5.3 Outer rise seismicity

The Chile Subduction Zone is characterized by clusters of shallow ( $< 30$  km depth) outer rise seismic activity due to the incoming plate bending, normal fracturing reactivation and subsequent plate hydration process (Tilmann *et al.*, 2008). Figure 5.1 presents a compilation of seismicity from the USGS (NEIC) catalog (green dots, from 01/01/2008 to 26/02/2010; yellow dots, stand for the events occurred between the main shock three months after it), and Harvard (CMT) catalog, as well as microseismicity collected by the ORN during the March and April of 2008 (red dots). On this Figure, it can be clearly seen that during the years previous to the main shock, the seismicity on- and off- shore Maule presented little activity in comparison with other segments of the Chilean subduction zone, likely due to the high locking between the incoming plate and the continent between Constitución and Concepción (Campos *et al.*, 2002). The most important offshore event prior to the Maule earthquake, occurred almost seven years before the Megathrust earthquake on 28/2/2003, when a  $M_w=5.3$ , 15 km depth compressional event (CMT catalog) hit the outer rise area offshore Constitución.

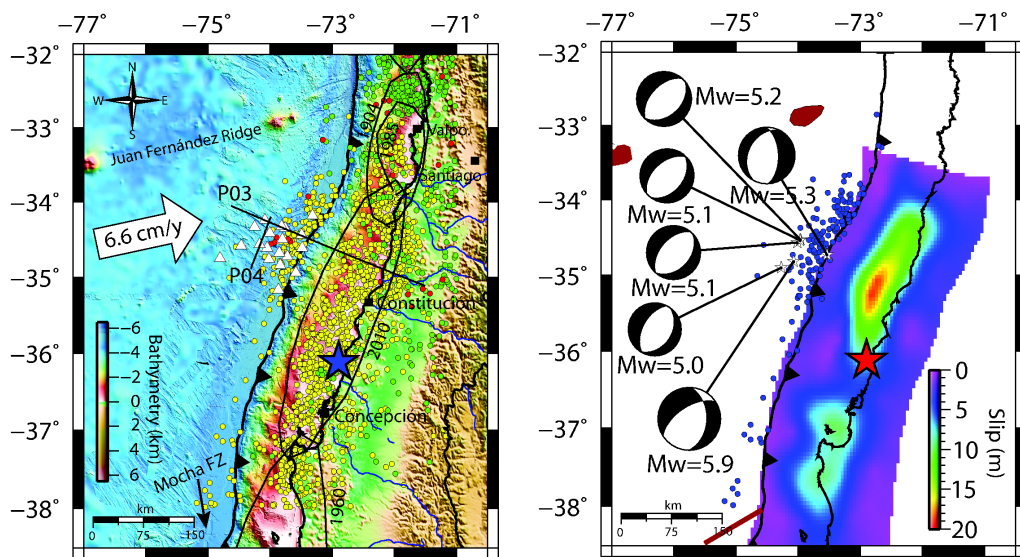


**Figure 5.1:** a) Map showing the seismicity prior the to Maule earthquake from NEIC prior (green dots) and after the Maule earthquake (yellow), ORN (red dots) and CMT catalog (Compressional earthquake with  $M_w = 5.3$ ); b) Slip distribution from Lorito *et al.* (2011), and its spatial correlation with the outer rise seismicity during the co-seismic period. The focal mechanisms correspond to events in the outer rise with  $M_w > 5.0$ .

---

The previously described situation changed radically after the main shock in 2010. Within the three months after the 27th of February, almost 480 outer rise events of  $M_w > 4$  were reported by NEIC catalog in the trench outer rise area. A cluster of high seismicity between the  $33.5^\circ S$  and  $35.5^\circ S$  was formed in the outer rise. In this sense, Figure 1b shows that this cluster is coincident with the northern maximum co-seismic slip of the Maule earthquake (Lorito *et al.*, 2011). Within the year following the Maule earthquake, 6 tensional outer rise events  $M_w > 5.0$  located seaward the northern maximum slip, were reported by the catalog.

The strong spatial correlation between the northern asperity and outer rise seismicity following the Maule megathrust earthquake shown in Figure 5.1b, suggests that tensional stresses are transferred in a more effective manner in regions seaward of large co-seismic slip. During the co-seismic, due to the underthrusting motion, slab pull forces are transmitted seawards through the plate, reactivating and likely creating new normal faults at the trench-outer rise, thus producing tensional outer rise events (Christensen and Ruff, 1988). In the interseismic, the high stress accumulation over more than a century in the Constitución-Concepción seismic gap was evidenced by 10 m slip deficit (Ruegg *et al.*, 2009). This scenario favored the occurrence of compressional outer rise events, characteristic of mature seismic gaps (Christensen and Ruff, 1988).

The shallow seismic activity found in the outer rise area near the Maule seamount, suggests that the reactivation and generation of normal faults, is triggered by plate bending, tensional stress transmission by the slab and likely the increment of pore pressure due to sea water percolation. The presence of the Maule seamount probably intensifies the percolation of seawater into the deep structures, producing an intense hydrothermal activity. The anomalous high seismic activity in the trench outer rise area, triggered by the main shock of the 2010 Maule earthquake, likely due to the transmission of stress along the incoming plate, might have produced a massive crack-opening of the bending faults and subsequently water intrusion into the lithosphere.

# Bibliography

- Ando, M., Y. Ishikawa, and F. Yamazaki, Shear Wave Polarization Anisotropy in the Upper Mantle Beneath Honshu, Japan, *Journal of Geophysical Research*, 88, 5850–5864, 1983.
- Angermann, D., J. Klotz, and C. Reigber, Space-geodetic estimation of the Nazca-South America Euler vector, *Earth and Planetary Science Letters*, 171, 329–334, 1999.
- Arriagada, C., et al., Nature and tectonic significance of co-seismic structures associated with the Mw 8.8 Maule earthquake, central-southern Chile forearc, *Journal of Structural Geology*, in press.
- Au, D., and R. Clowes, Shear-wave velocity structure of the oceanic lithosphere from ocean bottom seismometer studies, *Geophys. J. R. astr. Soc.*, 77, 105–123, 1984.
- van Avendonk, H., A. Harding, J. Orcutt, and J. McClain, two-dimensional tomographic study of the Clipperton transform fault, *Journal of Geophysical Research*, 103, 17,885–17,899, 1998.
- Barrientos, S., Giant returns in time, *Nature*, 737, 329, 2005.
- Barrientos, S. E., and S. N. Ward, The 1960 Chile earthquake: Inversion for slip distribution from surface deformation, *Geophysical Journal International*, 103, 589–598, 1990.
- Beck, S., S. Barrientos, E. Kausel, and M. Reyes, Source characteristics of historic earthquakes along the central Chile subduction zone, *Journal of South American Earth Sciences*, 11, 115–129, 1998.
- Bée, M., and L. D. Bibee, A seismic refraction study of cretaceous oceanic lithosphere in the Northwest Pacific Basin, *Marine Geophysical Researches*, 11, 239–261, 1989.

- 
- Bejar-Pizarro, M., et al., Asperities and barriers on the seismogenic zone in North Chile: state-of-the-art after the 2007 Mw 7.7 Tocopilla earthquake inferred by GPS and InSAR data, *Geophysical Journal International*, 183, 390–406, 2010.
- Bialas, J., and E. R. Flueh, Ocean bottom seismometers, *Sea Technol.*, 40, 41–46, 1999.
- Bilek, S. L., Invited review paper: Seismicity along the South American subduction zone: Review of large earthquakes, tsunamis, and subduction zone complexity, *Tectonophysics*, 495, 2–14, 2009.
- Blumberg, S., F. Lamy, H. Arz, H. Echtler, M. Wiedicke, G. Haug, and O. Oncken, Turbiditic trench deposits at the South-Chilean active margin: A Pleistocene-Holocene record of climate and tectonics, *Earth and Planetary Science Letters*, 268, 526–539, 2008.
- Byrne, D., D. Davis, and L. Sykes, LOCI AND MAXIMUM SIZE OF THRUST EARTHQUAKES AND THE MECHANICS OF THE SHALLOW REGION OF SUBDUCTION ZONES, *Tectonics*, 7, 833–857, 1988.
- Campos, J., and E. Kausel, The large 1939 intraplate earthquake of southern Chile, *Seismological Research Letters*, 61, 1990.
- Campos, J., et al., A seismological study of the 1835 seismic gap in south-central Chile, *Physics of The Earth and Planetary Interiors*, 132, 177–195, 2002.
- Canales, J. P., R. S. Detrick, D. R. Toomey, and W. S. D. Wilcock, Segment-scale variations in the crustal structure of 150-300 kyr old fast spreading oceanic crust (East Pacific Rise,  $8^{\circ}15'N - 10^{\circ}5'N$ ) from wide-angle seismic refraction profiles, *Geophysical Journal International*, 3, 766–794, 2003.
- Carlson, R. L., How crack porosity and shape control seismic velocities in the upper oceanic crust: Modeling downhole logs from Holes 504B and 1256D, *Geochemistry, Geophysics and Geosystems*, 11, 2010.
- Carlson, R. L., and D. J. Miller, Influence of pressure and mineralogy on seismic velocities in oceanic gabbros: Implications for the composition and state of the lower oceanic crust, *Journal of Geophysical Research*, 109, 2004.
- Chapple, W., and D. Forsyth, Earthquakes and Bending of Plates at Trenches, *Journal of Geophysical Research*, 84, 6729–6749, 1979.

- Christensen, D., and L. Ruff, SEISMIC COUPLING AND OUTER RISE EARTHQUAKES, *Journal of Geophysical Research*, *93*, 13,421–13,444, 1988.
- Christensen, D. H., and L. J. Ruff, Outer-rise earthquakes and seismic coupling, *Geophysical Research Letters*, *10*, 697–700, 1983.
- Christensen, N., Poisson's ratio and crustal seismology, *Journal of Geophysical Research*, *101*, 3139–3156, 1996.
- Christensen, N. I., and M. H. Salisbury, Structure and constitution of the lower oceanic crust, *Reviews of Geophysics*, *13*, 57–86, 1975.
- Cifuentes, I., and P. Silver, Low-Frequency Source Characteristics of the Great 1960 Chilean Earthquake, *Journal of Geophysical Research*, *94*, 643–663, 1989.
- Cisternas, M., et al., Predecessors of the giant 1960 Chile earthquake, *Nature*, *437*, 404–407, 2005.
- Contreras-Reyes, E., and D. Carrizo, Control of high oceanic features and subduction channel on earthquake ruptures along the Chile-Peru subduction zone, *Physics of the Earth and Planetary Interiors*, *186*, 49–58, 2011.
- Contreras-Reyes, E., and A. Osses, Lithospheric flexure modeling seaward of the Chile trench: Implications for oceanic plate weakening in the Trench Outer Rise region, *Geophysical Journal International*, *182*, 97–112, 2010.
- Contreras-Reyes, E., I. Grevemeyer, E. R. Flueh, M. Scherwath, and M. Heesemann, Alteration of the subducting oceanic lithosphere at the southern central Chile trench-outer rise, *Geochemistry, Geophysics and Geosystems*, *8*, 2007.
- Contreras-Reyes, E., I. Grevemeyer, E. R. Flueh, and C. Reichert, Upper lithospheric structure of the subduction zone offshore southern Arauco Peninsula, Chile at 38°S, *Journal of Geophysical Research*, *113*, 2008a.
- Contreras-Reyes, E., I. Grevemeyer, E. R. Flueh, M. Scherwath, and J. Bialas, Effect of trench-outer rise bending-related faulting on seismic Poisson's ratio and mantle anisotropy: a case study offshore of Southern Central Chile, *Geochemistry, Geophysics and Geosystems*, *173*, 142–156, 2008b.

- 
- Contreras-Reyes, E., E. R. Flueh, and I. Grevemeyer, Tectonic control on sediment accretion and subduction off south-central Chile: Implications for coseismic rupture processes of the 1960 and 2010 megathrust earthquakes, *Tectonics*, 29, 2010.
- Contreras-Reyes, E., I. Grevemeyer, A. Watts, E. R. Flueh, C. Peirce, S. Moeller, and C. Papenberg, Deep seismic structure of the Tonga subduction zone: implications for mantle hydration, tectonic erosion, and arc magmatism, *Journal of Geophysical Research*, in press.
- Darwin, C., Geological Observations of South America, *Smith and Elder, London*, 279 pp., 1851.
- Delouis, B., J.-M. Nocquet, and M. Vallee, Slip distribution of the February 27, 2010 Mw = 8.8 Maule Earthquake, central Chile, from static and high-rate GPS, InSAR, and broadband teleseismic data, *Geophysical Research Letters*, 37, 2010.
- DeMets, C., R. G. Gordon, D. F. Argus, and S. Stein, Effect of recent revisions to the geomagnetic reversal time scale on estimates of current plate motions, *Geophysical Research Letters*, 21, 2191–2194, 1994.
- Diaz-Naveas, J. L., Sediment subduction and accretion at the Chilean convergent margin between 35°S and 40°S, Ph.D. Thesis, Master's thesis, Christian-Albrechts-Universität, Kiel, Germany, 1999.
- Dijkstra, E. W., A note on two problems in connexion with graphs, *Numerische Mathematik*, 1, 269–271, 1959.
- Dixon, T. H., and J. Moore, *The Seismogenic Zone of Subduction Thrust Faults.*, New York: Columbia University Press, 2007.
- Fisher, A. T., et al., Hydrothermal recharge and discharge across 50 km guided by seamounts on a young ridge flank, *Nature*, 421, 618–621, 2003.
- Flueh, E. R., and J. Bialas, A digital, high data capacity ocean bottom recorder for seismic investigations, *International Underwater System Design*, 18, 18–20, 1996.
- Flueh, E. R., and J. Bialas, Cruise report JC23, *Tech. Rep. rep. 20*, IFM-Geomar, 2008.
- González, E., Hydrocarbon resources in the coastal zone of Chile, in Ericksen, G., et al., eds., *Geology of the Andes and its relation to hydrocarbon and mineral resources:*



- Houston, Texas, Circum-Pacific Council for Energy and Mineral Resources, *Circum-Pacific Council for Energy and Mineral Resources: Houston, Texas*, p. 383-404, 1989.
- Grevemeyer, I., W. Weigel, and C. Jennrich, Structure and ageing of oceanic crust at 14°S on the East Pacific Rise, *Geophysical Journal International*, 135, 573–584, 1998.
- Grevemeyer, I., J. L. Diaz-Naveas, C. R. Ranero, H. W. Villinger, and O. D. P. L. . S. Party, Heat flow over the descending Nazca plate in central Chile, 32°S to 41°S: observations from ODP Leg 202 and the occurrence of natural gas hydrates, *Earth and Planetary Science Letters*, 213, 285–298, 2003.
- Grevemeyer, I., N. Kaul, J. Diaz-Naveas, H. Villinger, C. Ranero, and C. Reichert, Heat flow and bending-related faulting at subduction trenches: case studies offshore of Nicaragua and Central Chile, *Earth and Planetary Science Letters*, 236, 238–248, 2005.
- Grevemeyer, I., C. R. Ranero, E. R. Flueh, D. Klaeschen, and J. Bialas, Passive and active seismological study of bending-related faulting and mantle serpentinization at the Middle America trench, *Earth and Planetary Science Letters*, 2007.
- Haberland, C., A. Rietbrock, D. Lange, K. Bataille, and T. Dahm, Structure of the seismogenic zone of the southcentral Chilean margin revealed by local earthquake traveltime tomography, *Journal of Geophysical Research*, 114, 2009.
- Hacker, B. R., H<sub>2</sub>O subduction beyond arcs, *Geochemistry, Geophysics and Geosystems*, 9, 2008.
- Hamilton, E. L., Shear-wave velocity versus depth in marine sediments: a review, *Geophysics*, 41, 985–996, 1976.
- Havskov, J., and L. Ottemöller, SeisAn Earthquake analysis software, *Seismological Research Letters*, 70, 532–534, 1999.
- Heit, B., X. Yuan, M. Bianchi, F. Sodoudi, and R. Kind, Crustal thickness estimation beneath the southern central Andes at 30°S and 36°S from S wave receiver function analysis, *Geophysical Journal International*, 174, 249–254, 2008.
- Herron, E., S. Cande, and B. Hall, An active spreading center collides with a subduction zone: a geophysical survey of the Chile Margin triple junction, *Geological Society of America. Memoir*, 154, 683–701, 1981.

- 
- Hervé, F., F. Munizaga, M. Parada, M. Brook, R. Pankhurst, N. Snelling, and R. Drake, Granitoids of the Coast Range of central Chile: Geochronology and geologic setting, *Journal of South American Earth Sciences*, *1*, 185–194, 1988.
- Hess, H. H., Seismic Anisotropy of the Uppermost Mantle under Oceans, *Nature*, *203*, 629–631, 1964.
- Hole, J. A., Nonlinear High-Resolution Three-Dimensional Seismic Travel Time Tomography, *Journal of Geophysical Research*, *97*, 6553–6562, 1992.
- Holmes, R., M. Tolstoy, J. R. Cochran, and J. S. Floyd, Crustal thickness variations along the Southeast Indian Ridge (100° – 116°E) from 2-D body wave tomography, *Geochemistry, Geophysics and Geosystems*, *9*, 2008.
- von Huene, R., J. Corvalán, E. Flueh, K. Hinz, J. Korstgard, C. Ranero, and W. Weinrebe, Tectonic control of the subducting Juan Fernández Ridge on the Andean margin near Valparaíso, *Tectonics*, *16*, 474–488, 1997.
- Hyndman, R., M. Yamano, and D. Oleskevich, The seismogenic zone of subduction thrust faults, *Island Arc*, *6*, 244–260, 1997.
- Hyndman, R. D., Poisson's ratio in the oceanic crust: a review, *Tectonophysics*, *59*, 321–333, 1979.
- Iturrino, G. J., N. I. Christensen, S. Kirby, and M. H. Salisbury, Seismic velocities and elastic properties of gabbroic rocks from Hole 735B. In Von Herzen, R.P., Robinson, P.T., et al., *Proc. ODP, Sci. Results, 118: College Station, TX (Ocean Drilling Program)*, *113*, 1991.
- Ivandic, M., I. Grevemeyer, A. Berhorst, E. R. Flueh, and K. McIntosh, Impact of bending related faulting on the seismic properties of the incoming oceanic plate offshore of Nicaragua, *Journal of Geophysical Research*, *113*, 2008.
- Ivandic, M., I. Grevemeyer, J. Bialas, and C. J. Petersen, Serpentinization in the trench-outer rise region offshore of Nicaragua: Constraints from seismic refraction and wide-angle data, *Geophysical Journal International*, 2010.
- Jung, H., and S. Karato, Water-Induced Fabric Transitions in Olivine, *Science*, *293*, 1460–1463, 2001.

- Jung, H., M. Wo, and H. W. Green, Upper mantle seismic anisotropy resulting from pressure-induced slip transition in olivine, *Nature Geoscience*, 2, 73–77, 2009.
- Kanamori, H., Seismological evidence for a lithospheric normal faulting - the sanriku next term earthquake of 1933, *Physics of The Earth and Planetary Interiors*, 4, 289–300, 1971.
- Kao, H., and W.-P. Chen, Seismicity in the outer rise-forearc region and configuration of the subducting lithosphere with special reference to the Japan Trench, *Journal of Geophysical Research*, 101, 27,811–27,831, 1996.
- Katayama, I., K. Hirauchi, K. Michibayashi, and J. Ando, Trench-parallel anisotropy produced by serpentine deformation in the hydrated mantle wedge, *Nature*, 461, 1114–1117, 2009.
- Kato, N., and T. Hirasawa, Effect of a large outer rise earthquake on seismic cycles of interplate earthquakes: A model study, *Journal of Geophysical Research*, 105, 653–662, 2000.
- Klingelhoefer, F., et al., Limits of the seismogenic zone in the epicentral region of the 26 December 2004 great Sumatra-Andaman earthquake: Results from seismic refraction and wide-angle reflection surveys and thermal modeling, *Journal of Geophysical Research*, 115, 2010.
- Kopp, H., E. R. Flueh, C. Papenberg, and D. Klaeschen, Seismic investigations of the O'Higgins Seamount Group and Juan Fernández Ridge: Aseismic ridge emplacement and lithosphere hydration, *Tectonics*, 23, 2004.
- Korenaga, J., Velocity-depth ambiguity and the seismic structure of large igneous provinces: a case study from the ontong java plateau, *Geophysical Journal International*, 2011.
- Korenaga, J., W. Holbrook, G. Kent, P. Kelemen, R. Detrick, H. Larsen, J. Hopper, and T. Dahl-Jensen, Crustal structure of the southeast Greenland margin from joint refraction and reflection seismic tomography, *Journal of Geophysical Research*, 105, 21,591–21,614, 2000.
- Lefeldt, M., I. Grevemeyer, J. Gossler, and J. Bialas, Intraplate seismicity and related mantle hydration at the Nicaraguan trench outer rise, *Geophysical Journal International*, 178, 742–752, 2009.

- 
- Lister, C. R. B., On the penetration of water into hot rock, *Geophys. J. R. Astronom. Soc.*, 39, 465–509, 1974.
- Lloyd, S., S. van der Lee, G. S. França, M. Assumpção, and M. Feng, Moho map of South America from receiver functions and surface waves, *Journal of Geophysical Research*, 115, 2010.
- Lorito, S., F. Romano, S. Atzori, X. Tong, A. Avallone, J. McCloskey, M. Cocco, E. Boschi, and A. Piatanesi, On the penetration of water into hot rock, *Nature Geoscience*, 4, 173–177, 2011.
- Madariaga, R., M. Métois, C. Vigny, and J. Campos, Central Chile Finally Breaks, *Science (in Perspectives)*, 328, 181–182, 2010.
- Marone, C., and C. H. Scholz, The depth of seismic faulting and the upper transition from stable to unstable slip regimes, *Geophysical Research Letters*, 15, 621–624, 1988.
- Melnick, D., B. Bookhagen, H. P. Echtler, and M. R. Strecker, Coastal deformation and great subduction earthquakes, Isla Santa María, Chile (37°S), *Geological Society of America Bulletin*, 118, 1463–1480, 2006.
- Mordojevich, C., Geology of a part of the Pacific margin of Chile: The Geology of Continental Margins, pp. 591–598, 1974.
- Moreno, M., M. Rosenau, and O. Oncken, 2010 Maule earthquake slip correlates with pre-seismic locking of Andean subduction zone, *Nature*, 467, 198–202, 2010.
- Moscoso, E., I. Grevemeyer, E. Contreras-Reyes, E. R. Flueh, Y. Dzierma, W. Rabbel, and M. Thorwart, Revealing the deep structure and rupture plane of the 2010 Maule, Chile earthquake (Mw = 8.8) using wide angle seismic data, *Earth and Planetary Science Letters*, 307, 147–155, 2011.
- Moser, T., Shortest path calculation of seismic rays, *Geophysics*, 56, 59–67, 1991.
- Moser, T., G. Nolet, and R. Snieder, Ray bending revisited, *Bulletin Seismological Society of America*, 82, 259–288, 1992.
- Müller, R. D., W. R. Roest, J. Royer, L. M. Gahagan, and J. G. Sclater, Digital isochrons of the world's ocean floor, *Journal of Geophysical Research*, 102, 3211–3214, 1997.

- Mutter, C. Z., and J. C. Mutter, Variations in thickness of layer 3 dominate oceanic crustal structure, *Earth and Planetary Science Letters*, 117, 295–317, 1993.
- Nakanishi, A., A. J. Smith, S. Miura, T. Tsuru, S. Kodaira, K. Obana, N. Takahashi, P. R. Cummins, and Y. Kaneda, Structural factors controlling the coseismic rupture zone of the 1973 Nemuro-Oki earthquake, the southern Kuril Trench seismogenic zone, *Journal of Geophysical Research*, 109, 2004.
- Obana, K., S. Kodaira, Y. Kaneda, K. Mochizuki, M. Shinohara, and K. Suyehiro, Microseismicity at the seaward updip limit of the western Nankai Trough seismogenic zone, *Journal of Geophysical Research*, 108, 2003.
- Oleskevich, D., R. Hyndman, and K. Wang, The updip and downdip limits to great subduction earthquakes: Thermal and structural models of Cascadia, south Alaska, SW Japan, and Chile, *Journal of Geophysical Research*, 104, 14,965–14,991, 1999.
- Pacheco, J., L. Sykes, and C. Scholz, Nature of Seismic Coupling Along Simple Plate Boundaries of the Subduction Type, *Journal of Geophysical Research*, 98, 14,133–14,159, 1993.
- Paige, C. C., and M. A. Saunders, LSQR: An Algorithm for Sparse Linear Equations and Sparse Least Squares, *ACM Transactions on Mathematical Software*, 8, 43–71, 1982.
- Park, J., and V. Levin, Seismic Anisotropy: Tracing Plate Dynamics in the Mantle, *Science*, 296, 485–489, 2002.
- Peyrat, S., R. Madariaga, E. Buforn, J. Campos, G. Asch, and J. P. Vilotte, Kinematic rupture process of the 2007 Tocopilla earthquake and its main aftershocks from teleseismic and strong-motion data, *Geophysical Journal International*, 182, 1411–1430, 2010.
- Planert, L., Crustal Structure of the Mid-Atlantic Ridge at 5 N South: Two Contrasting Spreading Segments, Ph.D. thesis, Christian-Albrechts-Universität zu Kiel, PHD Thesis, 2006.
- Ranero, C. R., J. P. Morgan, K. McIntosh, and C. Reichert, Bending, faulting, and mantle serpentinization at the Middle America Trench, *Nature*, 425, 367–373, 2003.
- Ranero, C. R., A. Villaseñor, J. P. Morgan, and W. Weinrebe, Relationship between bend-faulting at trenches and intermediate-depth seismicity, *Geochemistry, Geophysics and Geosystems*, 6, 2005.

- 
- Ruegg, J. C., A. Rudloff, C. Vigny, R. Madariaga, J. de Chabali er, J. Campos, E. Kausel, S. Barrientos, and D. Dimitrov, Interseismic strain accumulation measured by GPS in the seismic gap between Constituci on and Concepci on in Chile, *Physics of the Earth and Planetary Interiors*, 175, 78–85, 2009.
- Sallar es, V., and C. R. Ranero, Structure and tectonics of the erosional convergent margin off Antofagasta, north Chile ( $23^{\circ}30'S$ ), *Journal of Geophysical Research*, 110, 2005.
- Satake, K., and Y. Tanioka, Sources of Tsunami and Tsunamigenic Earthquakes in Subduction Zones, *Pure Appl. Geophys.*, 154, 467–483, 1999.
- Scherwath, M., E. Contreras-Reyes, E. R. Flueh, I. Grevemeyer, A. Krabbenhoef, C. Papenberg, C. J. Petersen, and R. W. Weinrebe, Deep lithospheric structures along the southern central Chile margin from wide-angle P-wave modelling, *Geophysical Journal International*, 179, 579–600, 2009.
- Scholz, C., *The Mechanics of Earthquakes and Faulting*, 2nd ed., Cambridge University Press, Cambridge, 2002.
- Shaw, P. R., and J. A. Orcutt, Waveform inversion of seismic refraction data and applications to young pacific crust, *Geophys. J. R. Astron. Soc.*, 1985.
- Shearer, P. M., and J. A. Orcutt, Compressional and shear wave anisotropy in the oceanic lithosphere - the Ngendei seismic refraction experiment, *Geophys. J. R. astr. Soc.*, 87, 967–1003, 1986.
- Siegesmund, S., T. Takeshita, and H. Kern, Anisotropy of  $V_p$  and  $V_s$  in an amphibolite of the deeper crust and its relationship to the mineralogical, microstructural, and textural characteristics of the rock, *Tectonophysics*, 157, 25–38, 1989.
- Spudich, P., and J. Orcutt, Petrology and porosity of an oceanic crust site: results from waveform modeling of seismic refraction data, *Journal of Geophysical Research*, 85, 1409–1433, 1980.
- Stern, R. J., Subduction zones, *Reviews of Geophysics*, 40, 1012, 2002.
- Tarantola, A., *Inverse Problem Theory: Methods for Data Fitting and Model Parameter Estimation*, Elsevier, New York, 1987.

- Tatsumi, Y., and R. J. Stern, Manufacturing Continental Crust in the Subduction Factory: Was Continent Born in the Ocean?, *Oceanography*, 17, 104–112, 2006.
- Tebbens, S., S. Cande, L. Kovacs, J. Parra, J. LaBrecque, and H. Vergara, The Chile ridge: A tectonic framework, *Journal of Geophysical Research*, 102, 12,035–12,059, 1997.
- Thornburg, T., D. M. Kulm, and D. Hussong, Submarine-fan development in the southern Chile trench: a dynamic interplay of tectonics and sedimentation, *Geological Society of America Bulletin*, 102, 1658–1680, 1990.
- Thornburg, T. M., and D. M. Kulm, Sedimentation in the Chile Trench: Depositional morphologies, lithofacies, and stratigraphy, *Geological Society of America Bulletin*, 98, 33–52, 1987.
- Tichelaar, B., and L. Ruff, Seismic Coupling Along the Chilean Subduction Zone, *Journal of Geophysical Research*, 96, 11,997–12,022, 1991.
- Tichelaar, B., and L. Ruff, Depth of Seismic Coupling Along Subduction Zones, *Journal of Geophysical Research*, 98, 2017–2037, 1993.
- Tieman, H. J., Investigating the velocity-depth ambiguity of reflection traveltimes, *Geophysics*, 1994.
- Tilman, F. J., I. Grevemeyer, E. Flueh, T. Dahm, and J. Gossler, Seismicity in the outer rise offshore southern Chile: Indication of fluid effects in crust and mantle, *Earth and Planetary Science Letters*, 269, 41–55, 2008.
- Tong, X., et al., The 2010 Maule, Chile earthquake: Downdip rupture limit revealed by space geodesy, *Geophysical Research Letters*, 37, 2010.
- Toomey, D., and G. Foulger, Tomographic Inversion of Local Earthquake Data From the Hengill-Grensdalur Central Volcano Complex, Iceland, *Journal of Geophysical Research*, 94, 17,497–17,510, 1989.
- Vera, E., J. Mutter, P. Buhl, J. Orcutt, A. Harding, M. Kappus, R. Detrick, and T. Brocher, The Structure of 0- to 0.2-m.y.-Old Oceanic Crust at 9°N on the East Pacific Rise From Expanded Spread Profiles, *Journal of Geophysical Research*, 95, 15,529–15,556, 1990.
- Verma, R., Elasticity of Some High-Density Crystals, *Journal of Geophysical Research*, 65, 757–766, 1960.

---

Völker, D., M. Wiedicke, C. Gaedeke, S. Ladage, C. Reichert, K. Rauch, W. Kramer, and C. Heubeck, *Latitudinal Variation in Sedimentary Processes in the Peru-Chile Trench off Central Chile.*, Springer, 2006.

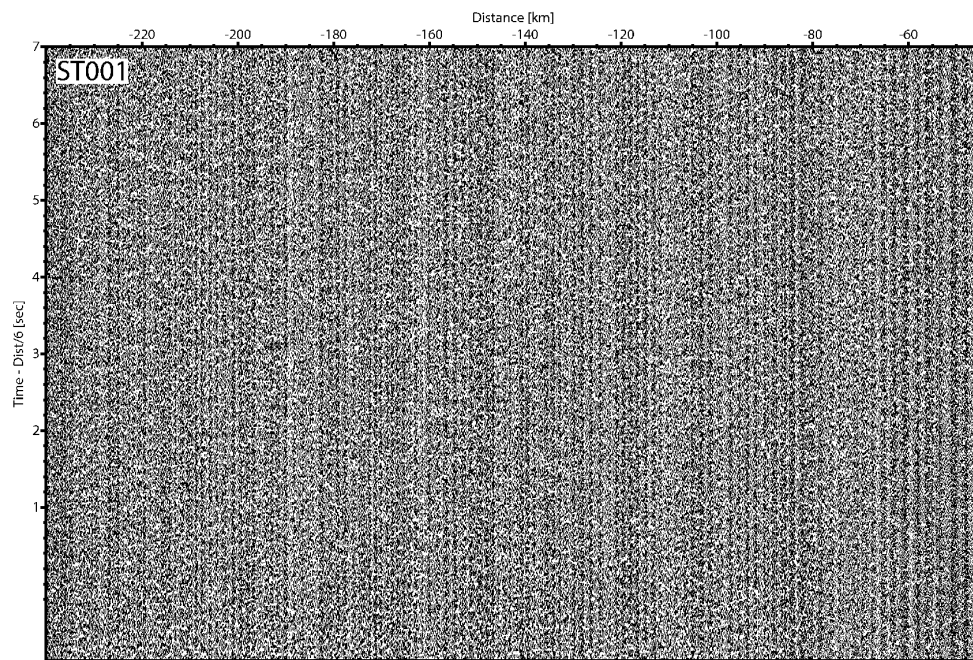
Zelt, C. A., K. Sain, J. V. Naumenko, and D. S. Sawyer, Assessment of crustal velocity models using seismic refraction and reflection tomography, *Geophysical Journal International*, 153, 609–626, 2003.

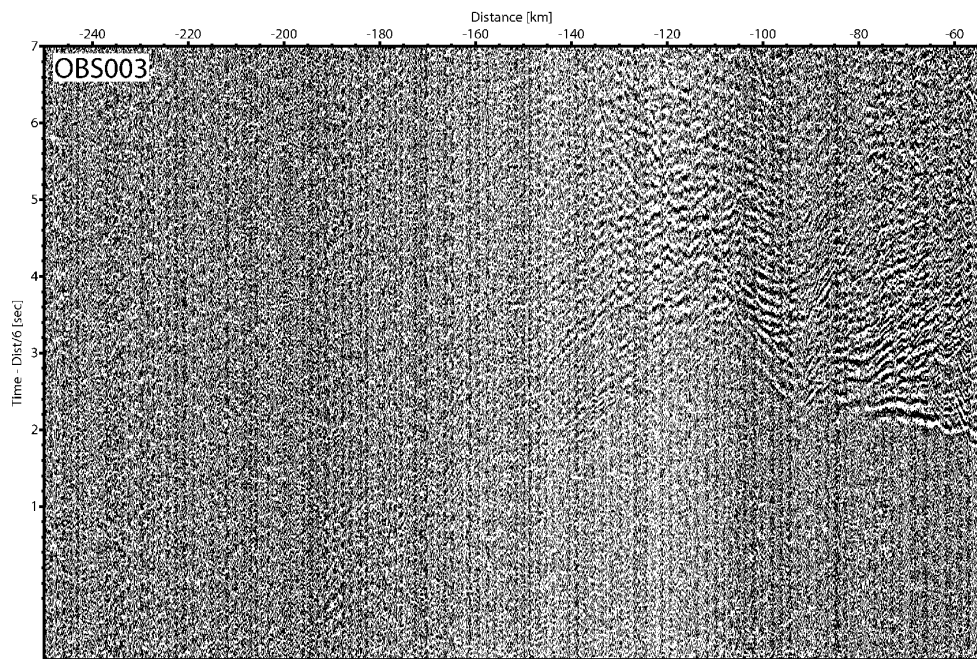
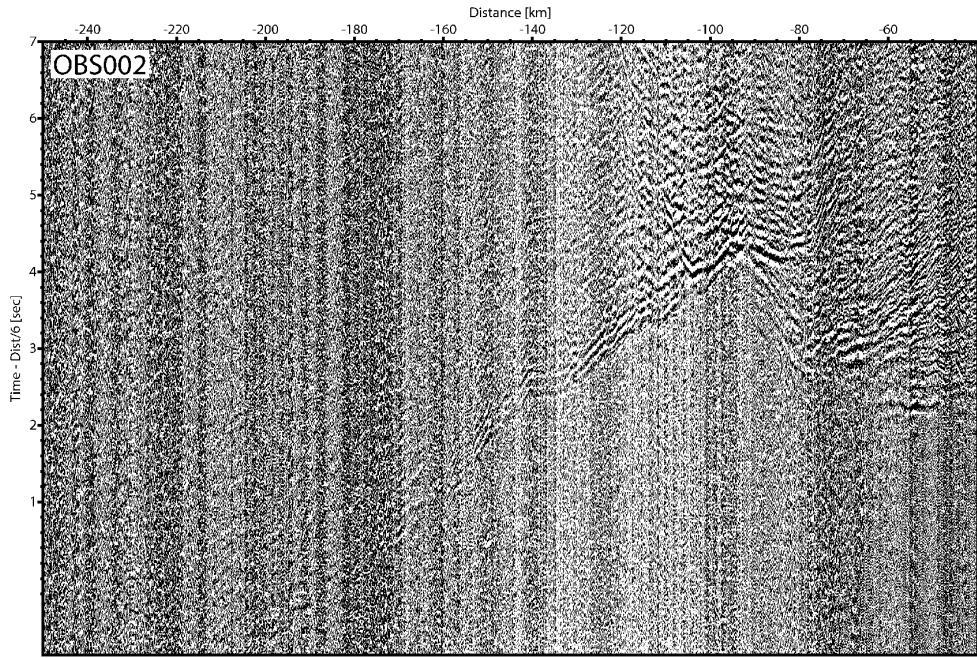
Zhang, S., and S. Karato, Lattice preferred orientation of olivine aggregates deformed in simple shear, *Nature*, 375, 774–777, 1995.



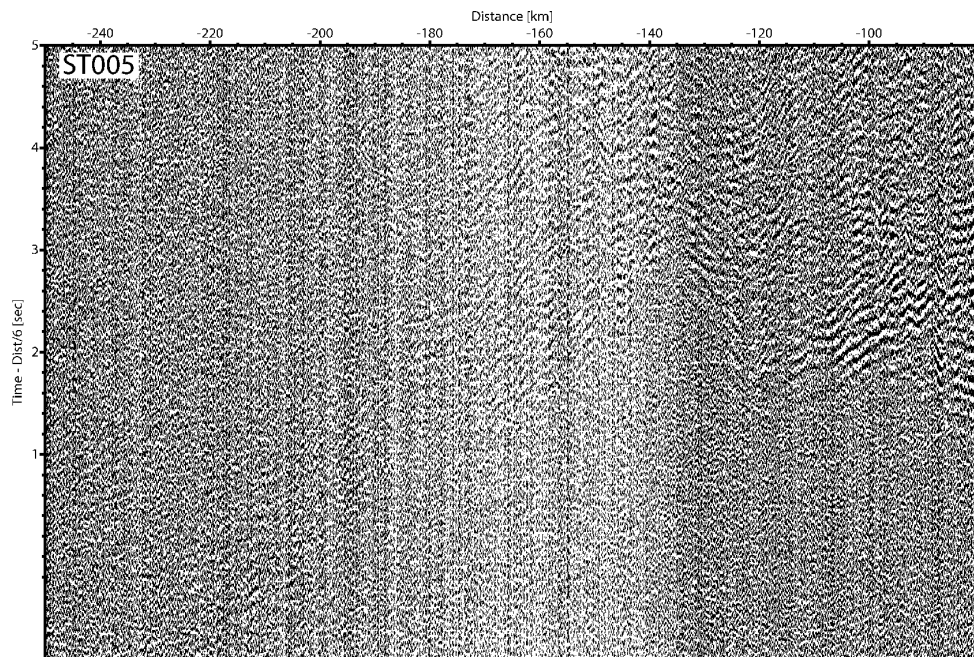
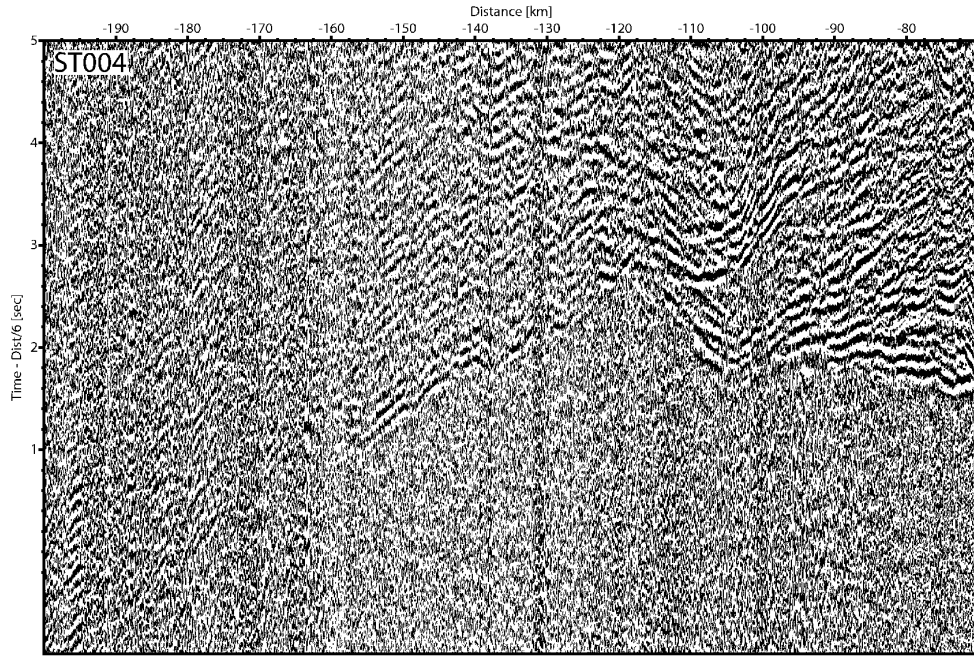
# Appendix A

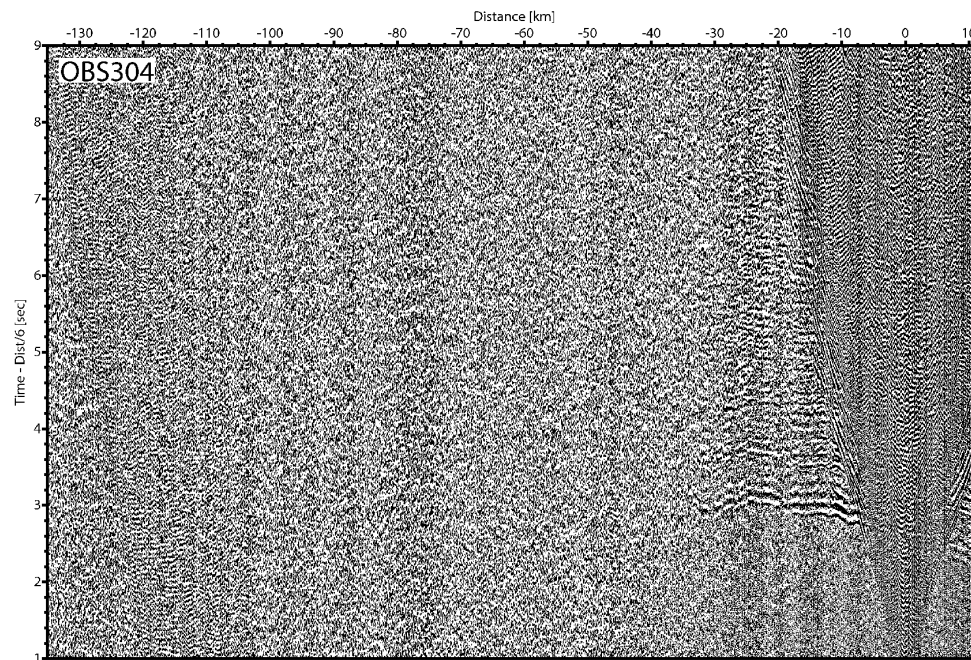
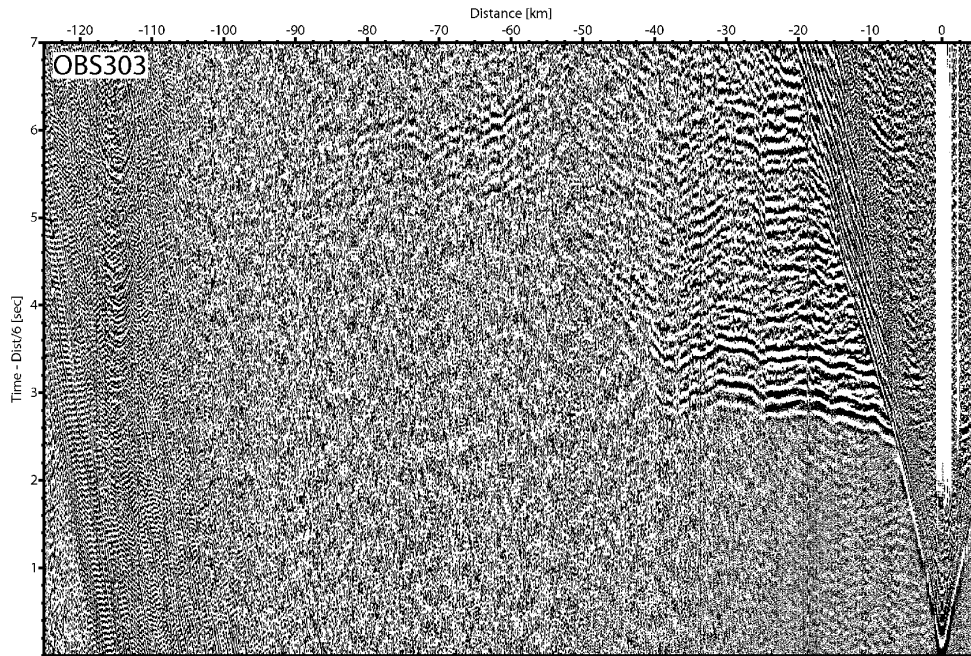
## Seismic sections





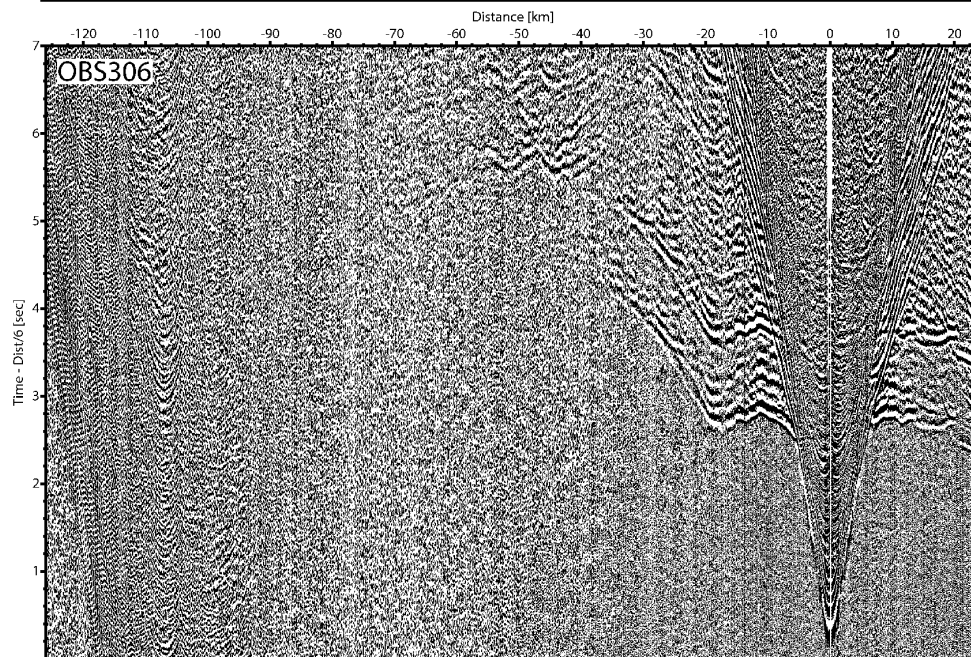
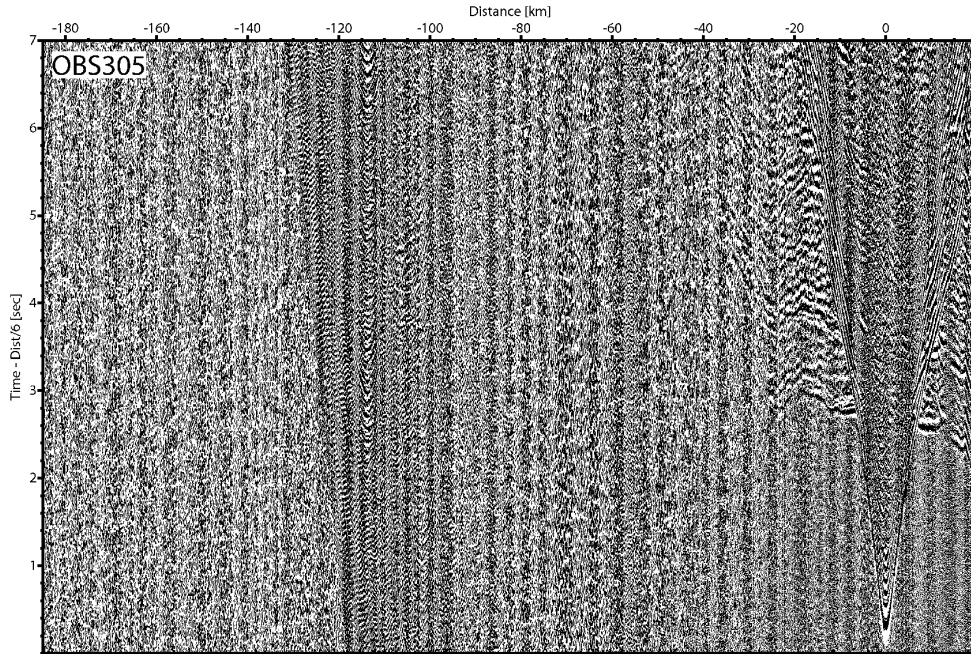
APPENDIX A. SEISMIC SECTIONS

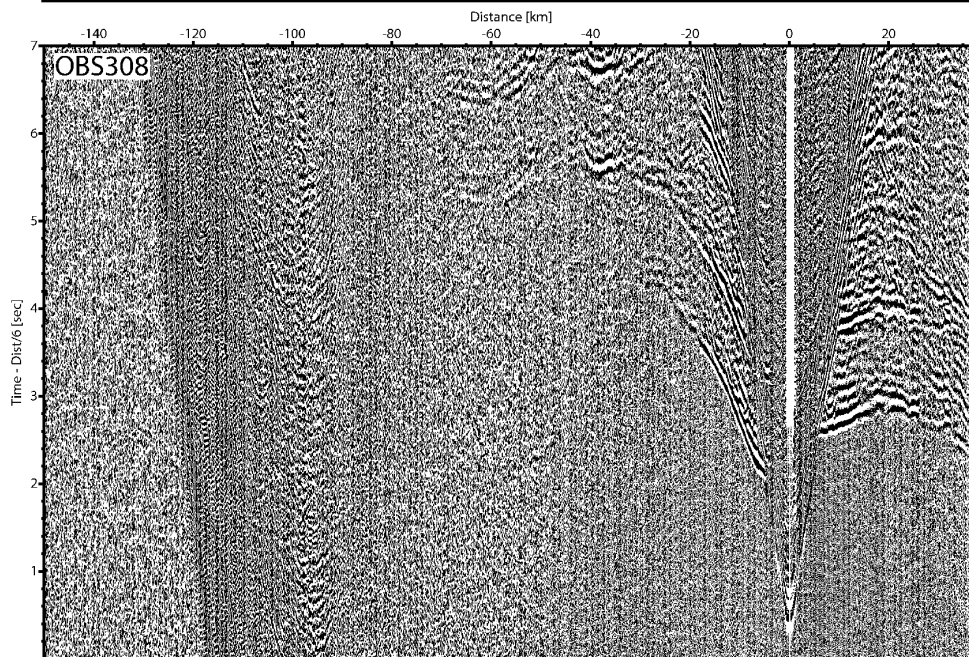
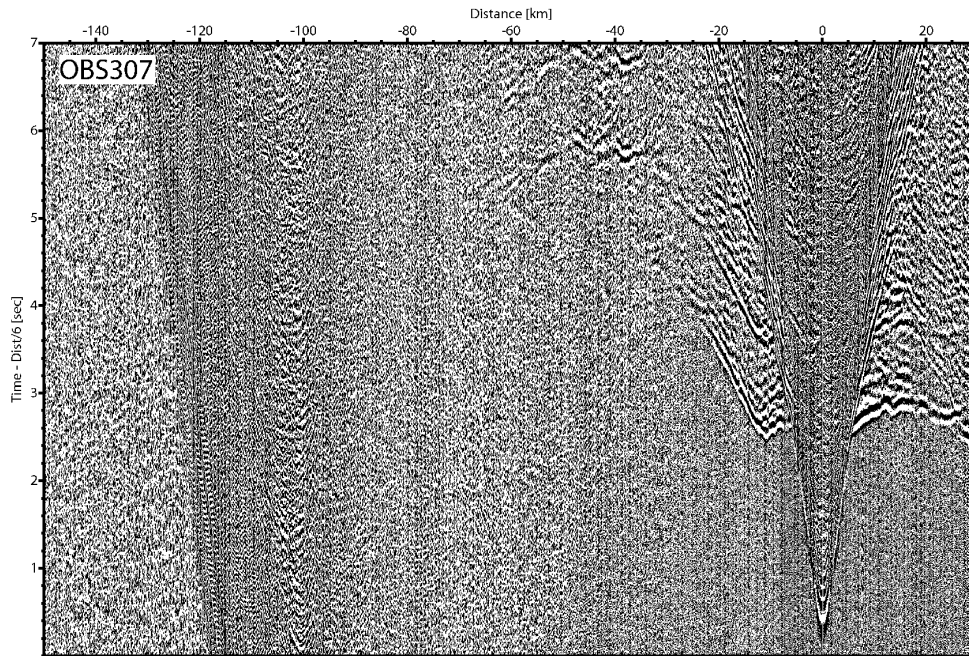




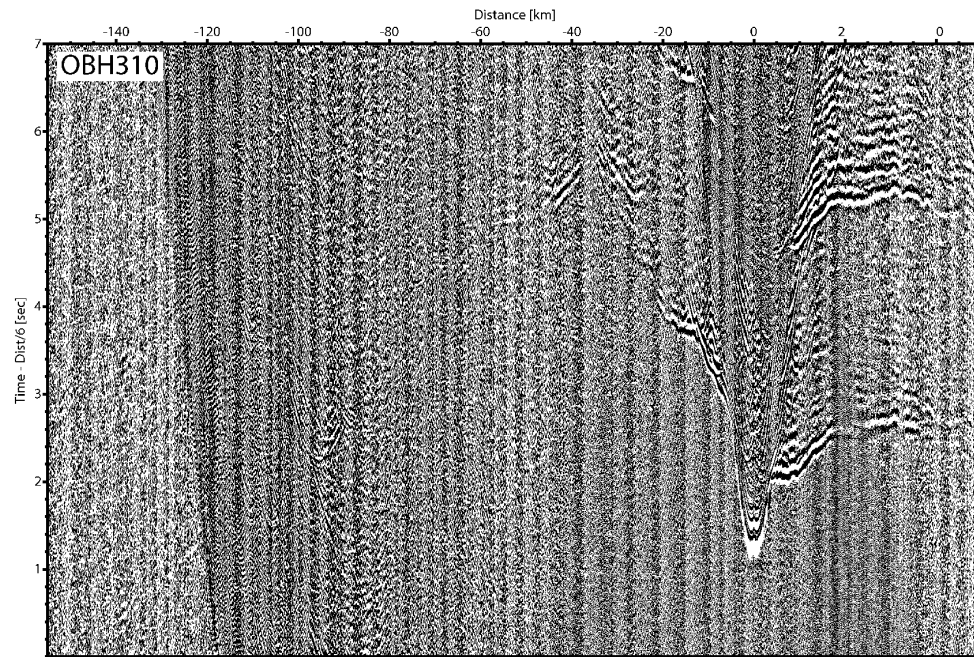
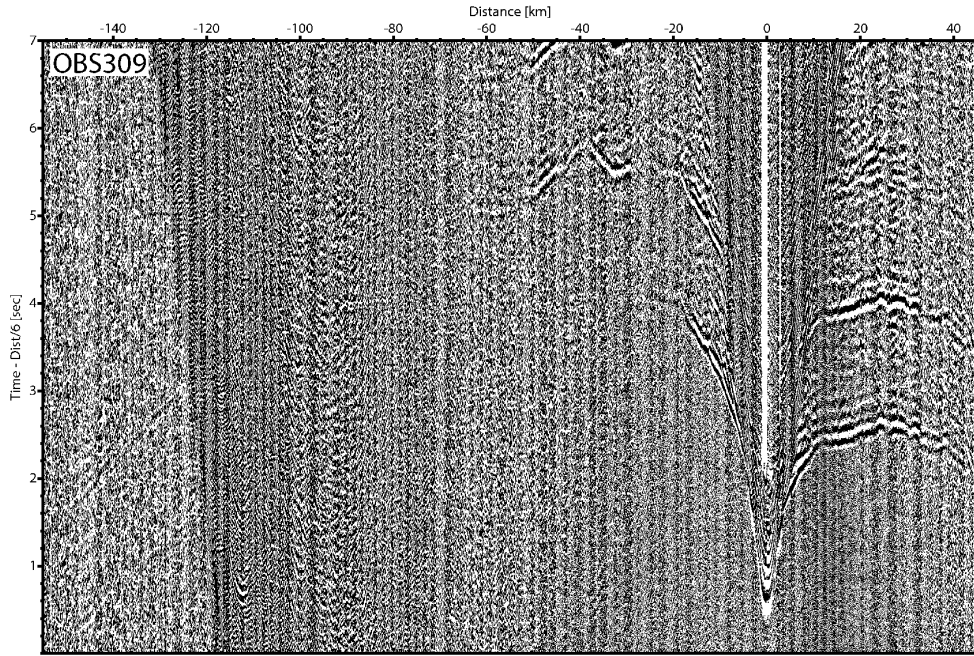


APPENDIX A. SEISMIC SECTIONS

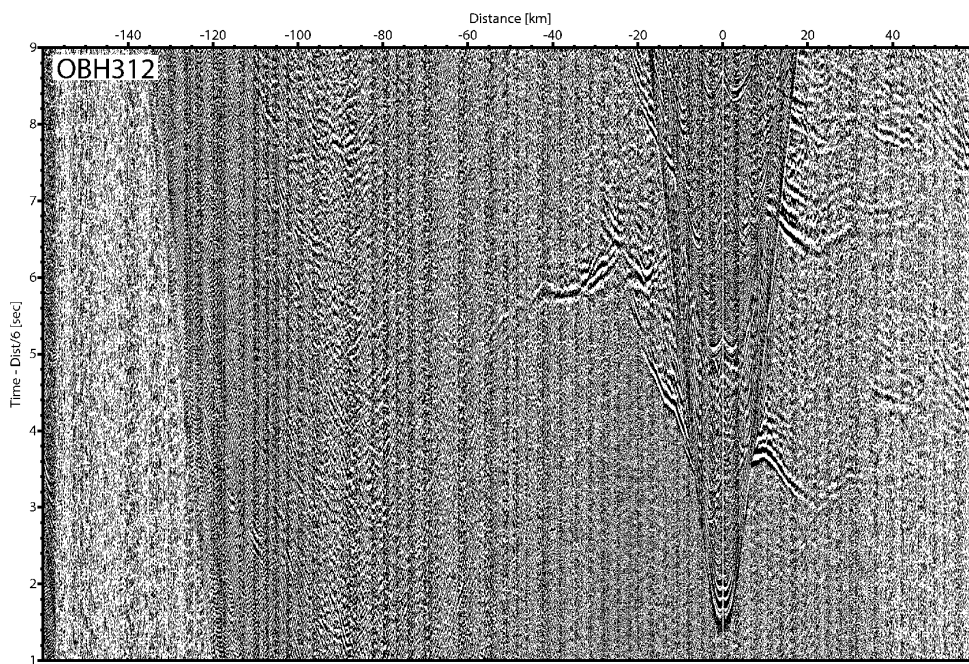
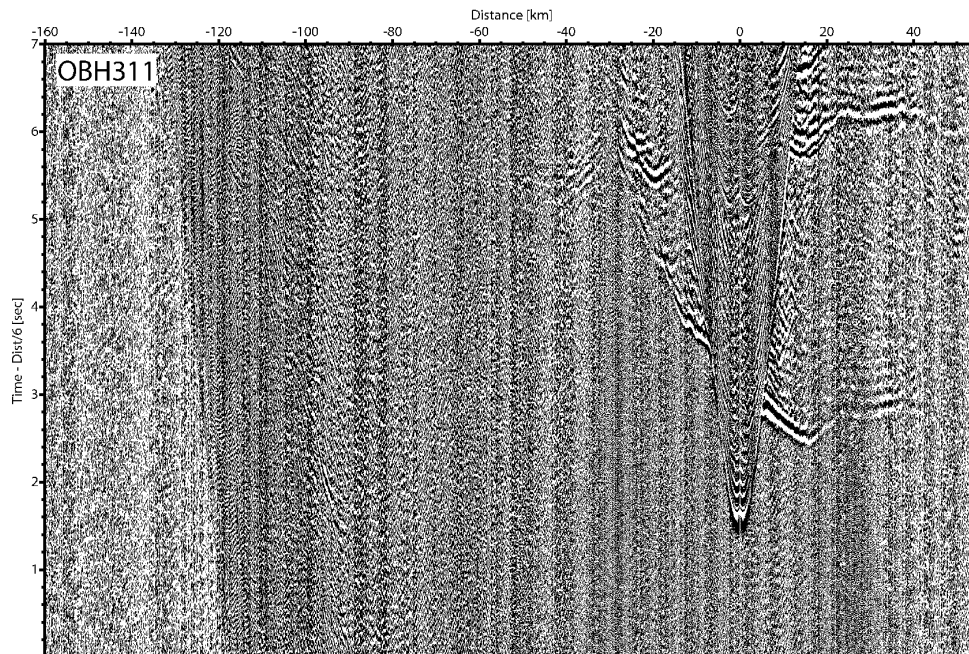




APPENDIX A. SEISMIC SECTIONS

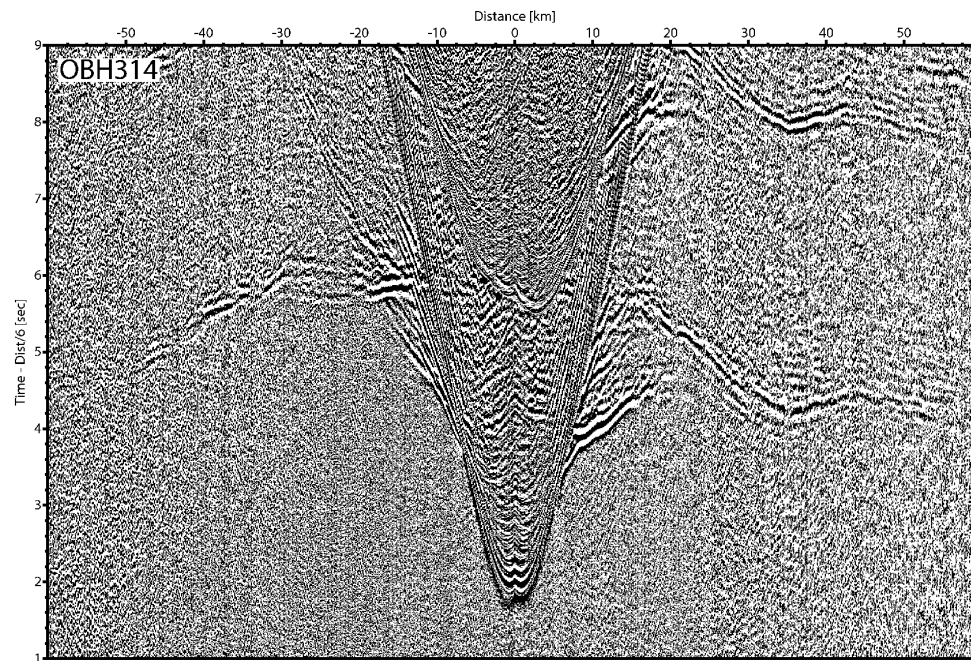
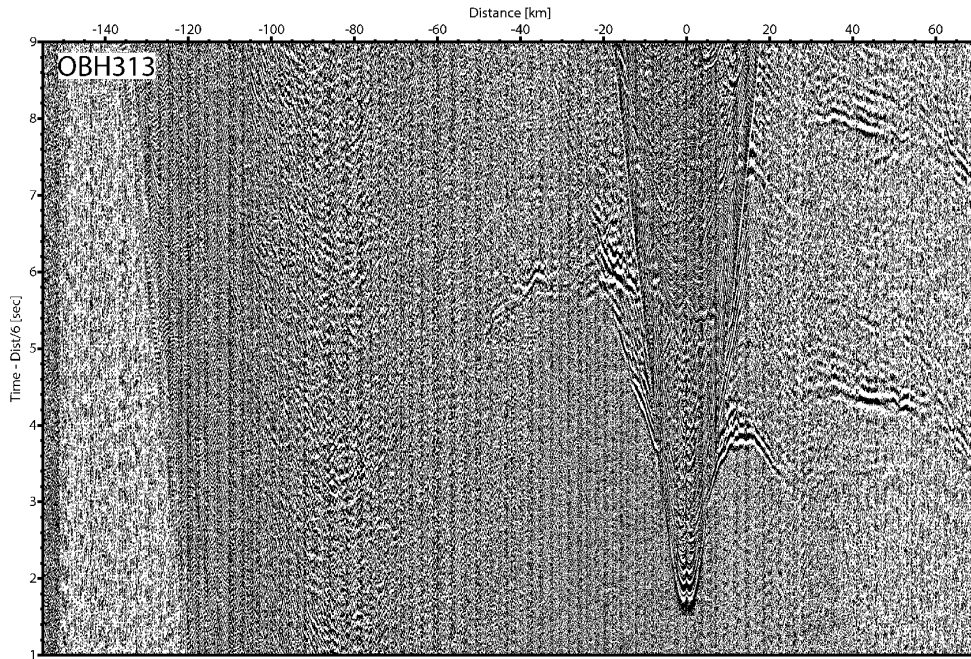


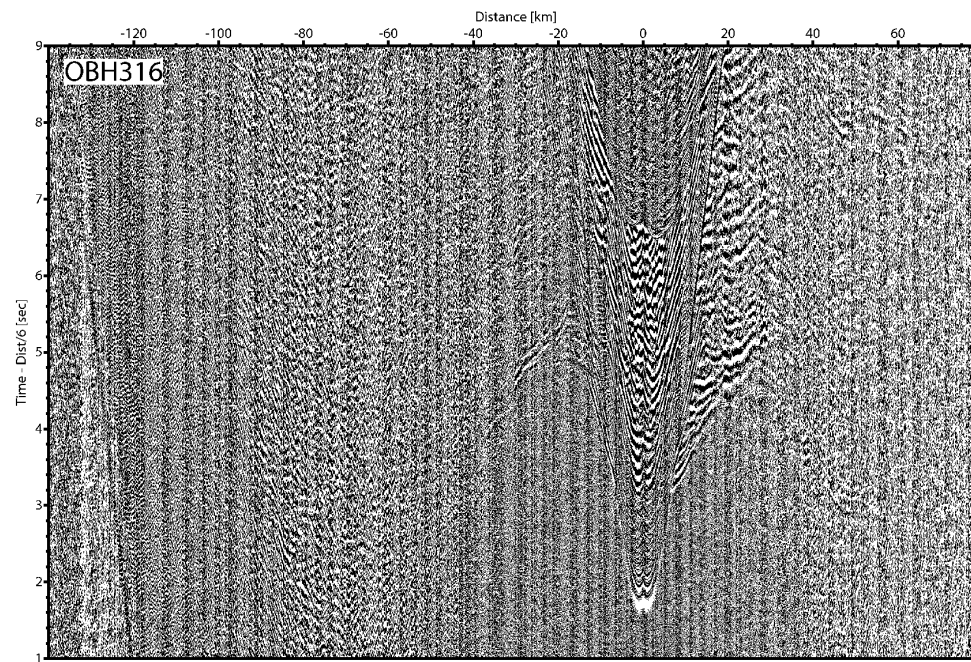
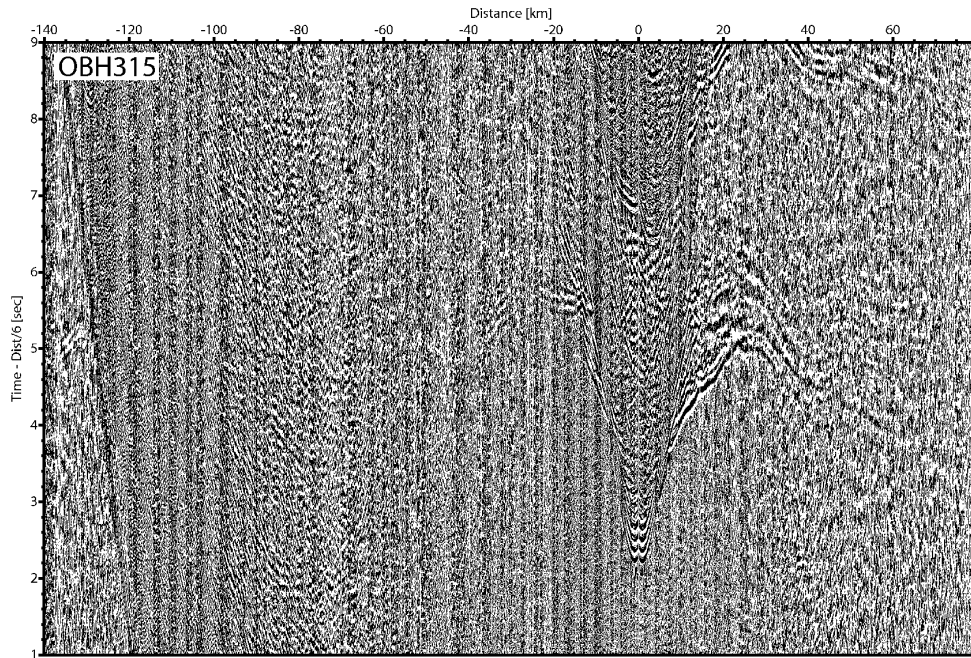




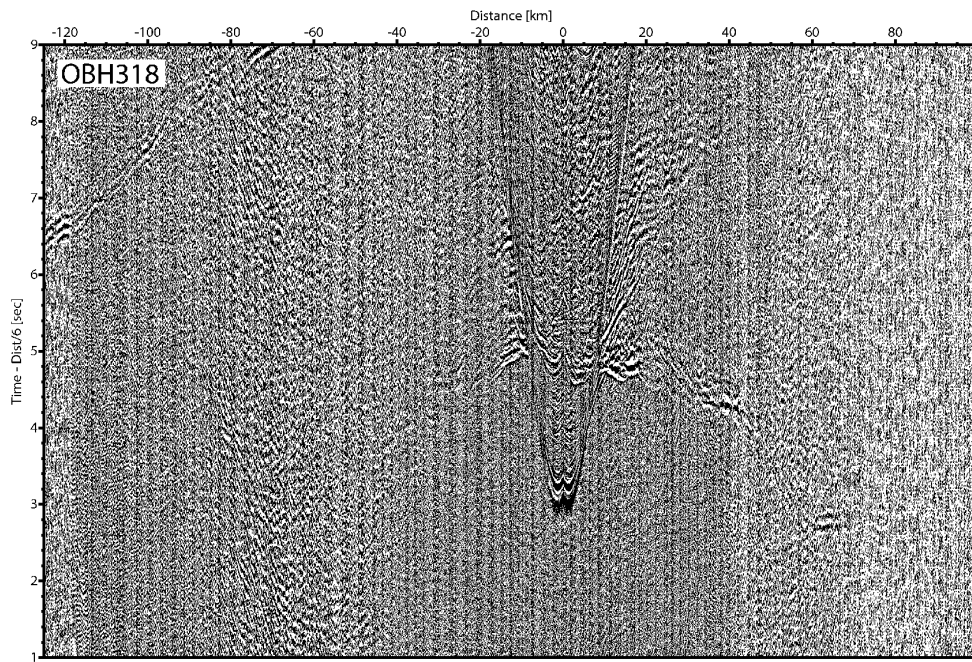
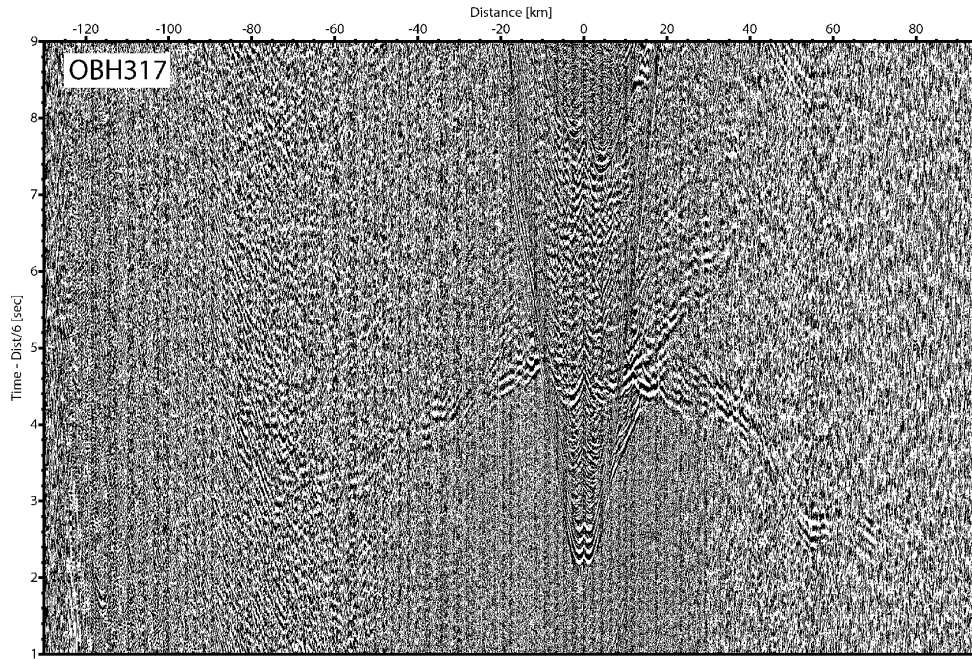


APPENDIX A. SEISMIC SECTIONS

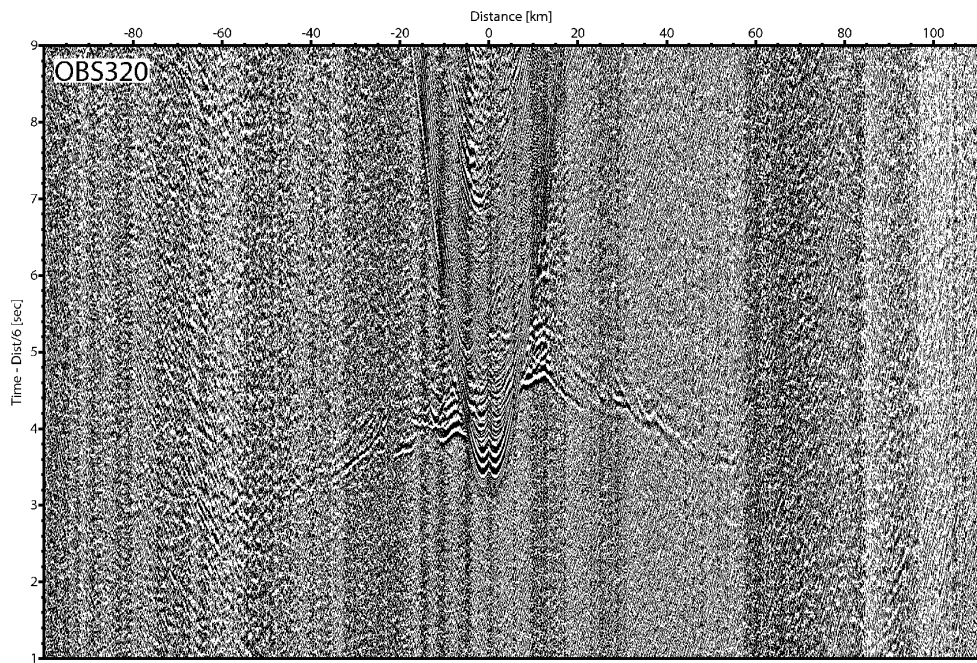
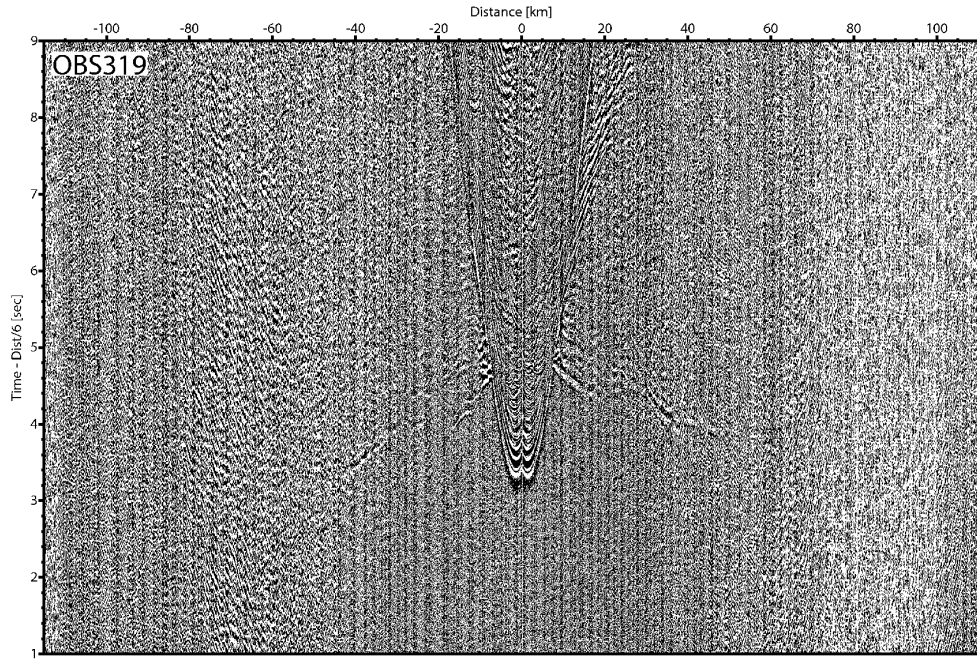




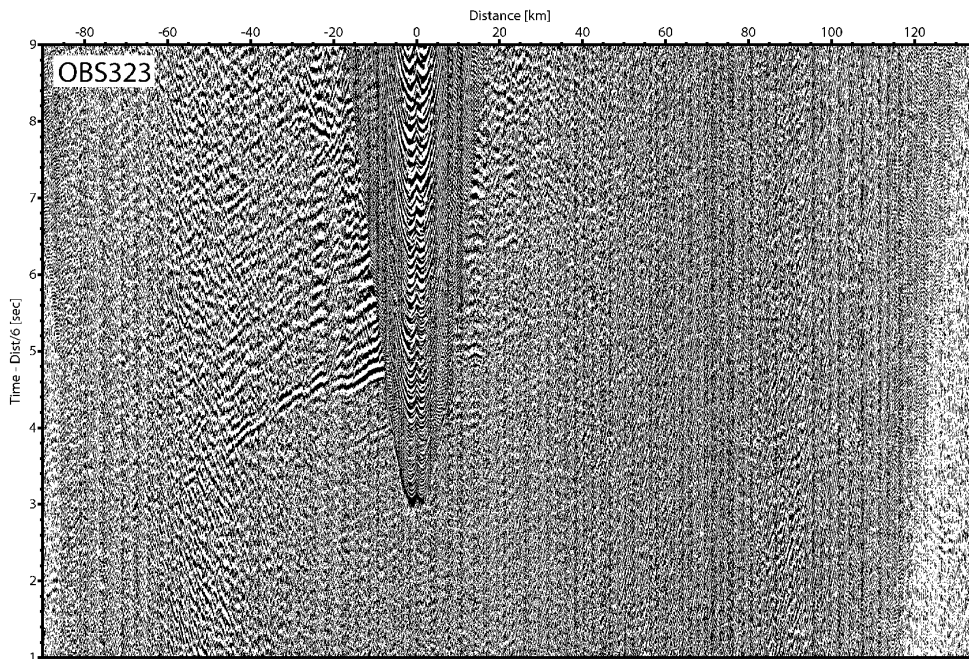
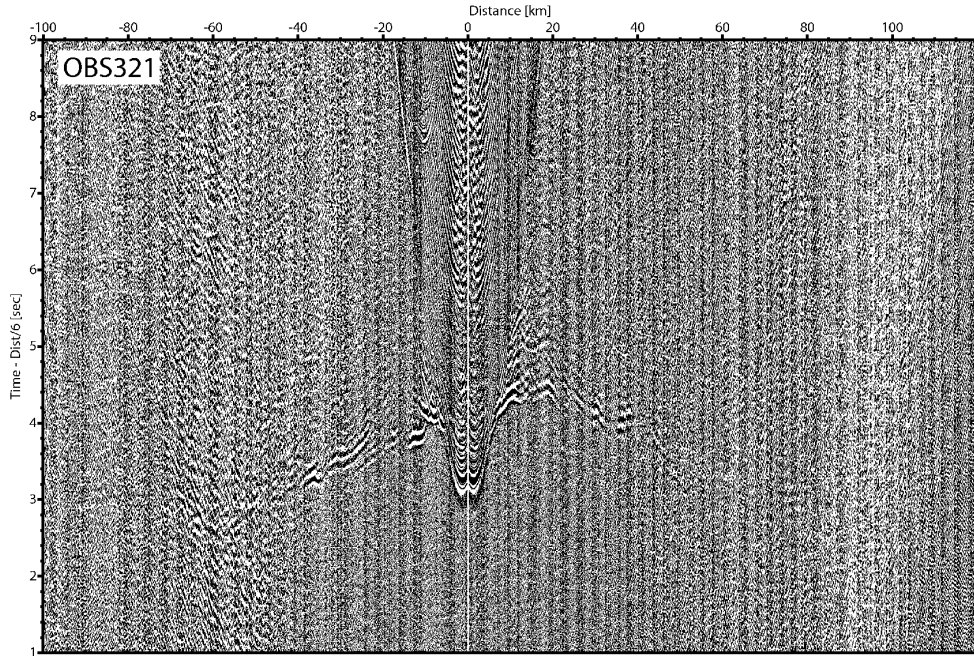
APPENDIX A. SEISMIC SECTIONS

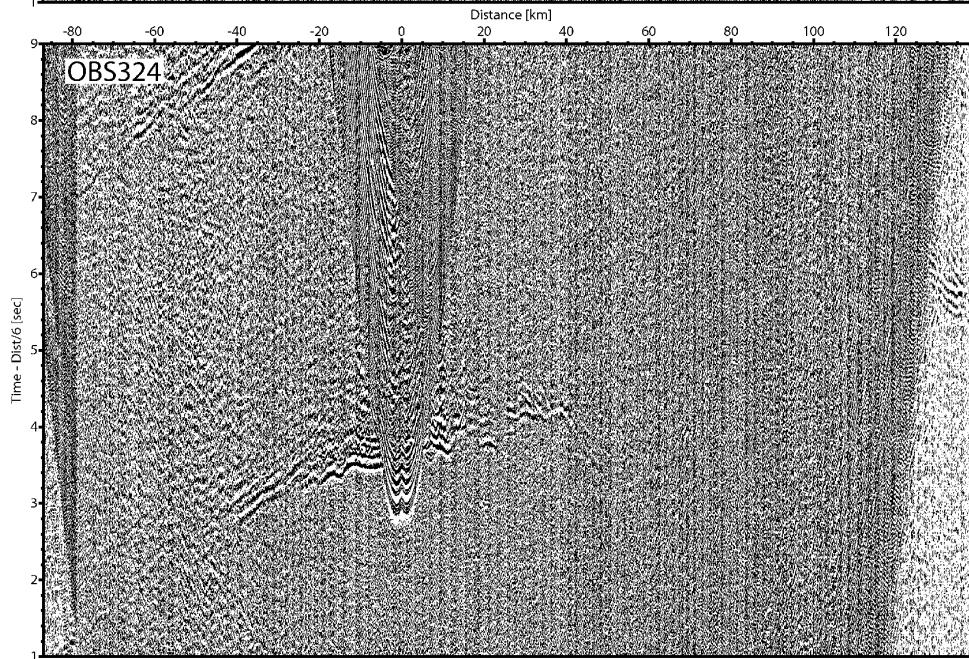
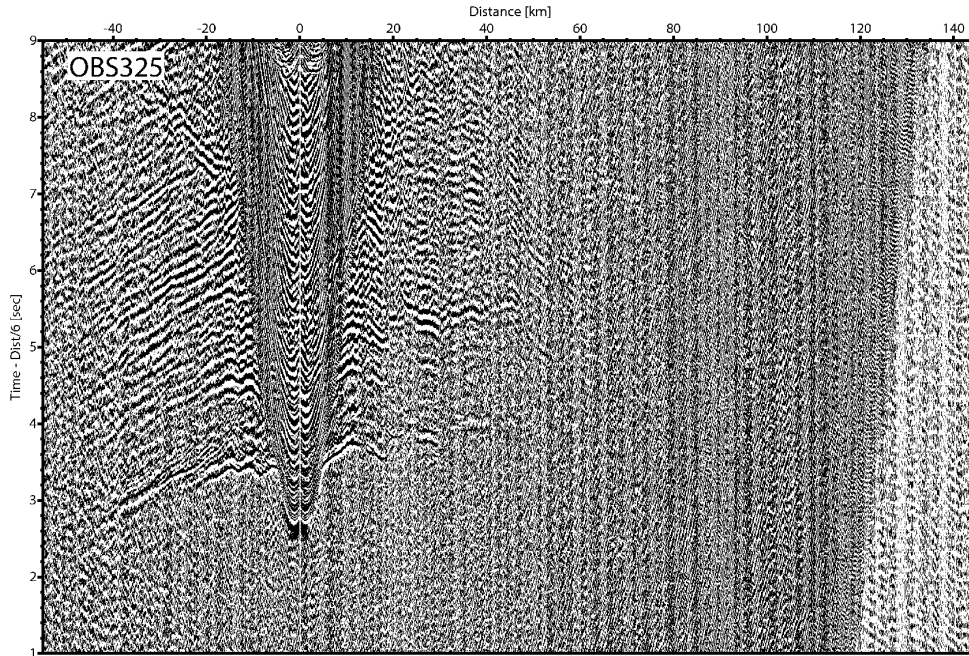






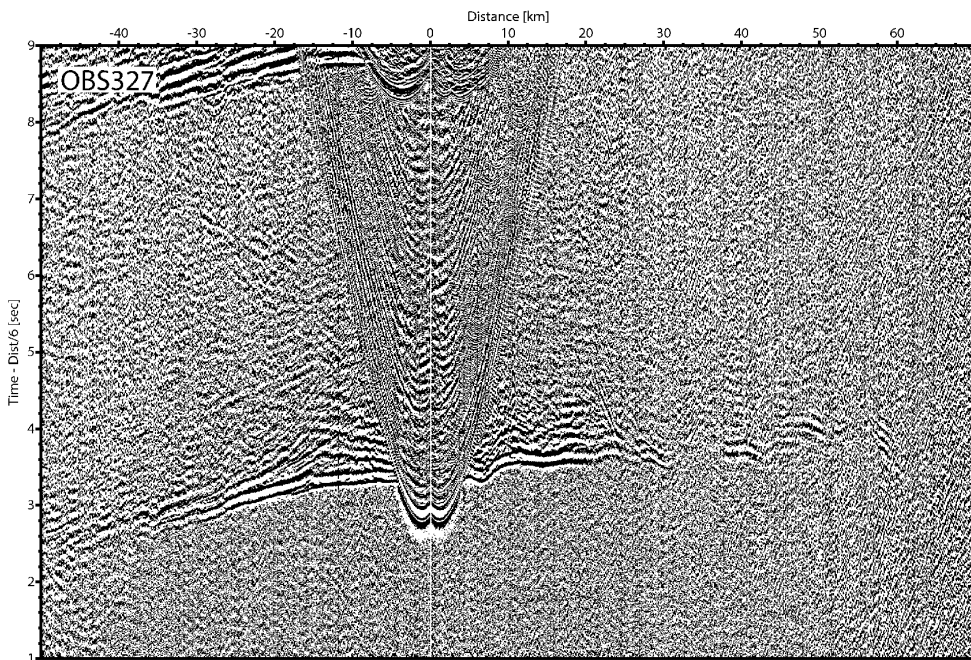
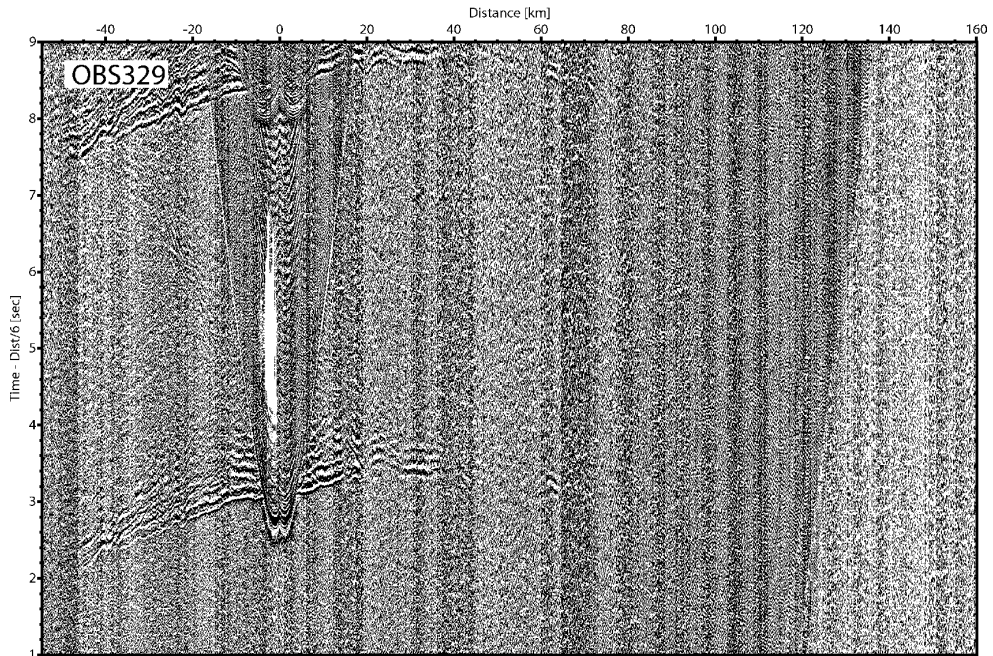
APPENDIX A. SEISMIC SECTIONS

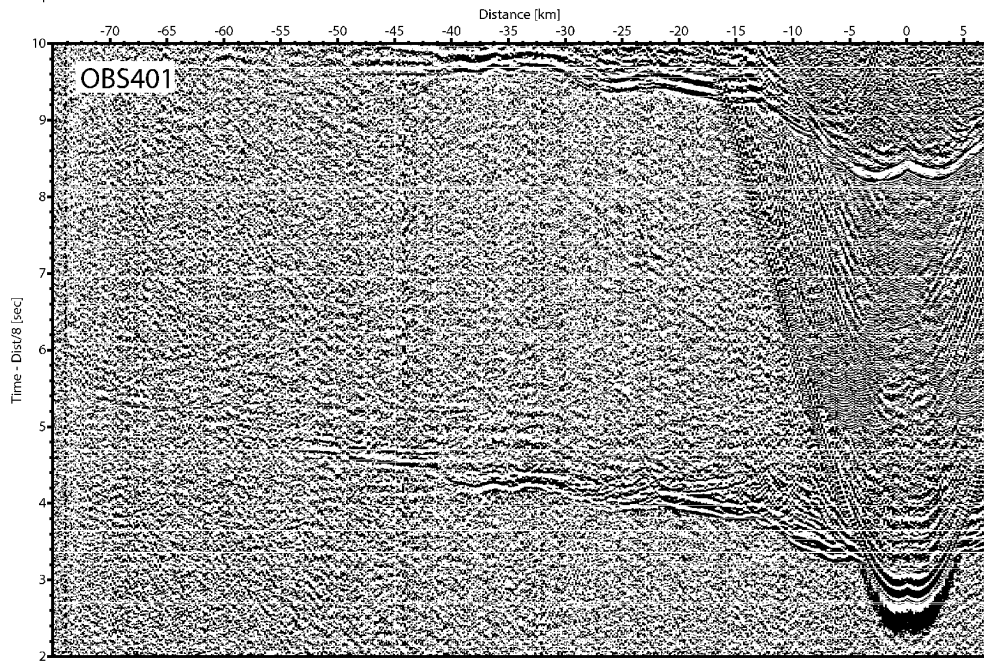
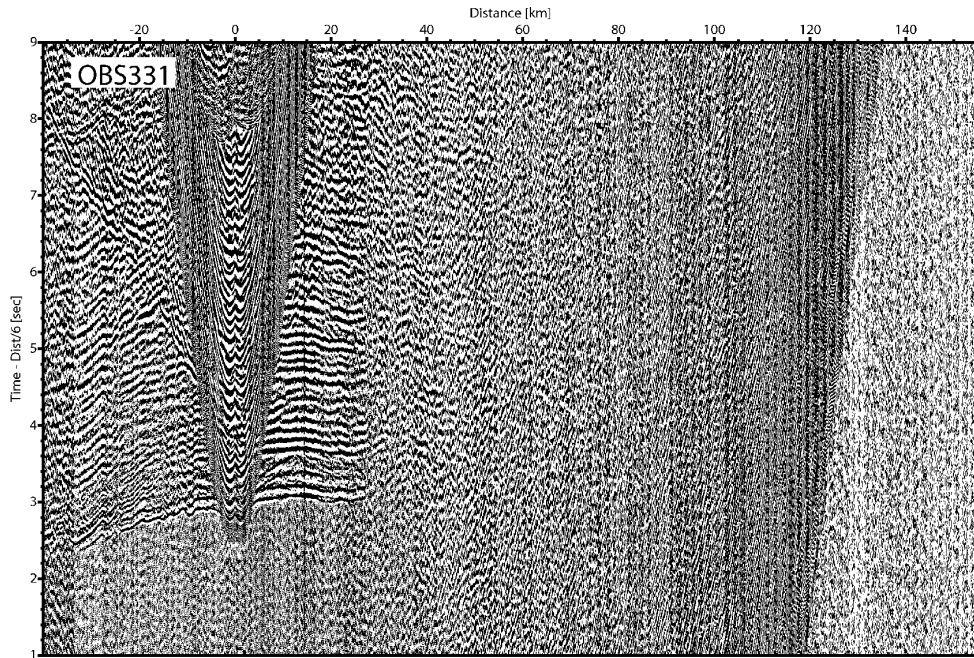






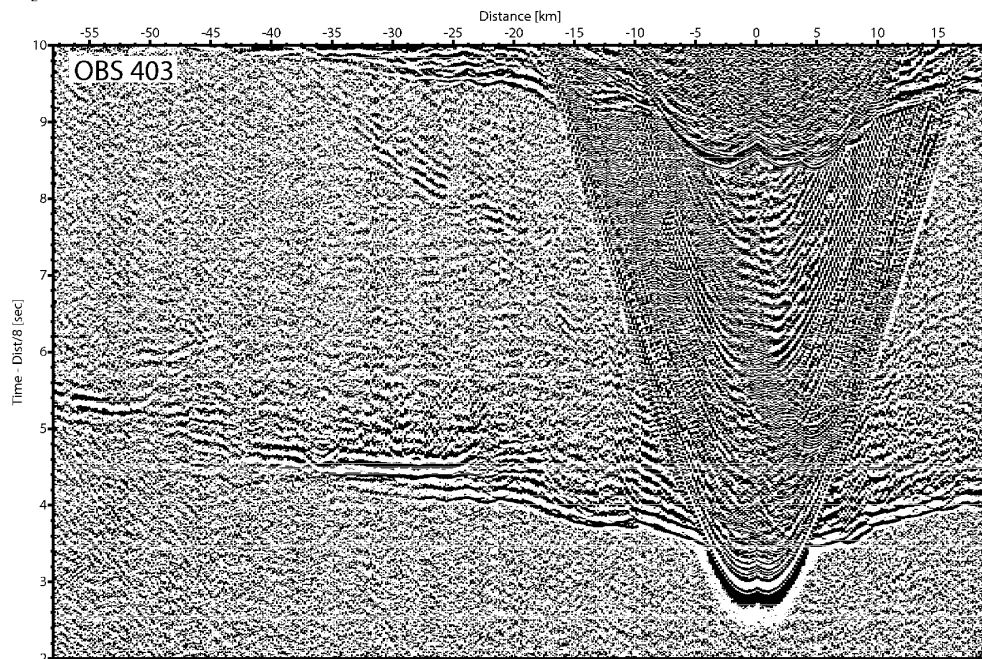
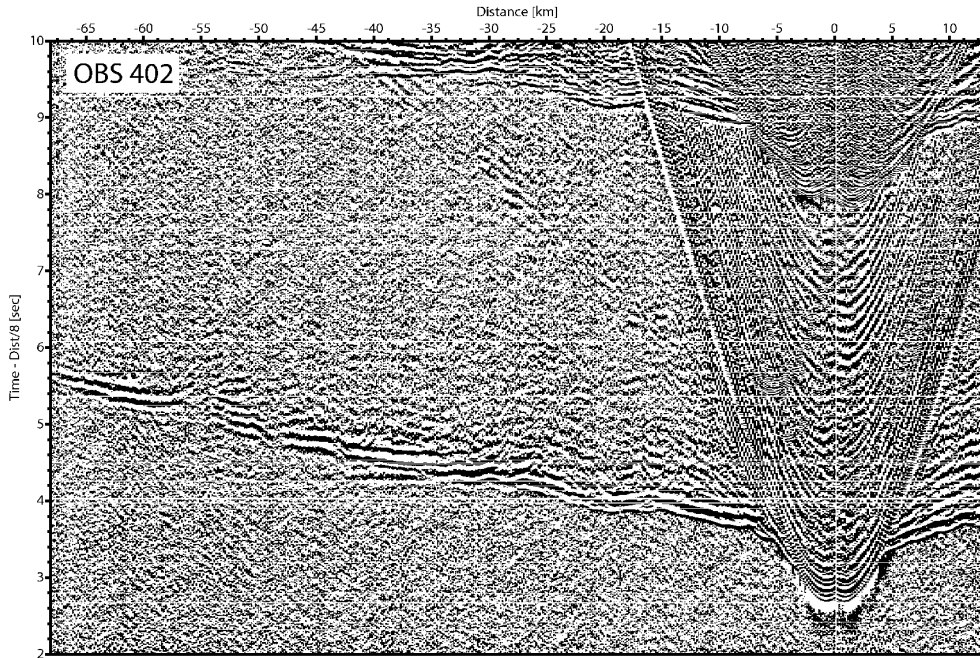
APPENDIX A. SEISMIC SECTIONS

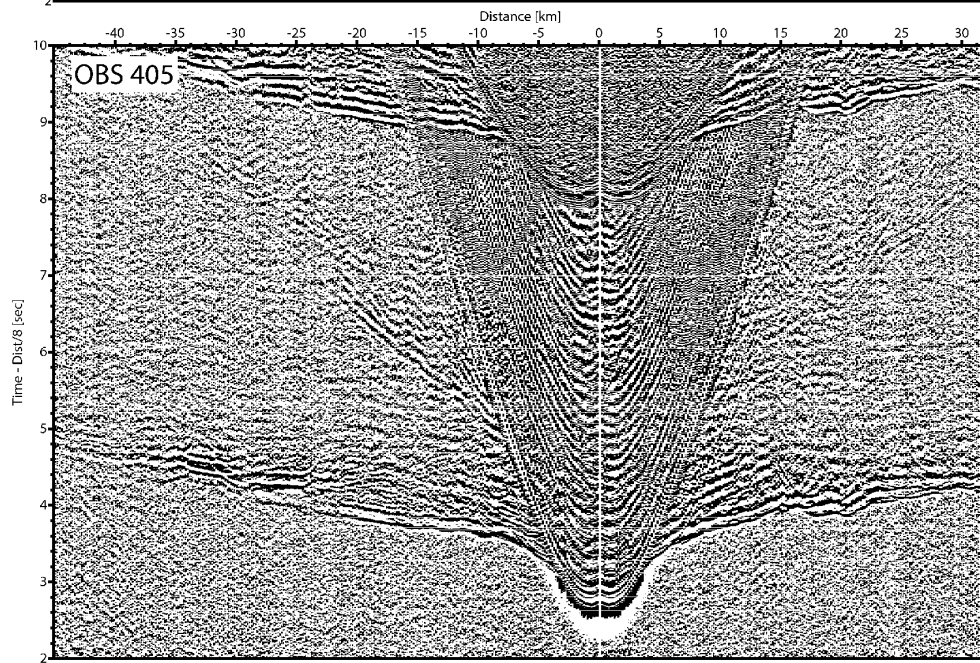
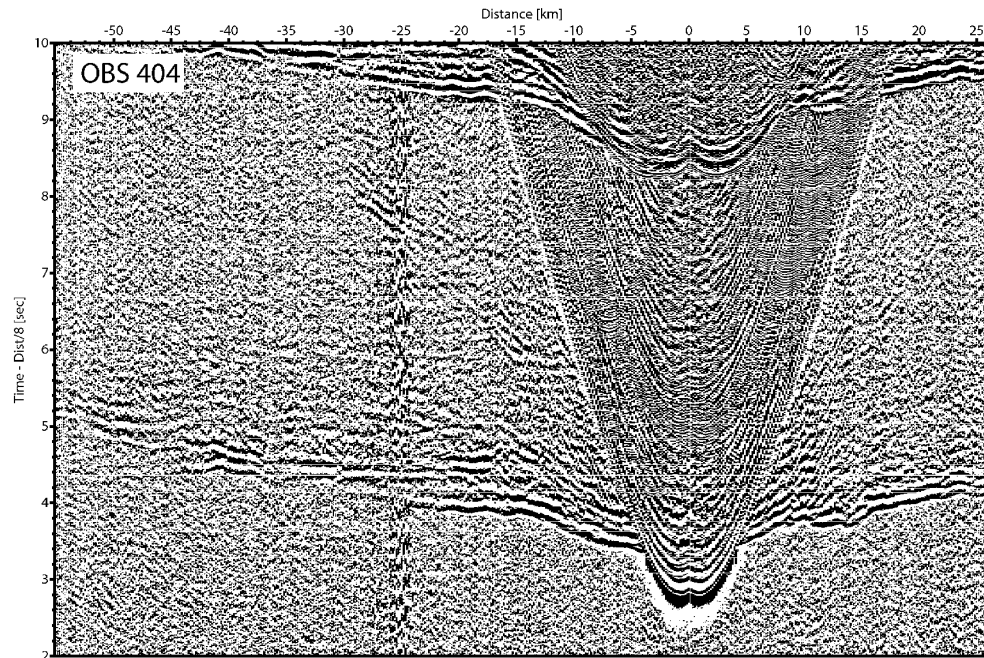


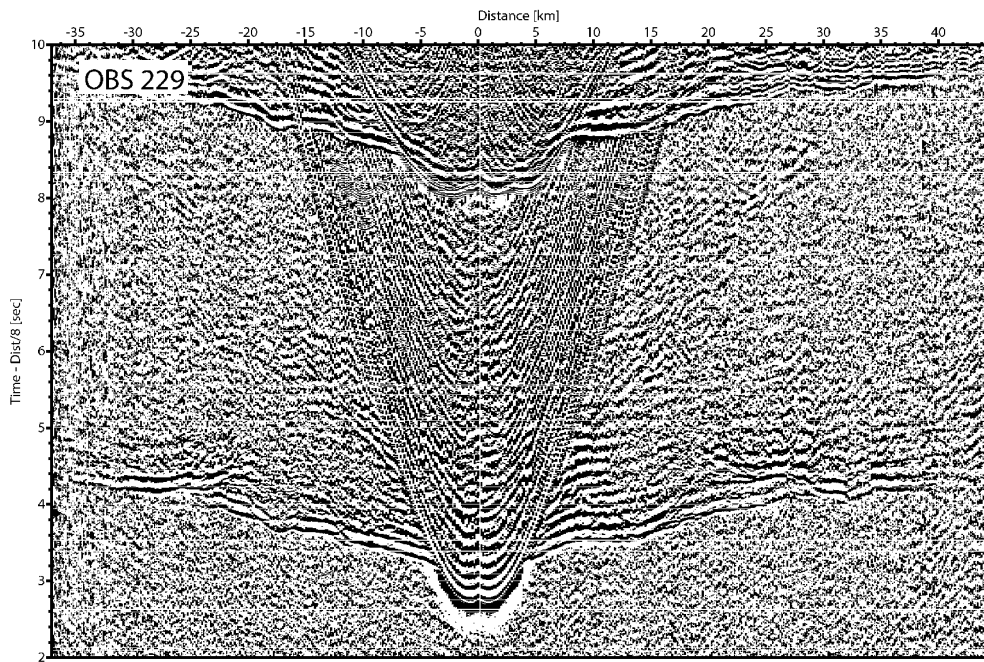
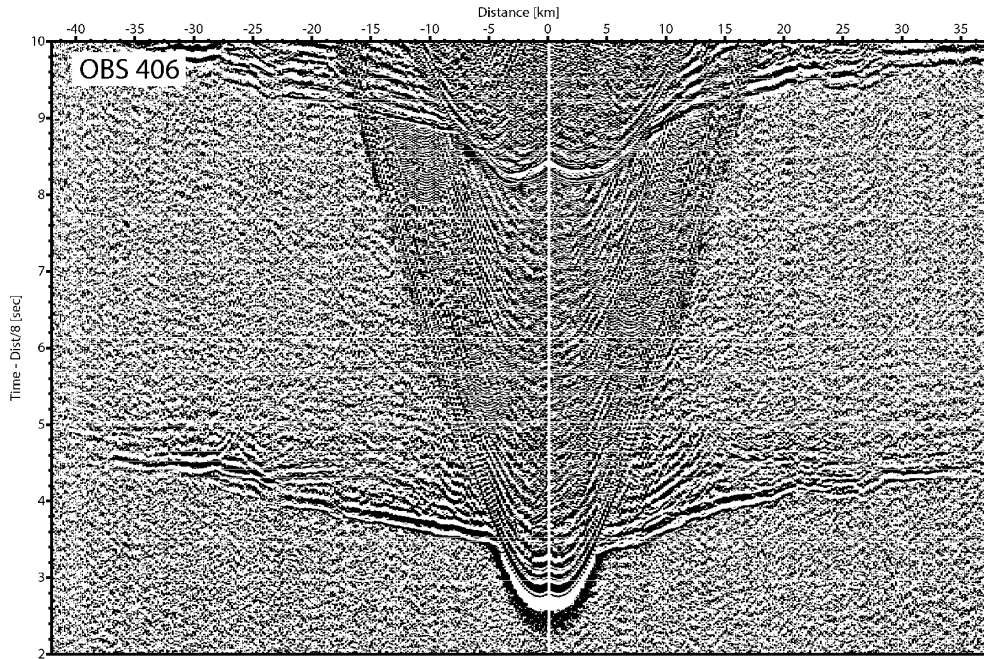


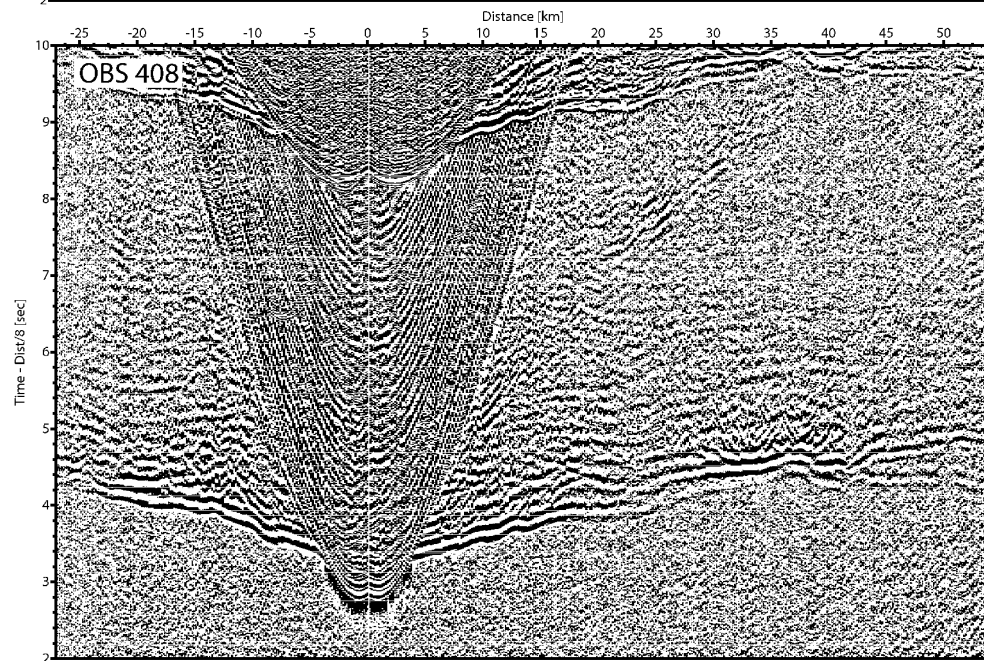
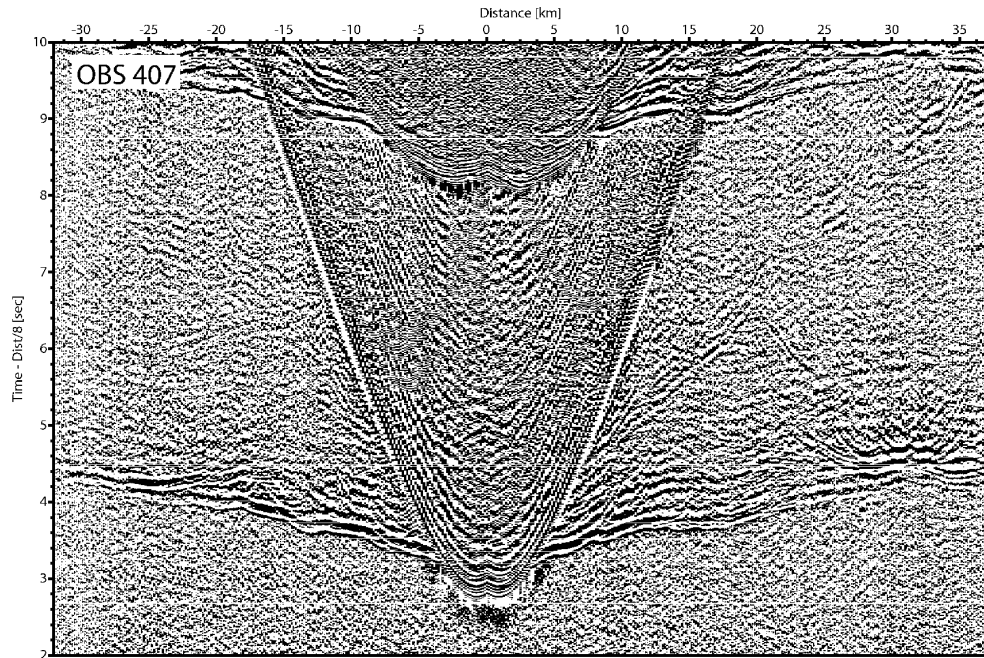


APPENDIX A. SEISMIC SECTIONS



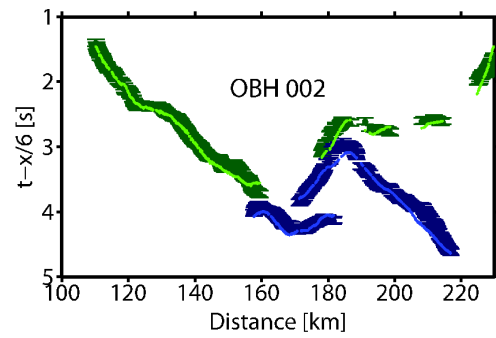
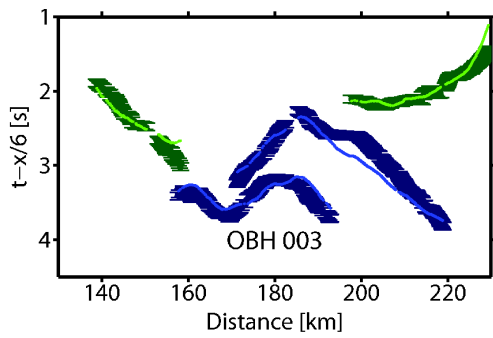
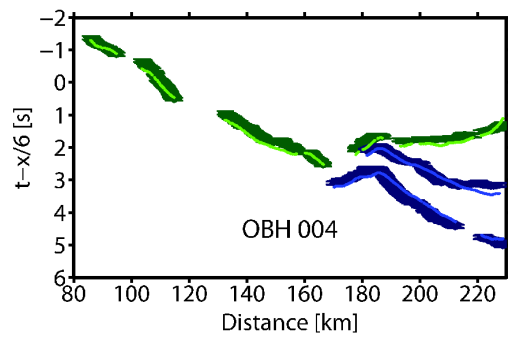
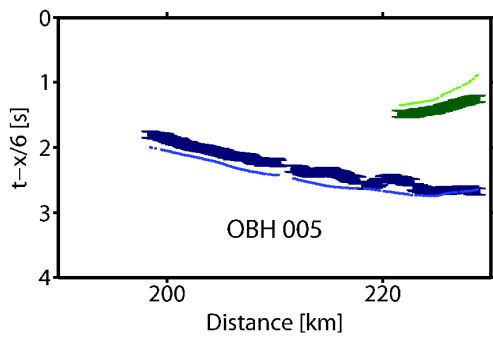


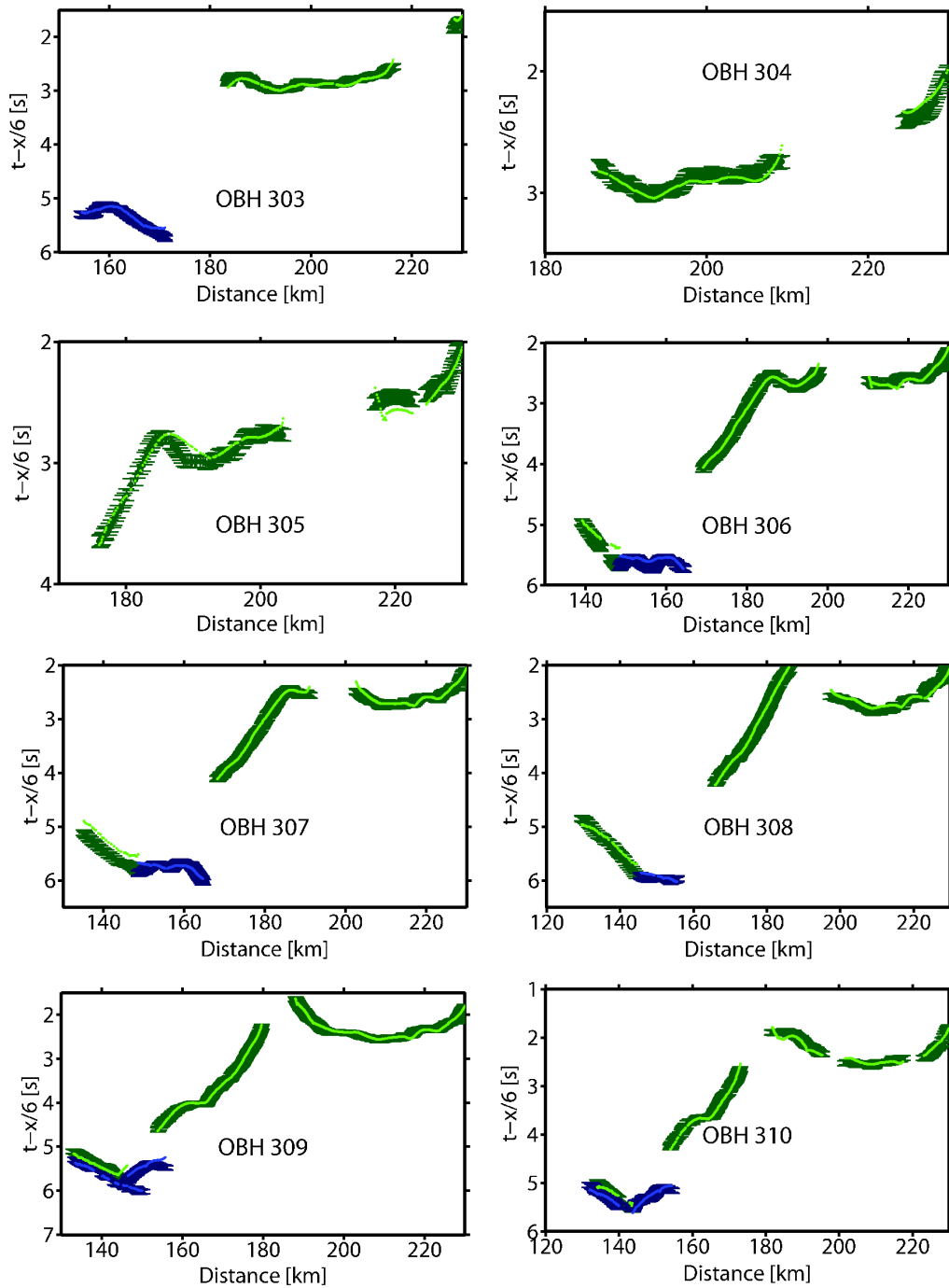




# Appendix B

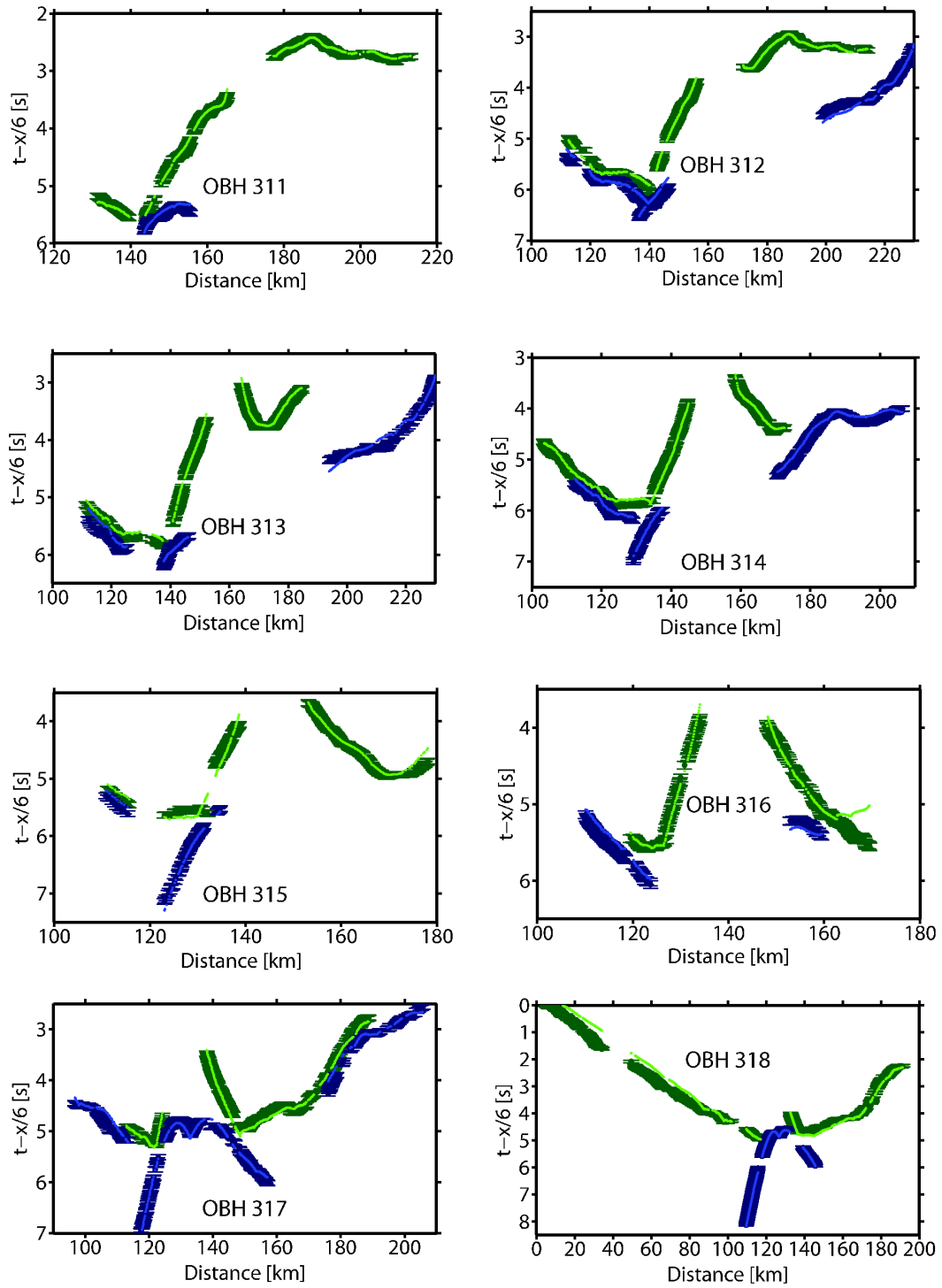
## Data picks used for $V_p$ modeling

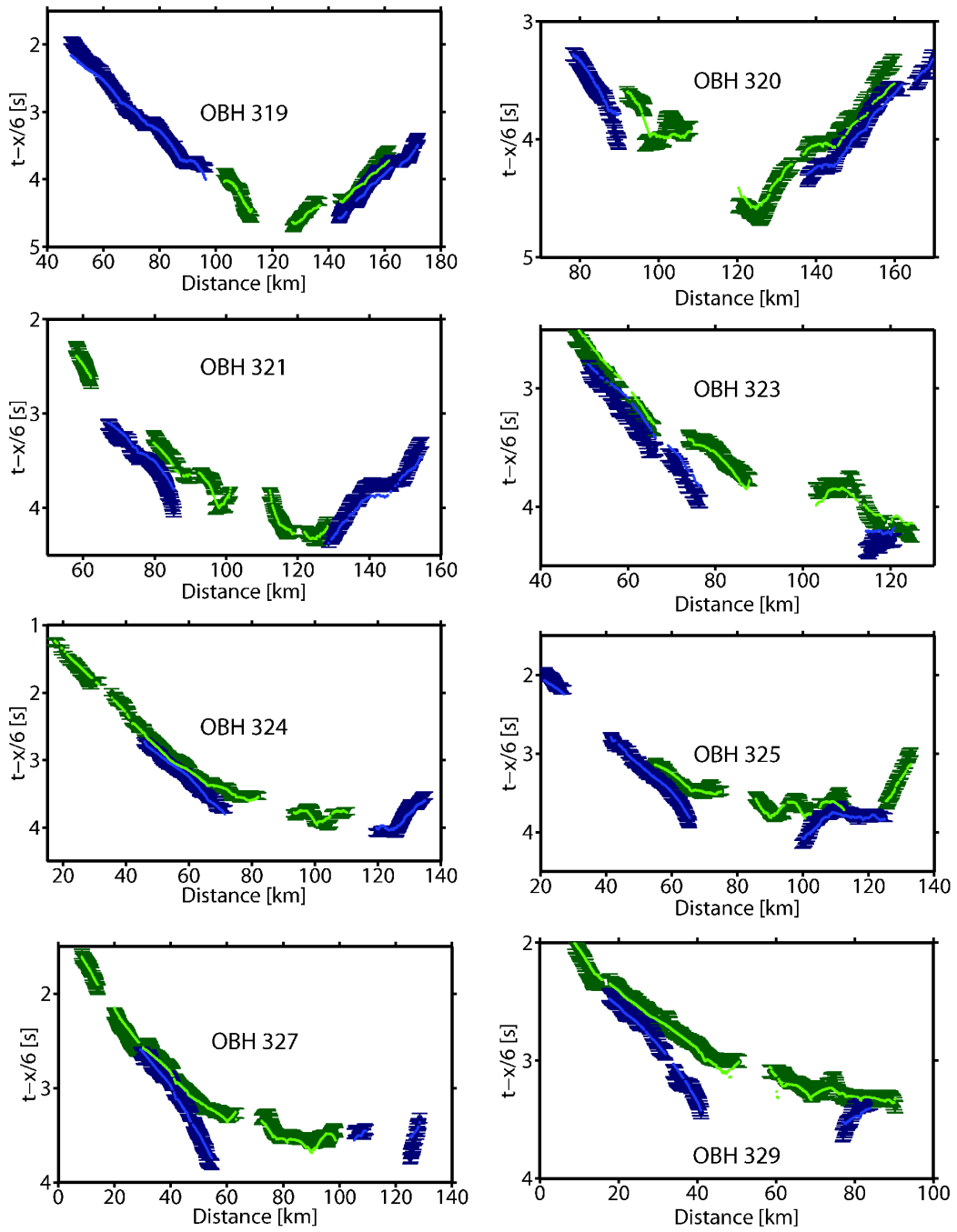






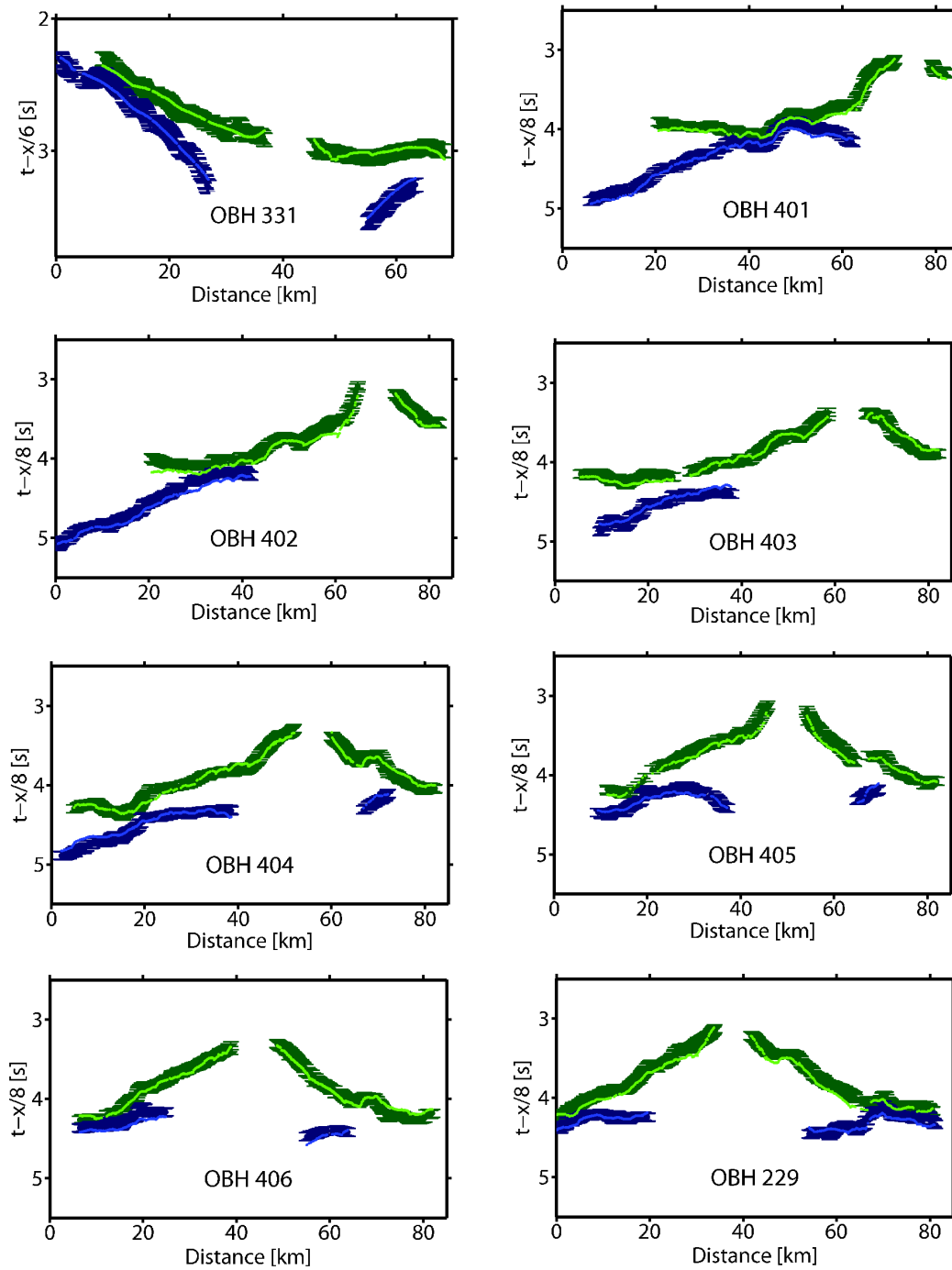
APPENDIX B. DATA PICKS USED FOR VP MODELING







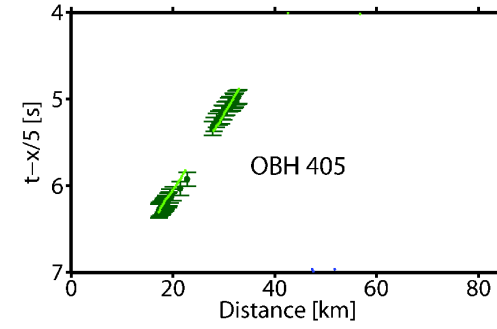
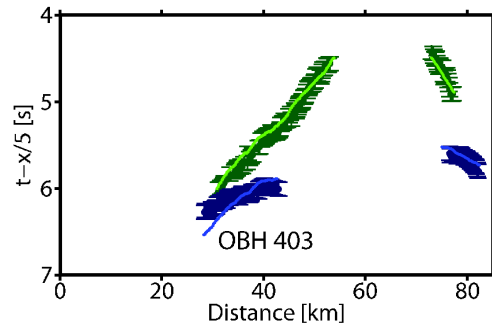
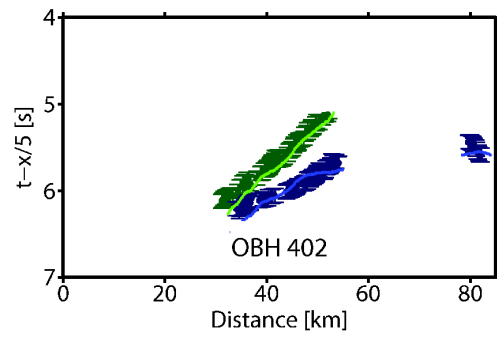
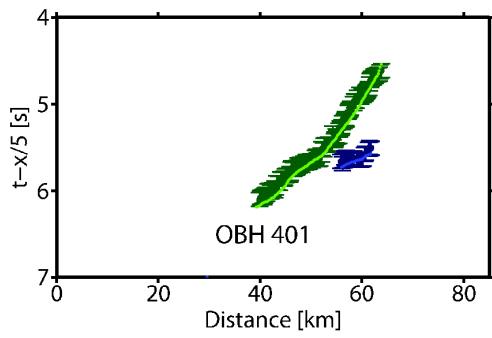
APPENDIX B. DATA PICKS USED FOR VP MODELING

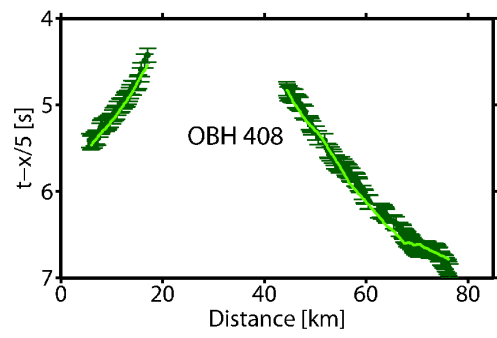
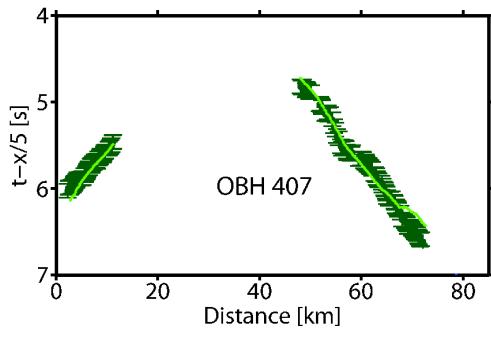
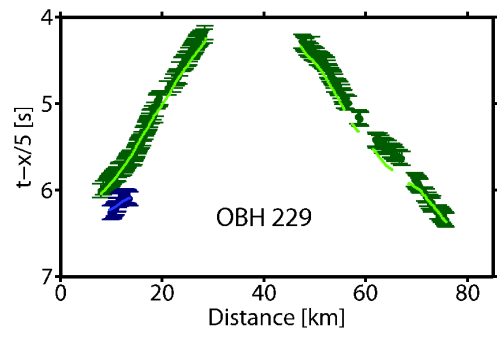
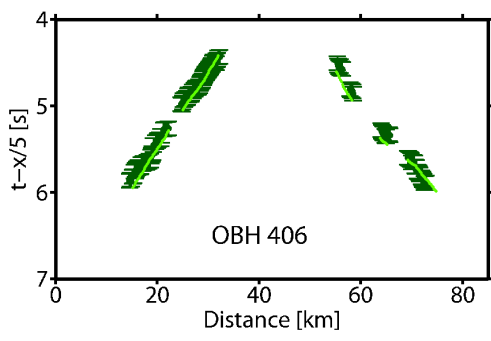


---

# Appendix C

## Data picks used for Vs modeling





# Appendix D

## Earthquake data examples and hypocenter sensitivity test

In order to test how much the hypocenters change due to variations of  $V_s$  in sediments, a sensitivity test was performed. For this test just the 7 events with gap  $< 180^\circ$  were considered. The self explanatory Figure D.1 shows the results for three different relocation procedures.

The first one consisted of relocating the events using the preferred velocity model. This model produces the minimum error. Therefore, it was used to derive the relocation of the events shown in Figure 4.10 based in the velocity models of Figure 4.8. The relocation procedure only considered the P wave arrivals. The result, presented in Figure D.1, shows that for only one event the depth is higher than considering both  $V_p$  and  $V_s$  arrivals, while the other events stay more or less in the same position. The rms error is 180 ms.

In the two following hypocenter relocation procedures, the velocity models of Table D.1 were used. They consider a sediment thickness of 1 km using two different velocities:  $V_s=0.35$  km/s and  $V_s=0.5$  km/s. From the results, one can conclude that for this dataset, a variation of the  $V_s$  in the sediment of 1,5 km/s, does not affect considerably the hypocentral locations. The simplified models used in this part of the test, produced rms errors in the order of 300-400 ms, larger than the preferred model.

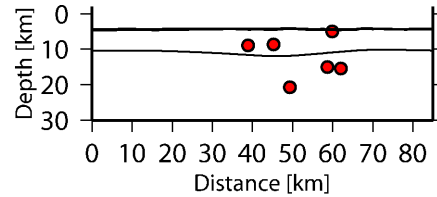
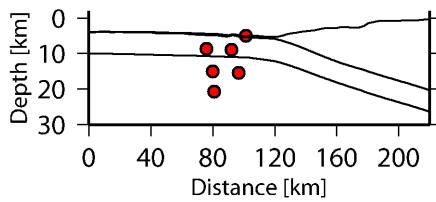
In conclusion, the epicenters do not vary significantly for the different models tested,

and the hypocenters stayed roughly in the range 5-20 km.

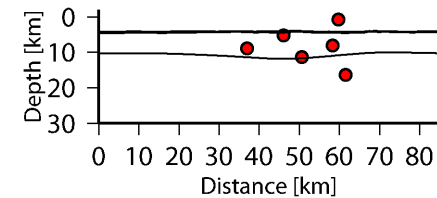
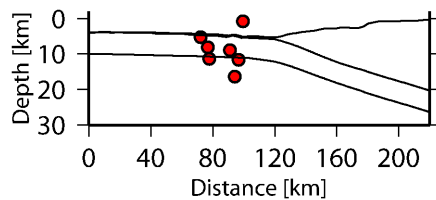
Depth from seabed (km)	Vp (km/s)	Vs model 1 (km/s)	Vs model 2 (km/s)
0	2	0.35	0.5
1	4.5	2.5	2.5
2.5	6.7	3.7	3.7
6	8.2	4.5	4.5
15	8.5	5	5

**Table D.1:** 1D velocity models used for the second part of the sensitivity test, for three different relocations.

Relocation, minimum error model,, using P wave arrivals



Relocation, considering sediments with Vs=0.35 P and S wave arrivals



Relocation, considering sediments with Vs=0.50 P and S wave arrivals

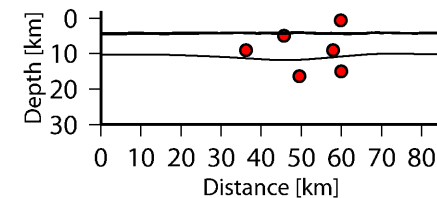
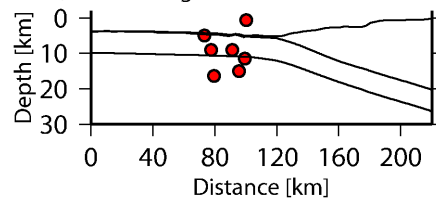


**Figure D.1:** Results of the hypocenter sensitivity test.

## APPENDIX D. EARTHQUAKE DATA EXAMPLES AND HYPOCENTER SENSITIVITY TEST

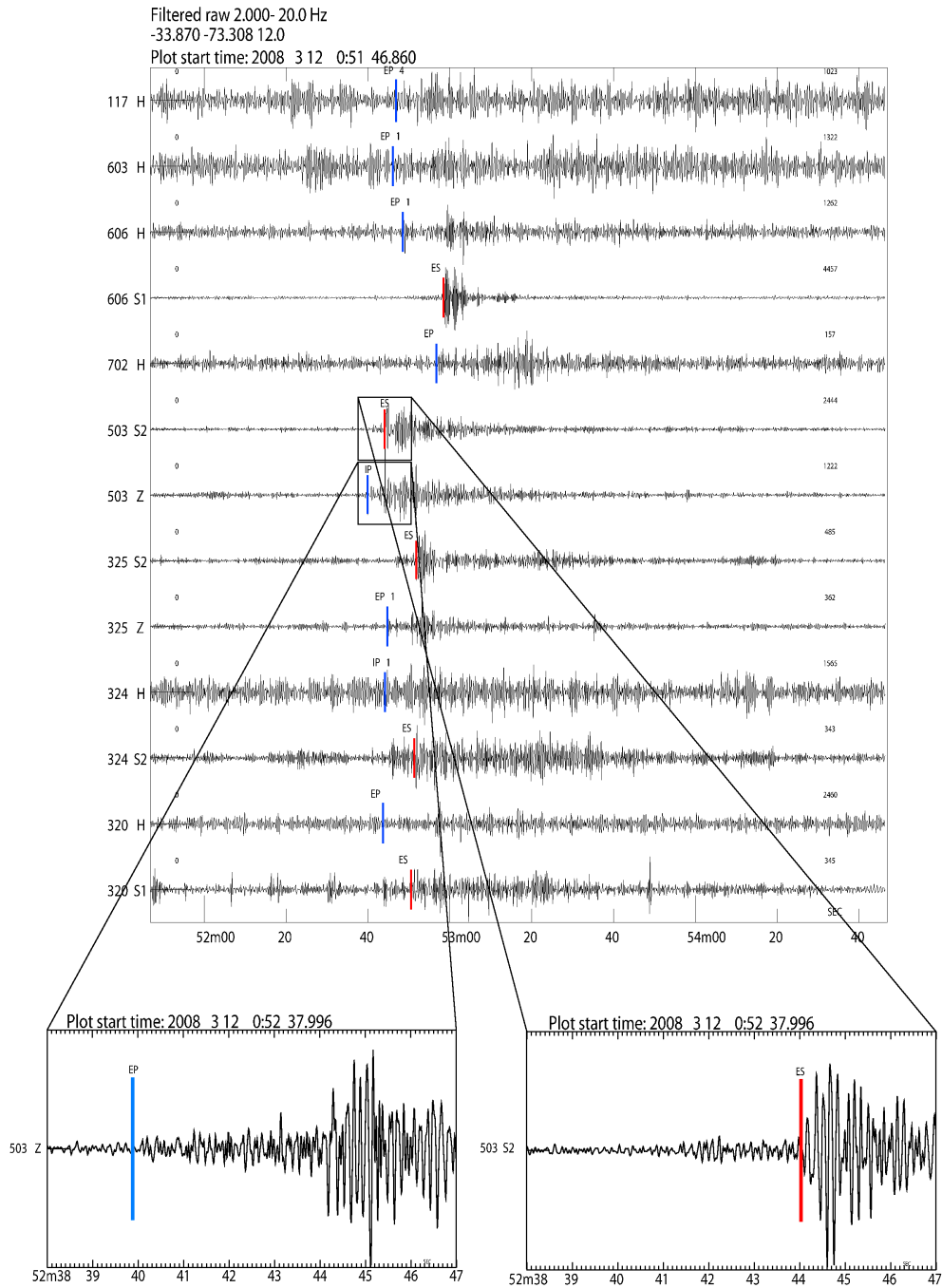


**Figure D.2:** Waveforms from two events occurred in the outer rise area and full covered by the ORN. Red bars stand for S-wave arrivals and the blue ones for P-wave arrivals. The number on the left side of each waveform stands for the obs code and the letter for the component: H: Hydrophone, S1: Horizontal component 1, S2: Horizontal component 2 and Z: Vertical component.

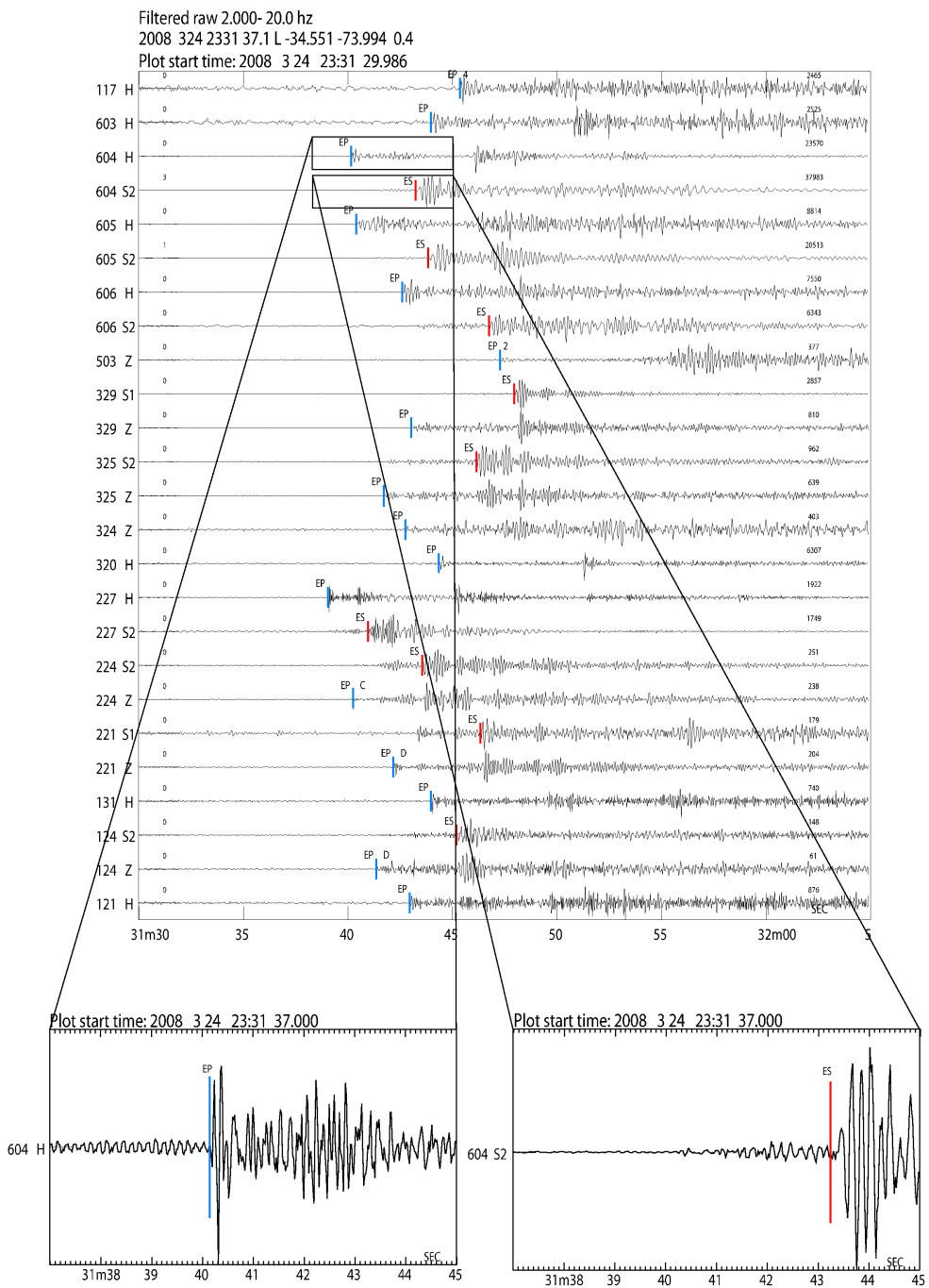


**Figure D.3:** (Figure D.2 Continuation).



# **Appendix E**

## **Moho geometry test**

### **E.1 Flat Moho v/s curved Moho**

To check the effect of a flat Moho in the travel times, we performed a forward ray tracing over a simple 2-D forward model that yields an overall error of 120 ms. This model was also used as starting velocity model for the velocity-depth ambiguity test. The final average Moho reflector and a flat reflector at 10.5 km depth (best flat geometry found by forward modelling) were used as reflectors. The results show that for distances between 25-30 km and 65 km the best fit is reached by a deeper reflector with curved geometry, while the flat reflector is not able to explain the PMP arrivals (see Figure E.1).

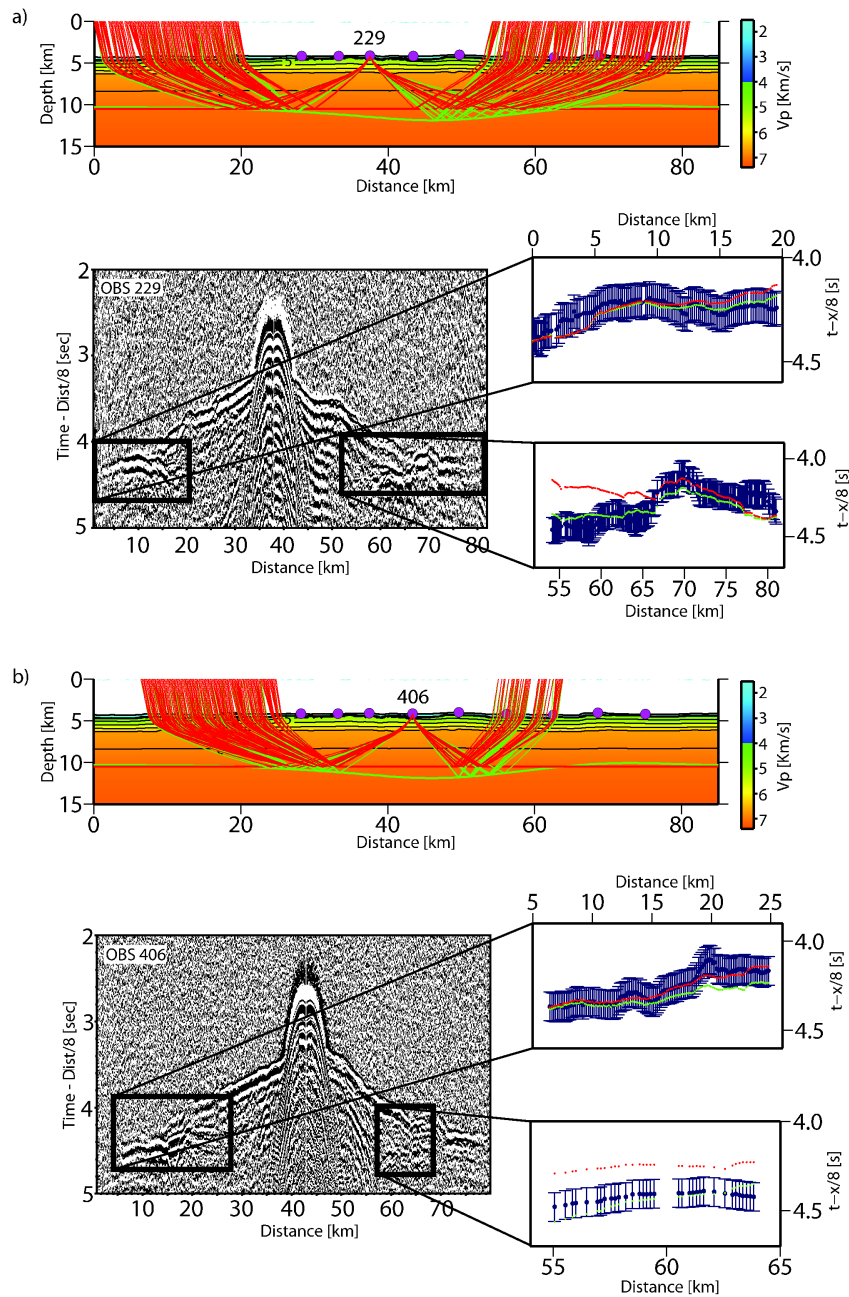


**Figure E.1:** Results of the Moho geometry test. A simple velocity model was used to test 2 different geometries: a flat Moho (red) and the curved Moho obtained from the tomographic inversion procedure (green). The ray paths for the Moho reflections, for each station and geometry are plotted over the model. Two stations were used a) OBS 229 and b) OBS 406. The result of this test shows that the arrivals observed (blue bars) are best explained by travel times calculated with the curved Moho (green dots) than with the flat one (red dots).

## E.2 Velocity-Depth ambiguity test

In order to estimate the velocity-depth ambiguity, three extra inversions for the oceanic crust were performed, following the methodology presented in section 4.4 and employing the same correlation lengths and smoothing parameters used for the final  $V_p$  model of Figure 4.8.

From the starting model and reflector of Figure E.2a, inversions were computed varying the depth kernel parameter  $\omega$ . The model of Figure E.2b was obtained using  $\omega = 10$ , that weights the depth perturbation higher than the velocity perturbation; The result of the inversion using  $\omega = 1$ , shown in Figure E.2c, equally weights depth and velocity perturbation; And finally, Figure E.2d corresponds to the results of the inversion using  $\omega = 0.01$ , that allows more velocity perturbation than depth variations. This test shows that the Moho geometry is well resolved and that the velocity field varies within the error estimated for  $V_p$  (Figure 4.5).

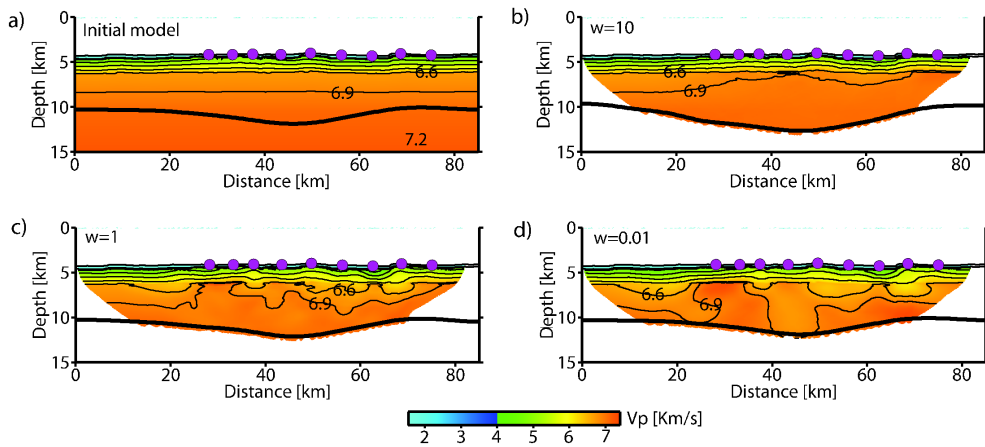


**Figure E.2:** Results of the velocity-depth ambiguity test. Successive inversions were performed using the starting model of a) and varying the depth kernel to: b)  $\omega = 10$ , c)  $\omega = 1$  and d)  $\omega = 0.01$ . The overall final error is 95 ms, 56 ms and 58 ms, respectively.

---

# Appendix F

## Dip angle test

As can be observed in Figure 1.4c, the amount of crossing ray paths in the continental crust is low, therefore the uncertainty of the lower crust velocity and the dip angle is high. We tested several dipping layers in two models with  $V_p$  of 6.7 km/s and 7.3 km/s in the lower crust, which can be interpreted as continental lower crust and upper continental mantle, respectively (see Figures F.1a and F.1b). As a result of this test, we can constrain the long offset dip angle between  $\sim 10^\circ$  and  $\sim 20^\circ$ . We have chosen the first model because the occurrence of aftershocks for offsets longer than the studied profile's maximum extension makes it unlikely that the upper continental mantle appears at depths shallower than 35-40 km.

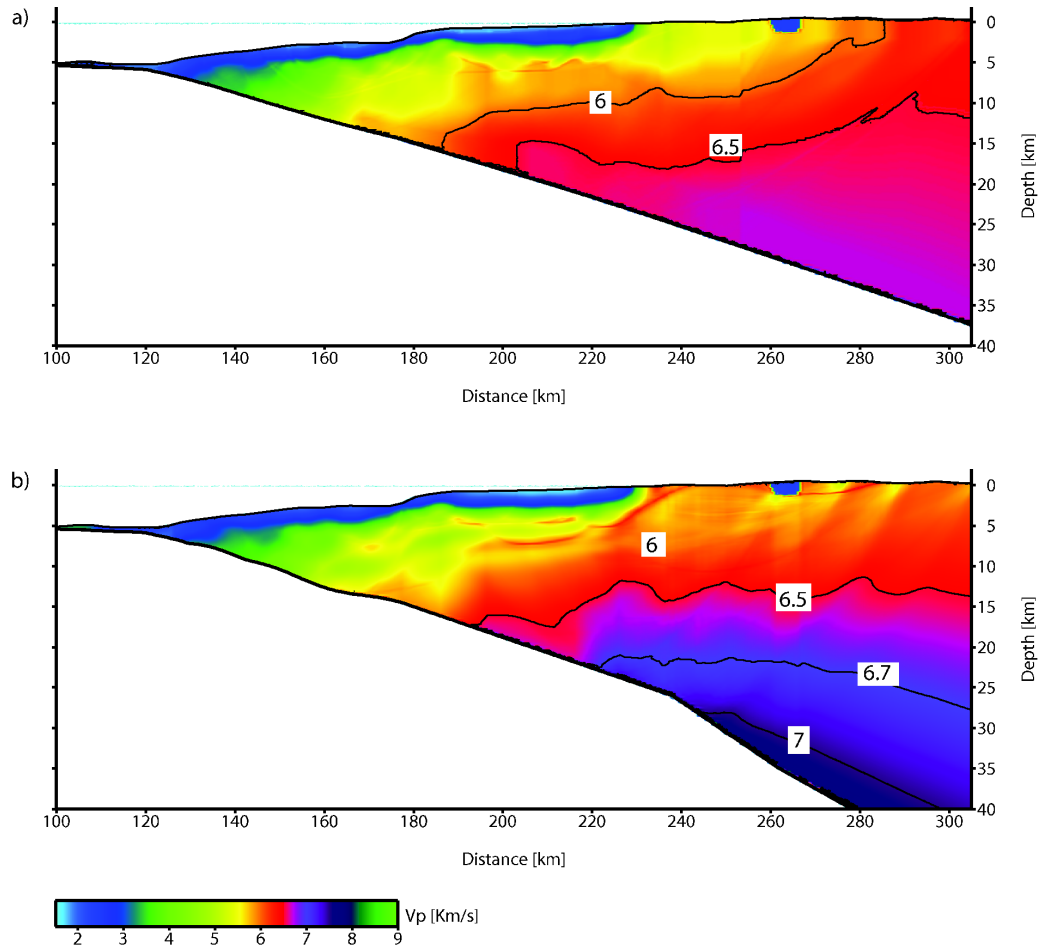


**Figure F.1:** *Since the only ray paths that illuminate the lower part of the continental crust considered during this layer's inversion are reflections, here we present two different tomographic images that fit the data picks ( $\chi^2 = 1$ ) given two different initial lower crust velocities, and how they affect the top of the oceanic crusts (TOC) geometry: a) When the velocity of the lower crust is between 6-6.7 km/s, the TOC has a dipping angle close to 10, which is the same angle modeled below the trench and accretionary prism, which is well constrained by refractions and reflections. b) When velocity of the layer at the bottom is 7.3 Km/s (which can be interpreted as the rising of the continental mantle), the reflector tends to increase the subduction angle.*

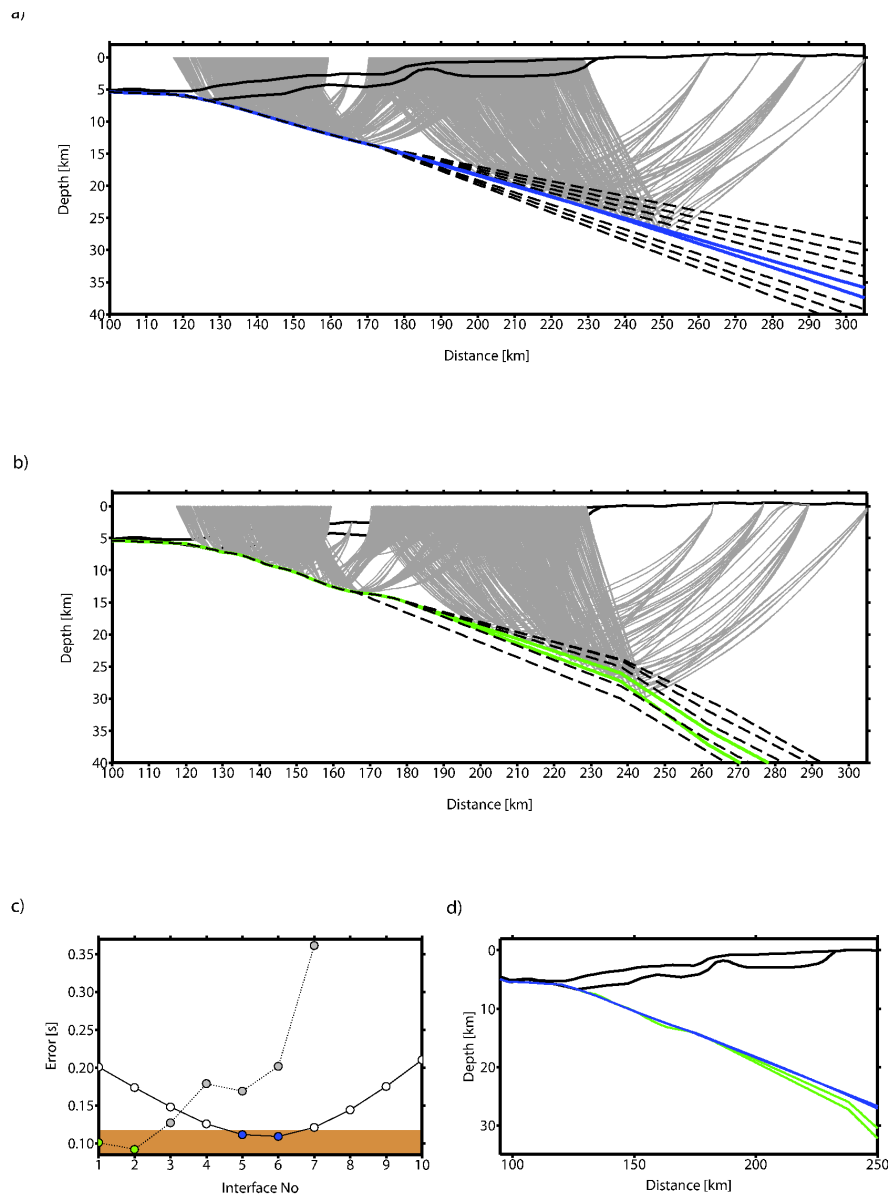


**Figure F.2:** From the models of Figure F.1, we analyzed the effect of varying the slope in the vicinity of the reflector obtained from the inversion at the zone where we have no refraction rays illuminating the lower part of the crust. In Figure a) Ten different reflector models are presented. The segmented line represents the reflectors with  $(\chi^2 = 1)$  and the solid blue lines correspond to the reflectors which adjust the data. In Figure b) the same analysis is carried out for the model with higher velocity at the bottom of the crust. Figure c) shows the RMS error of all the reflectors. The brown zone shows the pick uncertainties for PmP phases (120 ms). The TOC reflectors which satisfy the error criteria are plotted together in Figure d).

---



# Curriculum Vitae

## Personal details:

Name: Eduardo Ignacio Moscoso Henriquez  
Date of Birth: 25.08.1982  
Age: 29 years  
Place of Birth: Santiago de Chile  
Citizenship: Chilean  
Address: Hermanos Cabot 7769, Las Condes, Santiago, Chile  
email: emoscoso@ifm-geomar.de

## Education:

Since October 2008:	Phd. student at IFM-GEOMAR
Master in Geophysics:	Universidad de Chile, 2008
Civil-Electrical Engineer (equivalent to German degree Dipl. -Ing.):	Universidad de Chile, 2008
Bachelor in Engineering Sciences:	Universidad de Chile, 2007